DIFFUSION BARRIERS FOR Cu METALLISATION IN Si INTEGRATED CIRCUITS

DEPOSITION AND RELATED THIN FILM PROPERTIES

Samenstelling van de promotiecommissie

Voorzitter:	Prof. dr. ir. J. van Amerongen	Univ. Twente / EWI
Promotor:	Prof. dr. ir. R. A. M. Wolters	Univ. Twente / EWI / Philips Natuurkundig Laboratorium
Assistent-promotor:	Dr. J. Holleman	Univ. Twente / EWI
Leden:	Prof. dr. J. Schmitz	Univ. Twente / EWI
	Prof. dr. ir. A. J. Mouthaan	Univ. Twente / EWI
	Rrof. dr. C. I. M. Beenakker	TU Delft
	Prof. dr. K. Maex	KU Leuven
Deskundige:	Prof. dr. P. H. Woerlee	Philips Natuurkundig Laboratorium

This research was supported by Philips Semiconductors and carried out at Semiconductor Components (SC) group, MESA+ research institute/University of Twente, The Netherlands; Philips Research Laboratories, Eindhoven, The Netherlands.

Title: DIFFUSION BARRIERS FOR Cu METALLISATION IN Si INTEGRATED CIRCUITS
DEPOSITION AND RELATED THIN FILM PROPERTIES

Author: Svetlana Bystrova

ISBN 90-365-2114-9

Print: PrintPartners Ipskamp, Enschede, The Netherlands

DIFFUSION BARRIERS FOR Cu METALLISATION IN Si INTEGRATED CIRCUITS

DEPOSITION AND RELATED THIN FILM PROPERTIES

PROEFSCHRIFT

ter verkrijging van
de graad van doctor aan de Universiteit Twente,
op gezag van de rector magnificus,
prof.dr. F.A. van Vught,
volgens besluit van het College voor Promoties
in het openbaar te verdedigen
op woensdag 1 december 2004 om 13.15 uur

door

Svetlana Bystrova
geboren op 30 mei 1967
te Leningrad, USSR

Dit proefschrift is goedgekeurd door
de promotor Prof. dr. ir. R. A. M. Wolters en
de assistent-promotor Dr. J. Holleman

Contents

Chapter 1

Introduction

1.1 Interconnection in Si integrated circuits

Since 1960's, after the first integrated circuit was invented, the number of electronic components on a chip increases exponentially, while their size decreases. The continuous miniaturization and size reduction of components in CMOS integrated circuits (IC's) is driven by higher functionality (higher density of components/functions on chip), faster switching speed (see Table 1-1) and a lower cost per chip. For example, the number of transistors per cm^2 on a chip will increase from 61 million up to 980 million as projected for a technology with a gate length of 10 nm (see Table 1-1). In order to match the network of devices and the metallisation network the packing density of metal lines and the number of metal levels also increases (see Table 1-1).

A schematic of a structure with multilevel metallisation is shown in Figure 1-1. Metal layers, which are deposited after the transistor formation, are electrically connected by vias. This is called interconnection.

Table 1-1. Current and projected characteristics for logic application and interconnects [1].

year of production	2003	2004	2005	2010	2015
	technology node 100	90	80	45	25
transistors per chip, $x10^6$	180	226	285	1546	4908
local clock frequency, MHz	$3.0 \cdot 10^3$	$4.2 \cdot 10^3$	$5.2 \cdot 10^3$	$1.5 \cdot 10^4$	$3.3 \cdot 10^4$
transistor density, $x10^6$ transistors/cm^2	61	77	97	309	980
transistor gate length, nm	45	37	32	18	10
number of metal layers	9	10	11	12	13
pitch Metal 1, nm	240	214	190	108	60
barrier thickness, nm	12	10	9	5	3

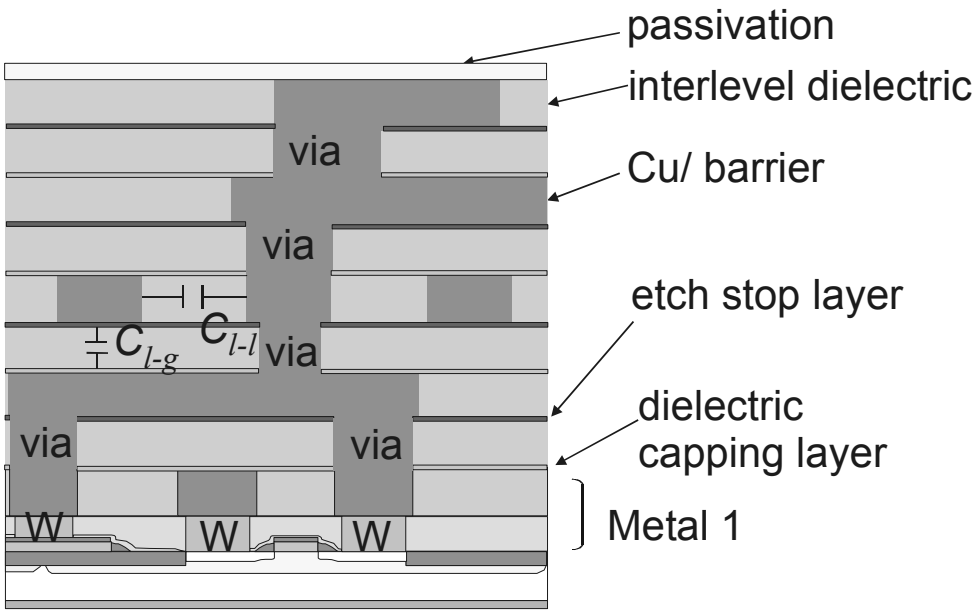

Figure 1-1. Schematic of cross section of a structure with multilevel metallisation. C_{l-l} and C_{l-g} are parasitic capacitance line-to-line and line-to-ground, respectively.

With scaling down of the gate length, the gate delay decreases (see diamonds in Figure 1-2) and the signal propagation in IC's becomes faster. At the same time the increasing density of metal lines causes a resistance increase of interconnects (R) and an increase of the parasitic capacitance (C) between metal lines. Therefore, signal delay due to interconnects, determined as R·C delay, increases (see ovals and triangles in Figure 1-2). For the technology node of 0.18 μm the interconnect delay becomes larger than the gate delay when a conventional Al/SiO_2 combination is used (see ovals and diamonds in Figure 1-2). Therefore the total signal delay (squares in Figure 1-2) determining the speed is limited by the RC delay in the interconnects.

There are two possible solutions to reduce this interconnect delay. First, by using a metal with a lower resistivity than Al. Second, by using materials with a static dielectric constant (k) lower than that of the conventional dielectric SiO_2 (~3.85): the so called low- k dielectric. Presently Cu having a resistivity of 1.7 μΩ·cm replaces Al-0.5at% Cu having a resistivity of 3 μΩ·cm [2]. The lowest interconnect delay can be obtained by using both Cu and low- k dielectric (see triangles in Figure 1-2) instead of the Al/SiO_2

combination. Cu integration in IC's, however, has some drawbacks. These are the ability of Cu to react with Si with a formation of silicides [3], to form deep energy levels in Si [4, 5] and to diffuse in dielectrics [6, 7]. This causes deterioration and failure of the electrical characteristics of devices. To prevent the Cu drift and diffusion through the dielectrics, a barrier blocking Cu is necessary between dielectric and Cu. The choice of such a barrier requires a material exploration and a study of the material reactivity with Cu and the dielectric used in back-end processing.

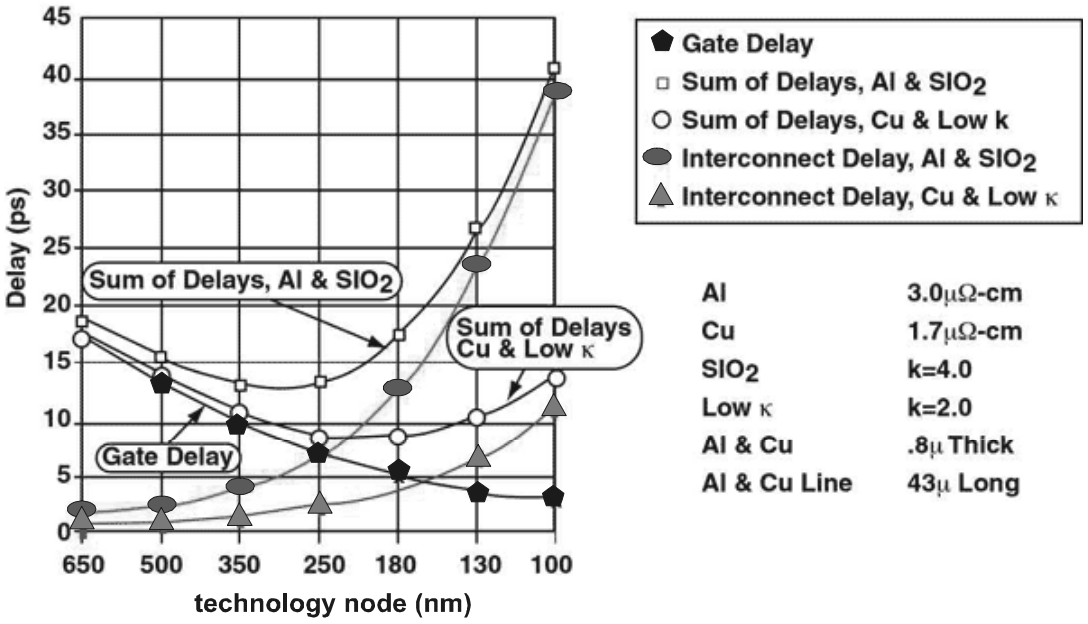

Figure 1-2. Contribution to RC delay from interconnects and gates versus generation (technology node) [1].

Among the low-k materials there are two groups of dielectrics, which are being studied nowadays: 1). inorganic materials deposited by PECVD (Plasma Enhanced Chemical Vapor Deposition), e. g. Black Diamond (BLOk^{TM}) or Aurora®. Both are dielectrics containing Si, O, C and H with k>2.5; and 2). organic materials deposited by spin-on technique, e.g. SiLK^{TM} (an aromatic hydrocarbon based polymer) with k~ 2.65 or porous SiLK with k~ 2.2. Currently, the PECVD technique, used traditionally in semiconductors industry, dominates to deposit low-k dielectrics. However, the lower dielectric constant of spin-on materials motivates research within the group of organic dielectrics. For a successful integration of organic

low-k dielectrics in back-end processing a study of their compatibility with adjacent materials in a multilevel structure, including barrier film, must be done.

1.2 Barrier choice

A barrier material must satisfy a number of requirements to be successfully applied in devices with multilevel metallisation. A list containing major requirements is presented in Table 1-2 [1, 2]. These requirements can be combined in three major groups, i.e. compositional, physical and geometrical requirements and requirements on the processing. First of all, the material must have a low reactivity with Cu and other materials used in structures with Cu, for instance, interlevel dielectrics, etch stop layers, etc. Secondly, the material must have a low resistivity to maintain the advantages of Cu. Moreover, a good adhesion of the material to Cu and interlevel dielectrics is required. A conformal deposition of the thin (<10 nm) films is required over high aspect ratio features. This means good step- and bottom coverage, i.e. the thickness at the sidewalls and at the bottom of the features should be preferably the same as on flat areas.

Table 1-2. Requirements to barriers blocking Cu diffusion.

aspects	requirements
compositional	• low reactivity with Cu and underlying material (no diffusion into surrounding, blocking Cu diffusion)
physical and geometrical	• lowest resistivity • mechanical stability (good adhesion, low stress, stress migration resistance) • good step coverage in high aspect ratio vias • thickness of films <10 nm
processing	• compatible with surrounding materials and their processing

At the same time, the deposition process for example, deposition temperature, precursors must be compatible with other processes during the fabrication of IC's.

1.2.1 Barriers overview

A numerous amount of materials has been studied for barrier application. These materials can be distinguished in: metals; binary compounds of refractory metals, such as silicides, carbides and nitrides; ternary compounds of Ta or W containing nitrogen and silicon or nitrogen and boron.

Metal films of Ta [8, 9], Ti [10] and W [9], having a polycrystalline structure, allow copper to diffuse easily along grain boundaries. Amorphous metals are quite unstable and crystallize at low temperatures, providing paths for diffusion. Therefore binary and ternary compounds with a higher thermal stability are more suitable for barrier application.

Such binary compounds of refractory metals as Ta_xN_{1-x} [8, 11], Ti_xN_{1-x} [12], Ta_xSi_{1-x} [13], Ta_xC_{1-x} [14], W_xSi_{1-x} [15], W_xN_{1-x} [16] and W_xB_{1-x} [17] have been tried as diffusion barriers. Ta_xN_{1-x}, Ti_xN_{1-x} and W_xN_{1-x} demonstrated good properties against Cu diffusion up to 500-600 ^oC as tested on p^+/n diodes. Some materials, however, are reactive with copper. Ti_xN_{1-x} integrated in back-end metallisation has shown to cause a pitting of copper [18]. This occurs due to Cl incorporated in the barrier film as a residue. Binary compounds containing Si have also been shown to be reactive with copper. Thus, these materials can not be applied for multilevel metallisation. Ternary compounds containing both silicon and nitrogen have shown to be less reactive.

Ternary compounds such as $Ta_xSi_yN_{1-x-y}$ [13, 19, 20, 21], $Ti_xSi_yN_{1-x-y}$ [21], $W_xSi_yN_{1-x-y}$ [15, 19, 20, 21], $Mo_xSi_yN_{1-x-y}$ [19], $Re_xSi_yN_{1-x-y}$ [21], $W_xB_yN_{1-x-y}$ [17], $W_xC_yN_{1-x-y}$ [18, 22, 23] have been studied. Films of these compounds can be amorphous and they exhibit a superior thermal stability. $Ta_xSi_yN_{1-x-y}$, $W_xSi_yN_{1-x-y}$, $W_xB_yN_{1-x-y}$ demonstrated good barrier properties against diffusion up to 800-900 ^oC as tested on p^+/n diodes. These properties were considerably better than for binary compounds. The amount of silicon allowed in the materials is limited due to a reactivity of silicon with copper. The ternary materials with a ratio of Si to Me not larger than 1.5 were reported to be inert with copper up to 900 ^oC [19]. An increase of nitrogen content leads to an increase of resistivity [19, 24].

Therefore a fine tuning of composition backed up with resistance measurements and compositional analysis must be done first of all.

Ternary materials on the basis of Ta and W have shown the best blocking ability of copper diffusion and they stay non- reactive with copper at higher temperatures. Properties of the material films, for instance resistivity and step (bottom) coverage, however, vary with the deposition method applied. For example, TaN by Physical Vapor Deposition (PVD) is characterized with a resistivity of 380 $\mu\Omega$·cm [11]. At the same time TaN by Chemical Vapour Deposition (CVD) has a resistivity of 920 $\mu\Omega$·cm [11]. The increase of resistivity is attributable to residuals incorporated in the films grown. Thus, the material choice should take place in combination with the deposition technique. This issue will be discussed in the next section 1.2.2.

1.2.2 Deposition methods and choice

Different techniques are applied to deposit thin films in IC fabrication. PVD is commonly used for metal based films. For the deposition of the film a target of this metal is sputtered in an appropriate ambient. Deposited films have a poor step coverage, because of the directionality of the material to be deposited. In order to improve step coverage PVD has been modified to Ionised PVD (I-PVD), Hollow cathode PVD or Low Pressure Long Throw PVD etc. I-PVD and Hollow cathode PVD aim to ionize the sputtered atoms [25]. In this case it is possible to direct ions to the features in electrical field. A sputtered film is formed by metal atoms and the ionized metal. Ions can be used to resputter the obtained film (from the edge and from the bottom of vias) improving overall coverage. A satisfactory step coverage has been reported in features of 0.25 μm with an aspect ratio of 3 for 30 nm films of Ta(N) [26]. At the bottom or on the side walls of the features, however, there are always thinner spots. Tighter geometry along with low-k integration has driven the investigation of Ti, Ta, and W based barrier materials in addition to alternative deposition techniques [27].

CVD offers more conformal deposition over small features. This method is based on a chemical reaction of precursors resulting in film growth. The step coverage for W_xN_{1-x} and $W_xSi_yN_{1-x-y}$ in 0.25 μm vias with an aspect

ratio of 4 was 70-100 %, (for 100 nm films) [24, 28]. The composition of Ta and W based ternaries, however, is difficult to control in features with high aspect ratio due to big differences in diffusion length and sticking probability between precursors [29]. Another disadvantage of this method is the possibility of gas phase reactions with the formation of particles or side reactions with the formation of undesirable adducts. For example, during the growth of W_2N using WF_6 and NH_3, these gases react with the formation of $WF_6{\cdot}NH_3$, a solid adduct [30]. In order to improve the step coverage and eliminate gas phase reactions from the CVD process the Atomic Layer Deposition (ALD) technique has been developed.

ALD can control the film thickness on an atomic scale [31]. The growth occurs via self-saturated chemisorption of various precursors pulsed over the growing film in a cycling sequence. This sequence results in a desirable outcome. The growth rate is less than one monolayer of material per cycle. As a result of the self- saturated principle of ALD, the growth occurs conformal over small features even with an extreme high aspect ratio. Step coverage of 100 % was reported for TaN films (40 nm thick) made by ALD for features of 0.1 μm with an aspect ratio as high as 11 [32].

As it has been demonstrated the choice of deposition method for a barrier is driven by the requirement of conformal growth, i.e. good step coverage. For small features with high aspect ratio CVD is superior to PVD. And ALD is the best technique. For that reason this study is focused on barriers grown by CVD and ALD.

Both Ta-based and W-based materials by CVD have been recognized equally as possible candidates for diffusion barriers (see Section 1.2.1). However, $TaCl_5$, which is the precursor for Ta, is solid at room temperature and difficult to handle in opposite to the standard liquid precursor for W, WF_6, which has a boiling temperature of 290 K [33]. Therefore we have chosen to investigate W-based films, to be specific, ternary compounds, which have a better stability of the amorphous structure. Among these are films containing silicon and nitrogen ($W_xSi_yN_{1-x-y}$), and films containing nitrogen and carbon ($W_xC_yN_{1-x-y}$).

1.2.3 Physical analytical techniques

In order to monitor the quality of barrier films grown (composition and residuals such as fluorine, oxygen, hydrogen) and a possible change of composition after thermal treatments in a copper/barrier/dielectric combination, different physical analytical techniques can be used. A brief description of principle of the commonly used techniques is given below [34].

- Auger electron spectroscopy (AES) is based on the emission of electrons (Auger electron) as a result of an electron bombardment of the material. Under the electron bombardment electrons from the core levels are ejected. The holes are filled with electrons from the higher levels, the secondary electron (Auger electron) escapes into vacuum with the remaining kinetic energy. The kinetic energy of the Auger electron is specific for the transitions of electrons in each element. By measuring this kinetic energy an elemental composition can be determined. This technique is not applicable for measuring of H and He, because at least 3 electrons in an atom are required for the generation of an Auger electron.

- X-ray photoelectron spectroscopy (XPS) is based on emission of photoelectrons from a sample under incident x-rays with energies higher than the electron binding energy. The electron binding energy depends on the chemical state of elements in a material. This makes the determination of the chemical bonds and elemental composition possible (except H and He) in compounds.

- Rutherford Backscattering Spectroscopy (RBS) is based on backscattering of incident light ions of He from the matrix of the studied material. Backscattering energy of the ions contain information on the mass/location of the elements in the material. Elastic recoil detection analysis (ERDA), as RBS, uses He^+ ions, but detects the recoil of the lighter hydrogen atoms. This effect makes determination of hydrogen possible.

In case of a reaction between materials or due to diffusion the composition of a sample changes. The depth profiling of the sample can be performed

by AES and XPS by sputtering. Using standard sensitivity factors, the concentration in depth can be calculated. However, some element combinations (e. g. W-N) suffer from the effect of preferential sputtering in a heavy matrix [35]. This makes a quantitative determination of composition with standard sensitivity factors less reliable [35, 36]. RBS, used as a non- destructive technique, determines the composition in the most accurate way with respect to AES and XPS. RBS, however, is unable to determine the chemical bonding of the measured elements. Therefore to obtain correct information about composition and compounds AES, XPS is performed in combination with RBS.

In order to identify crystalline phases present in films and their orientation, the X-ray diffraction method (XRD) is applied. The principle of XRD is based on the property that a crystal lattice diffracts monochromatic x-rays in a specific way. XRD can be applied to monitor the formation of Cu_3Si as a result of a reaction between copper and silicon.

Only metallurgical failures of the barrier or compositional changes can be detected by the described analytical techniques. The operation of devices, however, can be affected at a much lower level of Cu contamination of $\sim 10^{13}$ cm^{-3} [37]. Thus a barrier failure, resulting in copper diffusion through the barrier should be detected with electrical measurements.

1.2.4 Testing of barrier

Electrical characterisation

Different electrical measurements have been reported in literature to test the barrier integrity. First of all, reactivity between barrier and copper should be tested. This can be done with *four-point probe sheet resistance measurements* of Cu/barrier/SiO_2 stacks on Si substrates [8].

The test of the diffusion properties of barriers is performed on devices including diodes and capacitors.

I-V characteristics of p^+/n diodes are used to test a barrier failure. Cu diffusion is associated with an increase of leakage current [8, 11-13, 15-17, 19-20].

Capacitance- Voltage (C-V) measurement of Cu/barrier- gate capacitors before and after annealing is a mature method to monitor charges in oxide. Copper ions diffused or drifted in the oxide cause a shift of flatband voltage towards negative voltage [6, 38]. This shift is a measure of the amount of Cu ions in the oxide (mainly at SiO_2/Si interface). In a capacitor with 100 nm thick oxide, low charge densities of $\sim 1 \cdot 10^9$ cm^{-2} at the SiO_2/Si interface will result in a shift of 0.005 V, which is difficult to measure. The thicker the oxide, the bigger shift is expected for the same charge density.

The *Triangular Voltage Sweep (TVS) measurements* applied to the capacitors use the ability of copper ions to drift in oxide under an applied electrical field at elevated temperature [39-41]. The obtained current-voltage dependence shows a peak of current corresponding to mobile ions in oxide. The amount of ions in oxide determined from TVS measurements can be as low as 10^9 cm^{-2} [34].

Adhesion

One of the requirements of a material introduced into a multilevel metallisation process is good adhesion. The traditional "scratch and pull" scotch tape test is applied to test adhesion qualitatively. In order to quantify the adhesion energy of an interface the four point bend techniques can be used [42]. In the applications and in the measurements it is assumed that adhesion failure is determined as a result of plastic deformation. For example, a limit of adhesion energy for inorganic materials, at which no delamination occurs during Chemical Mechanical Polishing (CMP), was found to be 5 J/m^2 [43]. Knowing the critical limit of adhesion energy alone is not enough to predict along which interface the fracture takes place during CMP [44]. Nevertheless, a quantification of adhesion is a prerequisite to rank barrier films with respect to adhesion.

1.3 Motivation

Although Cu metallisation has been used for years, the continuous scaling with the decrease of the barrier thickness predicted by ITRS and integration issues demand an introduction of new materials satisfying requirements to a diffusion barrier (see Table 1-1). The choice of the deposition technique for barrier deposition is driven by the requirement of

good step- and bottom coverage. PVD processes for the barrier application are being replaced by CVD and ALD. This study is focused on the growth processes of tungsten nitride silicide films by CVD; tungsten nitride and tungsten carbide nitride films by ALD. In order to estimate the suitability of these materials as a diffusion barrier, the reactivity, diffusion properties and adhesion should be tested.

Moreover, integration of low-k dielectrics in a back-end process of IC's requires a study of processes at the interface of these films with other surrounding materials. Ta-based materials by PVD are used conventionally as barriers. Therefore a study of the interaction of low-k dielectrics with Ta-based materials should be performed.

1.4 Outline of the thesis

The thesis consists of seven chapters.

The motivation for this research has been discussed in *Chapter 1*.

Chapter 2 presents an overview of the methods used for electrical measurements, which were used to test blocking properties of the studied materials. A layout of the test devices as well as the process flow is presented.

Chapter 3 discusses the results of thermodynamical simulations performed for CVD of tungsten compounds in a system of WF_6, NF_3, SiH_4 and Ar. The results of simulations served as an input for the process study, determining ratio of gas flows for the CVD (*Chapter 5*). For the ALD process with a cycling sequence of precursors such as WF_6, NH_3, C_2H_4 and SiH_4 (*Chapter 6*) the thermodynamic calculations with available data are not suitable for (qualitative) analysis of the process.

The results of a study on integration issues of SiLK (pSiLK) such as reactivity with Ta-based diffusion barriers and adhesion are presented in *Chapter 4*.

Chapter 5 presents the results of the study of the CVD process of $W_xSi_yN_{1-x-y}$ deposition, the study of reactivity of this material with copper and its diffusion properties. A tuning of the composition of the films is

very difficult regarding N-content. A qualitative model of this phenomenon is discussed.

Results of the growth study of $W_{1.5}N$ and $W_{1.5}CN$ films are discussed in *Chapter 6*. Both $W_{1.5}N$ and $W_{1.5}NC$ are tested in p^+/n diodes and capacitors. The measurement results have demonstrated no reactivity with copper and excellent blocking properties against copper diffusion at temperatures used in back-end processing (~400 ^oC).

Finally, the summary, conclusions and recommendations are presented in *Chapter 7*.

References

1. International Technology Roadmap for Semiconductors (ITRS) 2003.
2. S. P. Murarka, Multilevel interconnects for ULSI and GSI era, *Material Science and Engineering*, R19, N^o 3- 4, p.87-151 (1997).
3. A. A. Istratov, H. Hedemann, M. Seibt, O. F. Vyvenko, W. Schröter, T. Heiser, C. Flink, H. Hieslmair, and E. R. Weber, Electrical and Recombination Properties of Copper-Silicide Precipitates in Silicon, *J. Electrochem. Soc*., Vol. 145, №11, p. 3889-3898 (1998).
4. H. Lemke, Defect Reactions in Copper-doped Silicon Crystals, *Phys. Status Solidi* (A), 95, p. 665-677 (1986).
5. A. A. Istratov, E. R. Weber, Electrical properties and recombination activity of copper, nickel and cobalt in silicon, *Appl. Phys. A* 66, p. 123-136 (1998).
6. J. D. McBrayer, R. M. Swanson, T. W. Sigman, Diffusion of metals in siicon dioxide, *J. Electrochem. Soc*, *Solid-State science and technology*, Vol. 133, N 6, p. 1242-1246 (1986).
7. G. Raghavan, C. Chiang, P. B. Anders, S.-Mo Tzeng, R. Villasol, G. Bai, M. Bohr, D. B. Fraser, Diffusion of copper through dielectric films under bias temperature stress, *Thin Solid Films*, 262, p. 168-176 (1995).
8. M. T. Wang, Y. C. Lin, and M. C. Chen, Barrier Properties of Very Thin Ta and TaN Layers Against Copper Diffusion, *J. Electrochem. Soc.*, Vol. 145, No 7, 2538-2545 (1998).
9. G. Bai, S. Wittenbrock, V. Ochoa, R. Villasol, C. Ciang, T. Marieb, D. Gardner, C. Mu, D. Fraser, and M. Bohr, Effectiveness and reliability of metal diffusion barriers for copper interconnects, *Mat. Res. Soc. Symp. Proc.*, Vol. 403, p. 501-506 (1996).
10. F. Braud, J. Torres, J. Palleau, J. L. Mermet, M. J. Mouche, Ti- diffusion barrier in Cu- based metallization, *Appl. Surf. Sci.* 91, p. 251-256, (1995).

11. M. H. Tsai and S. C. Sun, C. E. Tsai, S. H. Chuang, and H. T. Chiu, Comparison of the diffusion barrier properties of chemical- vapor-deposited TaN and sputtered TaN between Cu and Si, *J. Appl. Phys*. 79(9), p. 6932-6938 (1996).
12. S.C. Sun, M. H. Tsai, H. T. Chiu, S. H. Chuang, and C. E. Tsai, A Comparative Study of CVD TiN and CVD TaN Diffusion Barriers for Copper Interconnection, *IEEE (1995)* IEDM 95-461-463.
13. E. Kolawa, J. S. Chen, J. S. Reid, P. J. Pokela, and M.- A.Nicolet, Tantalum-based diffusion barrirs in Si/Cu VLSI metallizations, *J. Appl. Phys.* 70(3), p. 1369-1373 (1991).
14. J. Imahori, T. Oku, M. Murakami, Diffusion barrier properties of TaC between Si and Cu, *Thin Solid Films*, 301, p. 142-148 (1997).
15. M. T. Wang, Y. C. Lin, J. Y. Lee, C. C. Wang, and M. C. Chen, Effective Improvement on Barrier Capability of Chemical Vapor Deposited WSi_x Using N_2 Plasma Treatment, *J. Electrochem. Soc.* 146 (4), p.1583-1592 (1999).
16. S. C. Sun, M. N. Tsai, H. T. Chiu, and S.H. Chuang, A New CVD Tungsten Nitride Diffusion Barrier for Cu Interconnection, *Symposium on VLSI Technology Digest of Technical Papers*, p. 46-47 (1996).
17. J. S. Reid, R. Y. Liu, P. M. Smith, R. P. Ruiz, M. A. Nicolet, W-B-N diffusion barriers fo Si/Cu metallizations, *Thin Solid Films*, 262, p. 218-223 (1992).
18. W. Besling, A. S. Satta, J. Schuhmacher, T. Abell, V. Sutcliffe, A- M. Hoyas, G. Beyer, D.Gravesteijn, K. Maex, *Interconnect Technology Conference, 2002. Proc. of the IEEE 2002 International*, p. 288–291 (2002).
19. J. S. Reid, E. Kolawa, R. P. Ruiz and M.- A. Nicolet, Evaluation of amorphous (Mo, Ta, W)-Si-N diffusion barriers for <Si>/Cu metallizations, *Thin Solid Films*, 236, p. 319-324 (1993).
20. Marc- A. Nicolet, Tenary amorphous metallic thin film as diffusion barriers for Cu metallisation, *Appl. Surf. Science*, 91, p. 269-276 (1995).
21. R. Somatri-Bouamrane, N. Chevarier, A. Chevarier, A. M. Dutron, E. Blanquet and R. Madar, Ion beam analysis of ternary silicides Me-Si-N (Me= Re, Ta, Ti, W) thin films used as diffusion barriers in advanced metallization, *Electrochem. Soc. Proc.* Vol. 97-25, p. 741-748 (1997).
22. S. Smith, W.- M. Li, K.-E. Elers, K. Pfeifer, Physical and electrical characterization of ALCVD^{TM} TiN and WN_xC_y used as a copper diffusion barrier in dual damascene backend structures, *Microelectronic Engineering*, 64, p. 247-253 (2002).

23. W.-M. Li, K. Elers, J. Kostamo, S. Kaipio, H. Huotari, M. Soininen, P. J. Soininen, M. Tuominen, S. Haukka, S. Smith, W. Besling, *IEEE 2002,* International Interconnects and Technology Conference 2002.
24. J. G. Fleming, E. Roherty- Osmun, Paul Martin Smith, Jonathan S. Custer, Y.- D. Kim, T. Kacsich, M.- A. Nikolet, C. J. Galewski, Growth and properties of diffusion barriers deposited by chemical vapor deposition, *Thin Solid Films*, 320, p.10-14 (1998).
25. S.M. Rossnagel, Directional and preferential sputtering-based physical vapor deposition, *Thin Solid Films*, 263, p.1-12 (1995).
26. Zs. Tökei, D. McInerney, M. Baklanov, G.P. Beyer and K. Maex, Step coverage and continuity of an I-PVD Ta(N) barrier layer: limitations, *Proc. of the IEEE 2001 International Interconnect Technology Conference (Cat. No.01EX461)*, p. 213-215 (2001).
27. K.C. Yu, et al., Integration Challenges of 0.1μm CMOS Cu/Low-k Interconnects, Proc. International Interconnect Technology Conference, June 3-5, 2002 Session 2.1.
28. P. M. Smith, J. S. Custer, J. G. Fleming, El. Roherty- Osmun, M. Cohn, and R.V. Jones, *Proc. Thirteenth International VLSI Multilevel Interconnection Conference (VMIC)*, p. 162-167 (1996).
29. D. Srinivas, G. B. Raupp, T. S. Cale, M. K. Jain, B. Rogers, Step coverage of tungsten silicide films deposited by low pressure dichlorosilane reduction of tungsten hexafluoride, *Thin Solid Films*, v 193-194, n 1-2, p. 234-243 (1990).
30. T. Nakajiama,K. Watanabe and N. Watanabe, Preparation of Tungsten Nitride Film by CVD Method Using WF_6, *J. Electrochem. Soc.*, 134(12), p. 3175-3178 (1987).
31. T. Suntola, Atomic layer epitaxy, *Mat. Sci. Rep*., 4 (7), p. 261-312 (1989).
32. O. van der Straten, Y. Zhu, K. Dunn, E. Eisenbraun, A. Kaloyeros, Atomic layer deposition of tantalum nitride for ultrathin liner applications in advanced copper metallization schemes, *Journal of Mat. Research*, v 19, n 2, p. 447-453 (2004).
33. CRC handbook of chemistry and physics, vol. 82, 2001/2002, ISSN 0147-6262.
34. D. K. Schröder, Semiconductor materials and device characterization, NY, John Wiley& Sons, 1998, ISBN 0471-24139-3.
35. J. L. Alay, H. Bender, G. Brijs, A. Demesmaeker and W. Vandervorst, Qualitative Analysis of W(N), TiW and TiW(N) Matrices using XPS, AES, RBS, EPMA and XRD, *Surface and Interface Analysis*, Vol. 17, p. 373-382 (1991).
36. O.H. Gorkce, S. Amin, N. M. Ravinda, D. J. Szostak, R. J. Paff, J. G. Fleming, C. J. Galewski, J. Shallenberger, R. Eby, Effects of annealing on

X-ray-amorphous CVD W-Si-N barrier layer materials, *Thin Solid Films*, 353, p. 149-156 (1999).

37. A. A. Istratov, C. Flink, E.R. Weber, Impact of the unique physical properties of copper in silicon on characterization of copper diffusion barriers, *Phys. Stat. Sol*. (b) 222, p. 261-277 (2000).
38. V. S. C. Len, R.E. Hurley, N. McCusker, D. W. McNeill, B. M. Armstrong, H. S. Gamble, An investigation into the performance of diffusion barrier materials against copper diffusion using metal-oxide-semiconductor (MOS) capacitor structures, *Solid State Electronics*, 43, p. 1045-1049 (1999).
39. S. A. Cohen, J. Liu, L. Gignac, T. Ivers, D. Armbrust, K. P. Rodbell and S. M. Gates, Characterization of thin dielectric films as copper diffusion barriers using triangular voltage sweep, *Mat. Res. Soc. Symp. Proc*., Vol. 565, p. 189-196 (1999).
40. G. W. Book, K. Pfeifer, S. Smith, Barrier integrity testing of Ta using triangular voltage sweep and a novel CV-BTS test structure, *Microelectronic Engineering*, 64, p. 255-260 (2002).
41. J. Cluzel, F. Mondon, D. Blachier, Y. Morand, L. Martel and G. Reimbold, Electrical Characterization of Copper Penetration Effects, *Annual Proceedings - Reliability Physics (Symposium)*, p 431-432 (2002).
42. P. G. Charalambides, J. Lund, A. G. Evans, R. M. McMeeking, A Test Specimen for Determining the Fracture Resistance of Bimaterial Interfaces, J. of Appl. Mechanics, Vol. 56, p.77-82 (1989).
43. T. Scherban, B. Sun, J. Blaine, C. Block, B. Jin and E. Andideh, Interfacial Adhesion of Copper-Low k Interconnects, *Proc. of the IEEE 2001 International Interconnect Technology Conference (Cat. No.01EX461)*, p. 257-259 (2001).
44. F. Iacopi, D. Degryse, I. Vos, M. Patz, K. Maex, *Mat. Res. Soc. Symp. Proc.*, v 795, Understanding adhesion failure in low-k dielectric stack during chemical-mechanical polishing, *Thin Film- Stresses and Mechanical Properties X*, p. 131-136 (2003).

Chapter 2

Electrical characterisation methods and test structures

2.1 Introduction

Electrical characterisation techniques are used to test the suitability of a material as a diffusion barrier. First of all, reactivity of a barrier should be tested. This is done by four-point probe sheet resistance measurements before and after annealing [1] or in situ during heat treatment. Secondly, testing of the diffusion properties of the barrier should be performed. Traditional techniques, used to monitor effects of Cu contaminations and, therefore, diffusion properties of the barrier, are: I-V characteristics of reverse biased p/n diodes [2-4]; C-V and TVS measurements of capacitors [5, 6]; I-V characteristics of Schottky diodes [7]. The last method, being highly sensitive to changes at the interface with Si, requires a separate study of the preparation of a Si surface and the subsequent barrier deposition. Our goal is to characterise the diffusion properties of a material, not to develop a Schottky barrier diode on Si. Therefore, measurements of Schottky diodes will not be discussed.

The increase of the leakage current in diodes is attributed to Cu trapping centers, which are very effective recombination centers reducing drastically minority lifetime at the concentration of Cu higher than the doping level in p-Si and higher than 10^{13} cm^{-3} in n-Si [8].

In dielectrics, e.g. SiO_2, copper ions drift very fast under an applied electrical field at elevated temperature. Therefore C-V measurements after heat treatment and after BTS (Bias Temperature Stress), and TVS (Triangular Voltage Sweep) technique are applied in order to evaluate diffusion properties of the barrier.

2.2 Methods

2.2.1 Resistance measurements

Collinear four-point probes

The four-point probe technique is used to measure the sheet resistance of metals and semiconductors on wafers with blanket films. A current (I) is forced via two outer probes through a conducting layer giving a potential drop (V), which is measured between the inner two probes. The probe arrangement is shown in Figure 2-1. The distance s is constant and the sheet resistance (R_s) is given by:

$$R_s = \frac{2 \cdot \pi \cdot s}{t} \cdot F \cdot \frac{V}{I} \qquad \textit{Equation 2-1}$$

Where F is a correction factor, which depends on the sample geometry. If the film thickness is less than the probe space, F is given by:

$$F = \frac{t}{s \cdot 2 \cdot \ln(2)} \qquad \textit{Equation 2-2}$$

Thus, (eq.2-1) becomes

$$R_s = \frac{\pi}{\ln(2)} \cdot \frac{V}{I} = 4.532 \cdot \frac{V}{I} \qquad \textit{Equation 2-3}$$

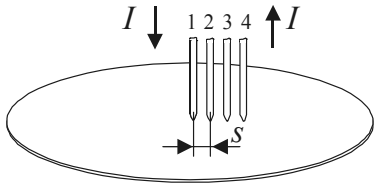

Figure 2-1. A collinear four-probes arrangement for the resistance measurements.

Other arrangements of the probes are possible, but different corrections factors have to be used.

Van der Pauw

Van der Pauw applied the four-point probe method to measure samples with an arbitrary or symmetrical shape. For a square arrangement as shown in Figure 2-2 the equation for the sheet resistance is equal to eq. 2-3,

where V is the potential drop between probe 3 and 4, and the current is flowing between probe 1 and 2.

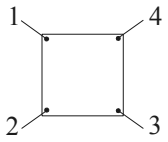

Figure 2-2. Symmetrical sample with 4 contacts.

2.2.2 Diode Current-Voltage measurements

Current-voltage I-V measurements of diodes allow us to obtain information about recombination current under forward voltage and leakage current under reverse bias. These data are used to calculate recombination and generation minority carrier lifetime, respectively. In this study I-V measurements have been done with an HP 4156B parameter analyser.

The total current through the p-n junction is a combination of the diffusion component in the neutral region (due to a concentration field) and a drift current in the p-n junction (due to electrical field).

Zero bias

At zero bias the drift current compensates the diffusion component and the potential drop across junction is called the built-in voltage V_{bi}, which is dependent on doping levels of p- and n-Si, N_A and N_D, with a relation:

$$V_{bi} = \frac{kT}{q} \cdot \ln \frac{N_A \cdot N_D}{n_i^2} \qquad \textit{Equation 2-4}$$

where k is Boltzmann's constant (1.38×10^{-23} J/K); q is a magnitude of electronic charge (1.6×10^{-19} C).

Forward bias

Under forward bias V_a the potential drop across the p-n junction is reduced and becomes equal to (V_{bi}-V_a). Holes from the neutral p-region and electrons from the neutral n-region will be injected across a space-charge

region. Some of them will recombine with majority carriers in the space-charge region, some in the neutral regions, electrons and holes, respectively, which are supplied from ohmic contacts. Thus, the components of forward current are 1) the recombination or drift current I_R in the space charge region and 2) a recombination current in the quasi-neutral region, which is often called diffusion current, I_{dif}:

$$I = I_{dif} + I_R \qquad \textit{Equation 2-5}$$

A typical Current-Voltage (*I-V*) plot is shown in Figure 2-3. Recombination current in the depletion region dominates at low voltages. Current components depend on applied bias exponentially, however with different arguments. E. g. the recombination current in the depletion region I_R is proportional to $exp[V_a/2]$:

$$I_R(V_a) = I_R(0) \cdot \left[\exp\left(\frac{qV_a}{2k \cdot T} \right) - 1 \right] \qquad \textit{Equation 2-6}$$

where $I_R(0)$ is a recombination current at zero bias. The value of $I_R(0)$ can be obtained as the intersect of the (*I-V*) slope for the depletion region with the y-axis. When the voltage increases, the diffusion current in the neutral region becomes dominant.

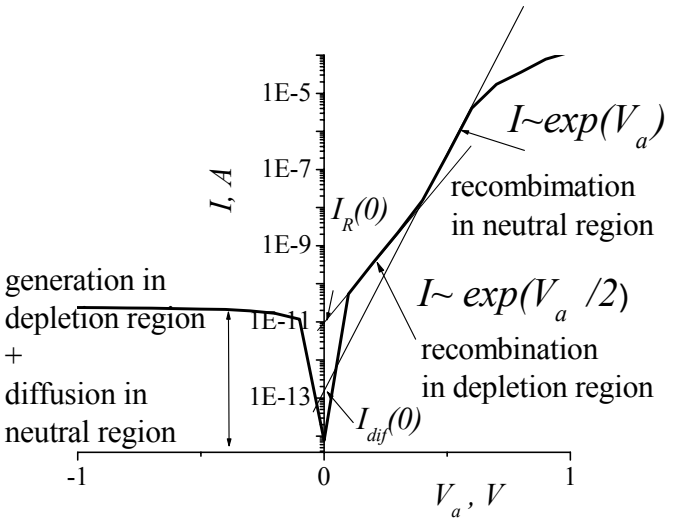

Figure 2-3. Typical I-V plot for a diode.

The slope of the current in the neutral region is related to the applied voltage as $exp[V_a]$ multiplied with a diffusion current at zero bias $I_{dif}(0)$:

$$I_{dif}(V_a) = I_{dif}(0) \cdot \left[\exp\left(\frac{qV_a}{k \cdot T} \right) - 1 \right] \qquad \textit{Equation 2-7}$$

$I_{dif}(0)$ is obtained by extrapolation of the current slope in the neutral region to zero voltage.

On the other hand, $I_R(0)$ is expressed with a width of the depletion layer W_d divided by a recombination lifetime of minorities τ_r:

$$I_R(0) = \frac{A \cdot q \cdot n_i \cdot W_d}{2 \cdot \tau_r} \qquad \textit{Equation 2-8}$$

The width of the depletion layer W_d is dependent on the doping levels in the diode. If $N_A >> N_D$, it is approximated with the following equation:

$$W_d = \sqrt{\frac{2\varepsilon_{Si}}{qN_D} \cdot (V_{bi} - V_a)} \qquad \textit{Equation 2-9}$$

Thus, using eqs. 2-8, 2-9 and the value of $I_R(0)$, we can calculate the recombination lifetime.

A value of the diffusion current at 0 bias, $I_{dif}(0)$, gives us the estimate of the recombination in the neutral region at the distance of the diffusion lengths of minorities L_p and L_n with a relation:

$$I_{dif}(0) = A \cdot \left[\left(\frac{q \cdot D_p}{N_D \cdot L_p} + \frac{q \cdot D_n}{N_A \cdot L_n} \right) \cdot n_i^2 \right] \qquad \textit{Equation 2-10}$$

where D_p and D_n are the diffusion coefficients of holes and electrons, respectively.

If $N_A >> N_D$, the substitution of the diffusion length of holes and electrons by $\sqrt{D \cdot \tau}$ in eq. 2-10 gives a dependence of the diffusion current on the minorities lifetime τ_p:

$$I_{dif}(0) = A \cdot q \cdot \sqrt{\frac{D_p}{\tau_p}} \cdot \frac{n_i^2}{N_D} \qquad \textit{Equation 2-11}$$

Thus, knowing the value of $I_{dif}(0)$ obtained with (I-V) curve, we can calculate the minority carrier lifetime in the neutral region τ_p with eq. 2-11.

Reverse bias

Under reverse bias the potential across the p-n junction is increased ($V_{bi}+V$), and minorities cannot overcome this barrier. Hole-electron pairs generated in the space-charge region are separated and a recombination current approximate zero. The generation rate G of the process is described as:

$$G = \frac{n_i}{\tau_g}$$

where τ_g is the effective generation time, required for the generation of electron-hole pairs.

Electrons and holes contribute to the generation component of current in the space-charge region, I_g. Hole-electron pairs generated in adjacent areas of the neutral region will diffuse towards the space charge region contributing to the diffusion current or generation in the neutral region, I_{dif}. Thus the total reverse current is the sum of I_g and I_{dif} (see Figure 2-3):

$$I = I_g + I_{dif} \qquad \textit{Equation 2-12}$$

The diffusion component does not change with the applied voltage, but the potential across the junction and the depletion width alters. The capacitance of the depletion layer varies accordingly. The dependence of depletion width, W_d, on applied voltage can be calculated with Capacitance-Voltage characteristics:

$$W_d(V) = A \cdot \frac{\varepsilon_o \cdot \varepsilon_{Si}}{C(V)} \qquad \textit{Equation 2-13}$$

Then, the dependence of current versus voltage can be obtained by combining $I(V)$ and $W_d(V)$ data. The contribution of the diffusion component to the total current can be obtained as the intercept of the

Current-Width (I-W_d) dependence with the I-axis [9]. The generation current now can be calculated with eq. 2-12. On the other hand, the generation current relates to the width of the generation layer W_i and the generation lifetime τ_g as follows:

$$I_g = I - I_{dif} = \frac{A \cdot q \cdot n_i \cdot W_i}{2\tau_g} \qquad \textit{Equation 2-14}$$

The generation layer is a part of the space-charge region, where the maximum generation occurs. W_i is located between cross-points of the intrinsic level E_i with quasi Fermi levels. This width for the p^+/n junction is defined with the following equation [10]:

$$W_i = \sqrt{\frac{2\varepsilon_S kT}{q^2 N_D}} \cdot \left[\sqrt{\ln\frac{N_D}{n_i} - \frac{qV}{kT}} - \sqrt{\ln\frac{N_D}{n_i}} \right] \qquad \textit{Equation 2-15}$$

The combination of eq. 2-14 and 2-15 gives the expression for the generation lifetime τ_g:

$$\tau_g = \frac{A \cdot q \cdot n_i \cdot W_i}{2 \cdot \left(I - I_{dif}\right)} \qquad \textit{Equation 2-16}$$

Schröder [11] showed that the generation lifetime is related to the recombination lifetime via the exponential function of the energy of the trapping center E_T:

$$\tau_g \approx \tau_r \cdot e^{\frac{|E_T - E_i|}{k \cdot T}} \qquad \textit{Equation 2-17}$$

The analysis of the equation shows that for Cu trapping centers, which have the energy band between (E_C-0.15) and (E_C-0.35) eV, the generation lifetime exceeds the recombination lifetime by $8 \cdot 10^6$ and $3 \cdot 10^3$ times respectively.

Cu serves as deep traps in the Si, therefore it leads to a decrease of the recombination-generation lifetimes and an increase of the recombination and generation current in the neutral as well in the space charge region of p-n junctions. Thus, an increase of the leakage current and the increase of forward current can be observed.

2.2.3 Capacitance-Voltage measurements

2.2.3.1 C-V measurements for diodes

Capacitance-voltage measurements give information about the doping in a diode. The built-in potential between p^+ and n-side of a junction and the depletion width can be calculated based on measurements results.

Under a reverse bias the diode capacitance equals to the capacitance of the depletion region, which expands with applied voltage. The width of the space charge region in the reverse bias is described with the following equation:

$$W_d = \sqrt{2 \cdot \frac{\varepsilon_{Si} \cdot \varepsilon_0}{q} \cdot (V_{bi} + V_a) \cdot \left(\frac{1}{N_A} + \frac{1}{N_D} \right)} \qquad \textit{Equation 2-18}$$

where V_{bi} is the built-in potential.

Rewriting of the eq.2-13 for a relation ($1/C^2$) and combination with eq. 2-18 results in the following dependence:

$$\frac{1}{C^2} = \frac{2}{\varepsilon_{Si} \cdot \varepsilon_0 \cdot q \cdot N_{eff} \cdot A^2} \cdot (V_{bi} + V_a), \qquad \textit{Equation 2-19}$$

where N_{eff} is an effective doping, which is expressed as:

$$N_{eff} = \frac{N_A \cdot N_D}{N_A + N_D} \qquad \textit{Equation 2-20}$$

Thus, the effective doping N_{eff} can be obtained from the slope of the $1/C^2$-V dependence with the relation:

$$N_{eff} = \frac{2}{A^2 \varepsilon_{Si} \varepsilon_0} \cdot \frac{1}{d\left[1/C^2\right]/dV} \qquad \textit{Equation 2-21}$$

In fact, N_{eff} is not the effective doping, but the effective carrier density, because holes and electrons, moving under the applied voltage, are actually being measured. The effective carrier density is approximately equal to the majority carrier density, therefore we continue to use the term “doping”. A built-in potential is obtained as the intersect of the ($1/C^2$-V) plot with the voltage axis. ($N_A N_D$) product can be calculated according to eq. 2-4. Then,

solving eq. 2-20 with a value of ($N_A N_D$) and N_{eff}, we can calculate apparent carrier density or doping in p-and n-region.

2.2.3.2 C-V measurements of capacitors

C-V measurements are used to calculate doping concentrations of a semiconductor, the flat-band voltage and charges in oxide and at the interface. The measurements were done with a superimposing of a small ac signal with 10 kHz frequency on a varying dc voltage applied to a gate. An HP 4140B meter was used as the dc voltage source. An HP 4275 multi-frequency meter as the ac signal source.

Normal C-V

The capacitance of MOS (Metal Oxide Semiconductor) structure is a capacitance of the oxide C_{ox} in series with a capacitance of the depletion layer C_{dep} formed in Si under applied bias V_a:

$$C = \frac{C_{ox} \cdot C_{dep}}{C_{ox} + C_{dep}} \qquad \textit{Equation 2-22}$$

There are three operational regimes of the capacitor: with the silicon surface brought into accumulation, depletion or inversion under applied voltage. A C-V curve with the regimes noted is shown with a solid line in Figure 2-4. If the Si bulk is n-type, a positive gate voltage results in the accumulation of electrons on the silicon surface. The measured capacitance in this case equals the charge in oxide of a thickness t_{ox} with the contact area A:

$$C = C_{ox} = \frac{\varepsilon_{ox} A}{t_{ox}} \qquad \textit{Equation 2-23}$$

The negative gate voltage causes the depletion of electrons in the silicon surface layer. The applied bias gives the potential drop across oxide V_{ox} and a potential drop at the Si surface ϕ_S:

$$V_a = V_{ox} + \phi_S \qquad \textit{Equation 2-24}$$

The surface potential determines the width of the depletion layer. The capacitance of the depletion layer is reciprocal to the depletion width W_{dep}:

$$C_{dep} = \frac{\varepsilon_{Si} A}{W_{dep}} \qquad \textit{Equation 2-25}$$

When the potential drop at the Si surface, ϕ_S, equals two times a bulk potential in the Si, ϕ_n, the width of the depletion region reaches maximum. The related applied voltage is called threshold voltage V_T.

The further increase of the bias results into a creation of an inversion layer in the silicon surface region. The charge in the inversion layer is governed by the generation rate of carriers in the depletion layer, which is a slow process and cannot follow a high frequency measuring signal. Thus, the relation for the measured capacitance in inversion $C_{\min}$ with eq. 2-22 and 2-25 with a maximum depletion width W_{inv} becomes

$$C_{\min} = \frac{1}{\frac{1}{C_{ox}} + \frac{W_{inv}}{\varepsilon_{Si} A}} \qquad \textit{Equation 2-26}$$

The width of the inversion layer depends on doping N_D as

$$W_{inv} = \sqrt{\frac{4\varepsilon_{si} kT \ln \frac{N_D}{n_i}}{qN_D}} \qquad \textit{Equation 2-27}$$

At very low frequencies, the charge variations in the inversion layer can follow the measuring signal, and the measured capacitance approaches the oxide capacitance. Now using C-V plot the doping density of Si can be calculated using eq. 2-26 and 2-27 by numerical methods.

Charges in oxide

A difference of work functions for the Si and metal, ϕ_{MS}, results in a potential drop across oxide and a bending of the energy band in the Si. The gate voltage, at which there is no band bending, is called a flatband voltage, V_{fb} The corresponding capacitance is called flat-band capacitance C_{fb}. At V_{fb} the effective width of the depletion layer is the distance over which the charge imbalance is neutralised by majority carriers under equilibrium conditions [12]. This distance is called Debye length L_D and expressed via N_D with the following equation:

$$L_D = \sqrt{\frac{kT\varepsilon_{Si}}{q^2 N_D}} \qquad \textit{Equation 2-28}$$

Eq. 2-22 can be written for the flat band capacitance as:

$$C_{fb} = \frac{A}{\frac{t_{ox}}{\varepsilon_{ox}} + \frac{L_D}{\varepsilon_{Si}}} \qquad \textit{Equation 2-29}$$

In practice, there are four different kinds of charges in MOS structure: fixed oxide charge, oxide trapped charge, mobile charge in oxide and interface states charges. The last two are influenced by an applied voltage.

To account for the distribution of charges throughout an oxide, a body factor for the oxide γ_{ox} is introduced:

$$\gamma_{ox} = \frac{\int_0^{t_{ox}} (x/t_{ox})\rho(x)\cdot dx}{\int_0^{t_{ox}} \rho(x)\cdot dx} \qquad \textit{Equation 2-30}$$

The body factor equals 0 for a charge located at the gate-SiO_2 interface, and 1 at the SiO_2-Si.

Charges result in a potential drop across the dielectric, contributing to V_{fb}. The relation of flatband voltage with ϕ_{ms}, potential drops in oxide due to a mobile charge Q_m, fixed charge Q_f, trapped charge Q_t and charge due to interface states Q_{it} is given by:

$$V_{fb} = \phi_{ms} - \gamma_{ox}\frac{Q_m}{C_{cx}} - \frac{Q_f}{C_{ox}} - \gamma_{ox}\frac{Q_t}{C_{ox}} - \frac{Q_{it}}{C_{ox}} \qquad \textit{Equation 2-31}$$

Figure 2-4 demonstrates the deviations of C-V plots from ideal curve without any charges. The oxide charges produce a parallel shift of the line. The shift of flatband voltage, correlated with the total charge Q_{total}, is shown with a dotted line.

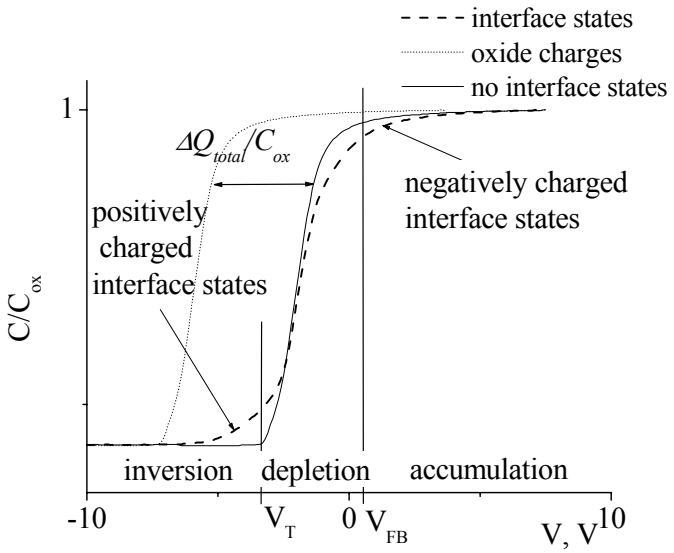

Figure 2-4. C-V plot demonstrating the effect of oxide charges and interface states. Regions of inversion, depletion and accumulation are assigned to a device without interface states.

The dashed line illustrates the effect of interface states. The C-V plot is smeared along the voltage axis. The interface states are characterised usually with an energy level close to the intrinsic level in the Si band gap. As a result, if the Fermi level changes at the interface, the charge of the interface states alters. Thus, in n-Si the interface states are negatively charged or neutral. In inversion the states are positively charged and the C-V curve shifts to a lower voltage. In depletion the interface charge is negative and the curve is shifted to a higher voltage.

A density of interface states D_{it} can be calculated by the Terman method. At first, a surface potential versus applied voltage is calculated for the ideal case (D_{it}=0) and for the measured capacitance (D_{it}#0). Then, a voltage shift ΔV_a, obtained at the same surface potential ϕ_S, can be plotted versus the surface potential. A slope of this dependence [$d(\Delta V_a)/d\phi_S$] is proportional to the density of the interface charges as follows:

$$D_{it} = \frac{C_{ox}}{q} \cdot \frac{d(\Delta V_a)}{d\phi_S} \qquad \textit{Equation 2-32}$$

This method is useful for measuring densities above 10^{10} cm^{-2}.

Effect of copper charges

Cu drifts in SiO_2 as Cu^+ under an applied electrical field at elevated temperatures. A density of mobile charge can be obtained from the flatband voltage shift after bias-temperature stress (BTS). At room temperature copper ions are considered to be immobile. However, when the copper charge is located at the gate/SiO_2 interface, it images the charge in the gate and does not effect the flatband voltage. When Cu ions diffuse towards the SiO_2/Si interface, the charge will image in the Si, giving a change of V_{fb}.

When a barrier failed, Cu will diffuse fast in the Si wafer, but slow in the SiO_2. As a result, changes in C-V characteristics can occur even without Cu^+ ions diffused through SiO_2, if there are neighboring devices with a Cu contact to Si. Thus, devices for testing the barrier performance on Si (diodes) and on SiO_2 (capacitors) must be made on separate wafers.

2.2.4 Capacitance-time measurements

Capacitance-time measurements are used for the extraction of the generation lifetime τ_g [12]. The test is performed on a capacitor pumped into deep depletion. The capacitance (depletion width) changes in time. How fast the capacitance is changing depends on the thermal generation of electron-hole pairs. Results of the measurements are usually plotted as a Zerbst plot using the following relation:

$$-\frac{d}{dt}\left(\frac{C_{ox}}{C}\right)^2 = \frac{2n_i}{\tau_g N_D}\cdot\frac{C_{ox}}{C_{inv}}\left(\frac{C_{inv}}{C}-1\right)+\frac{2n_i s}{N_D t_{ox}}\cdot\frac{\varepsilon_{ox}}{\varepsilon_{Si}}, \qquad \textit{Equation 2-33}$$

where s is the surface generation velocity.

The vertical axis of the Zerbst plot is $-d(C_{ox}/C)^2/dt$ and proportional to the generation current. The horizontal axis is $(C_{inv}/C-1)$ and proportional to the generation width of the space charge region. The deviation of the dependence from the straight line at the beginning is due to the fact that equilibrium has not been reached yet. The plot can be curved at the end, because of field-enhanced emission from interface or the bulk traps. The slope of the straight part of the plot is $2n_iC_{ox}/N_DC_{inv}\tau_g$. Thus generation lifetime τ_g is reciprocal to the slope.

2.2.5 Triangular Voltage Sweep measurements

TVS is used to measure mobile ions in oxide at elevated, constant temperature in air environment [12]. Initially, the electrical field applied to the capacitor pushes mobile ions through a barrier and oxide towards the SiO_2/Si interface. Then an inverse applied bias forces the mobile ions to drift backwards. The corresponding current is measured. Applied bias V_a is changing in time t with a constant ramp α as following:

$$V_a(t) = V_a(0) + \alpha \cdot t \qquad \textit{Equation 2-34}$$

An example of the *I-V* curve is presented in Figure 2-5. The measured current is the sum of displacement current I_c and current due to mobile ions I_m. The displacement current is proportional to the capacitance C and given by:

$$I_C = \frac{dQ}{dt} = \frac{dQ}{dV_a} \cdot \frac{dV_a}{dt} = C \cdot \alpha \; ; \qquad \textit{Equation 2-35}$$

where Q includes all charges except mobile.

The current due to mobile ions is related to the charge of mobile ions Q_m

$$I_m = \frac{dQ_m(t)}{dt} \qquad \textit{Equation 2-36}$$

If several peaks are observed in the curve, they are attributed to ions with different mobility. High mobility ions move at a lower electrical field than low mobility ions. As a result, a peak for ions with a high mobility (Na^+, for example) appears at lower bias than a peak for Cu^+ ions. The number of mobile ions corresponds to the area of the peak based on a level of displacement current. The peak for Cu^+ ions is expected to be at about 1 MV/cm when measured at 250-300 ^oC [6, 13].

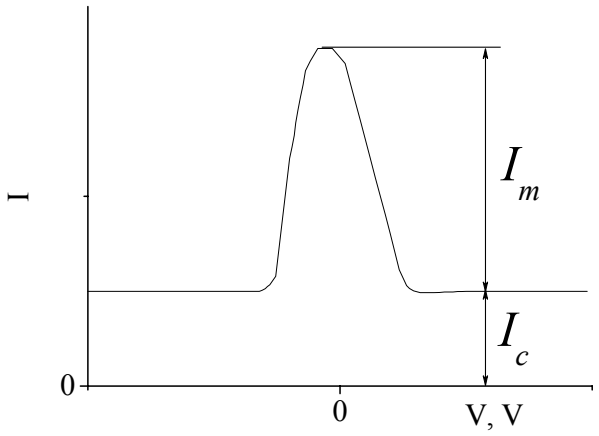

Figure 2-5. Illustration of the TVS method.

2.3 Test structures

2.3.1 Structures for resistance measurements

Van der Pauw structures

Van der Pauw structures were designed for the sheet resistance measurements of the Si bulk and metal contact on SiO_2 (see Figure 2-6). Three different designs are available, see Table 2-1: an uncovered van der Pauw structure (P1), a structure with the metal contact to the Si-bulk (P2) and SiO_2 (P3). The structure P1 is used to measure sheet resistance after the processing as a reference. The metal covered structure is designed to measure a change in sheet resistance when copper ions have diffused through the barrier material into the Si (P2) and oxide (P3) or changes in the metallization stack of barrier/Cu.

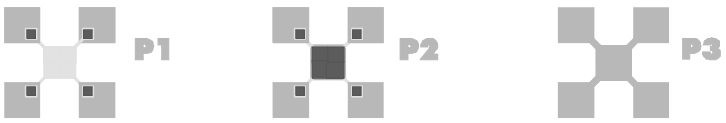

Figure 2-6. Van der Pauw structures.

Table 2-1. Description of van der Pauw structures.

Idi	SiO_2 LOCOS	Boron implanted SiO_2	barrier/ Cu	remarks	
P1	no	yes	no	p+Si/50nm SiO_2	to measure changes in Si bulk
P2	no	yes	yes	p+Si/ Me	to measure changes in Si / Me stack
P3	yes	yes	yes	nSi/ SiO_2/ Me	to measure changes in Cu/barrier on oxide

2.3.1.1 Four-point probe measurements

Stacks with the Cu/barrier metallisation on SiO_2(700 nm)/Si substrate are used for sheet resistance measurements in- situ. The schematic of the tested combination is shown in Figure 2-7. The thickness of the Cu layer was 200 nm or 100 nm.

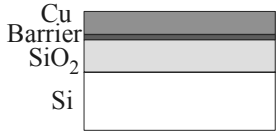

Figure 2-7. Schematic presentation of a structure for the four-point probe measurements.

2.3.2 Diodes

I-V and C-V measurements were performed on diodes before and after an annealing treatment in forming gas (N_2/5% H_2). Tests results were used to calculate changes in minority lifetime. Two series of diodes were designed: one with one contact opening for devices with an area between $1 \cdot 10^{-4}$ and $2.56 \cdot 10^{-2}$ cm^2 (D1-D5) and the other for the large active area of $2.56 \cdot 10^{-2}$ cm^2 with a varying area of contacts openings (DS1-DS3, DL1-DL3). Examples of the openings of a different geometry with equal active area are shown in Figure 2-8.

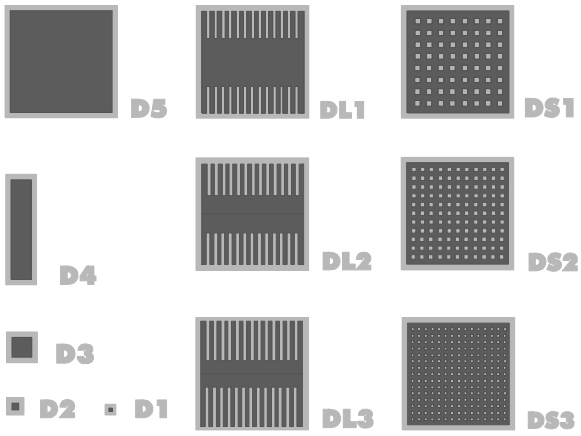

Figure 2-8. Diodes with different geometry of the contacts openings.

2.3.3 Capacitors

C-V, C-t and TVS measurements were applied to calculate the amount of charges in oxide and detect Cu penetrating the SiO_2/Si interface.

Capacitors with a different area to perimeter ratio (C1-C5) were designed and presented in Figure 2-9. The devices were manufactured on Si with 200 nm thermal oxide. A Cu metallisation on barrier was used as a gate electrode. References with the Al metallisation on barriers were also made. The area of electrode varies from $1 \cdot 10^{-4}$ to $2.56 \cdot 10^{-2}$ cm^2 for C1 and C5 capacitors, respectively.

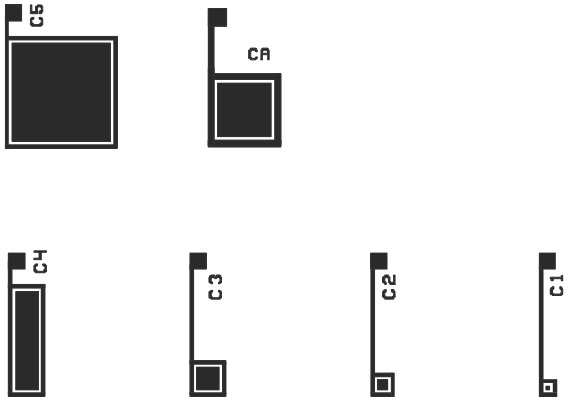

Figure 2-9. Capacitors test structures.

2.4 Experimental details

Diodes and capacitors were manufactured on individual wafers, thus two groups of wafers and process flows were used.

2.4.1 Diode process flow

(100) n-type Si 3 and 4 inch wafers with a bulk resistivity 1-10 Ω·cm were used. The process sequence is shown in Figure 2-10. After 700 nm field oxide was grown, the active areas were defined and protected with 50 nm sacrificial oxide. A shallow p^+ channel was fabricated with BF_2^+

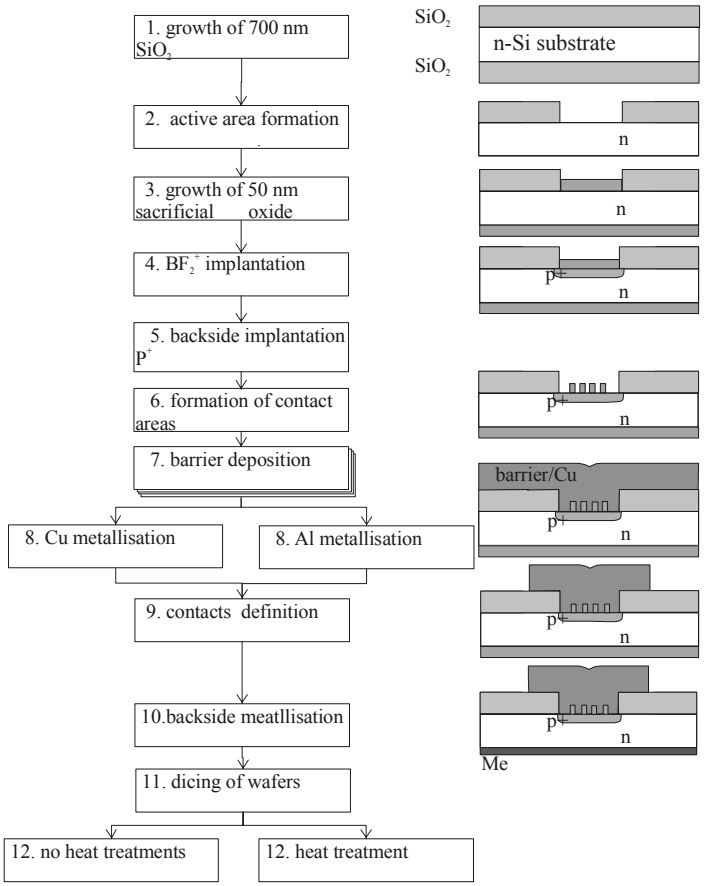

Figure 2-10. Process overview for the fabrication of the test structures.

ion implantation (70 keV-$2x10^{15}$ at/cm^2). The following backside implantation with P^+ (100 keV-$8x10^{15}$ at/cm^2) resulted in a gettering n^+ layer. Removal of the implantation damage was preformed at 900 ^oC in inert N_2 atmosphere for 1 hour. The p^+/n junction was formed at a depth of 0.25 μm. Then the contacts holes were etched in a buffered HF solution (1 HF:6 NH_4F) for 3 min. Before barrier deposition the wafers were dipped in 0.3 % HF for 3 min. After a barrier was grown, the wafer was transferred into a sputtering equipment to deposit Cu or Al-reference samples. Metal contacts to devices were defined by photolithography and

wet etching: for Cu 5 % HNO_3 and for Al a solution of H_3PO_4: CH_3OOH: HNO_3 was used. The barrier was etched in a CF_4/O_2 plasma. After the front side of the wafer was protected with photoresist, oxide on the backside of the wafer was etched off in a buffered HF solution. An Al layer was deposited on the backside and the photoresist was removed in fuming HNO_3.

The fabricated wafers were diced in quarters and annealed at different temperatures before electrical testing. Van der Pauw test structures were made with the same process flow.

2.4.2 Capacitor process flow

(100) n-type Si 3 inch (*Chapter 5*) and 4 inch (*Chapter 6*) wafers with a bulk resistivity 1-10 Ω·cm were used. The process sequence for a making capacitors does not include steps 2−6 in Figure 2-10. During the 1st step a silicon thermal oxide layer with a thickness of 195 nm (*Chapter 6*) or 700 nm (*Chapter 5*) was grown in water vapour. Afterwards, wafers were annealed at 450 ^oC for 30 min in wet N_2 atmosphere to remove states at the SiO_2/Si interface. The further procedure is identical to the one for diodes.

References

1. H. Ono, T. Nakano and T. Ohta, Diffusion Barrier effects Against Cu of W-N Layer Formed by Electron Cyclotron Resonance Plasma Nitridation on W Layer, *Jpn, J. Appl. Phys*., Vol. 34, p. 1827-1830 (1995).
2. M. T. Wang, Y. C. Lin, J. Y. Lee, C. C. Wang, and M. C. Chen, Effective Improvement on Barrier Capability of Chemical Vapor Deposited WSi_x Using N2 Plasma Treatment, *J. Electrochem. Soc*., 146 (4), p. 1583-1592 (1999).
3. J. S. Reid, E. Kolawa, R. P. Ruiz and M.- A. Nicolet, Evaluation of amorphous (Mo, Ta, W)-Si-N diffusion barriers for <Si>/Cu metallizations, *Thin Solid Films*, 236, p. 319-324 (1993).
4. M. T. Wang, Y. C. Lin, and M. C. Chen, Barrier Properties of Very Thin Ta and TaN Layers Against Copper Diffusion, *J. Electrochem. Soc*., Vol. 145 (7), p. 2538-2545 (1998).
5. S. C. Sun, M. N. Tsai, H. T. Chiu, and S.H. Chuang, A New CVD Tungsten Nitride Diffusion Barrier for Cu, *Interconnection Symposium on VLSI Technology Digest of Technical Papers*, p. 46-47 (1996).

6. J. Cluzel, F. Mondon, D. Blachier, Y. Morand, L. Martel and G. Reimbold, Electrical characterization of copper penetration effects, *Annual Proceedings - Reliability Physics (Symposium)*, p 431-432 (2002).
7. C. Ahrens, G. Friese, R. Ferretti, B. Schwierzi, W. Hasse, Electrical characterization of $TiN/TiSi_2$ and $WN/TiSi_2$ Cu diffusion barriers using Schottky diodes, *Microelectronic Engineering*, 33, p. 301-307 (1997).
8. R. Sachedeva, A. A. Istratov, and E. R. Weber, Recombination activity of copper in silicon, *Appl. Phys. Lett*., Vol. 79, N 18, p. 2937-2939 (2001).
9. Y. Murakami and T. Shihgyouji, Separation and analysis of diffusion and generation components of pn junction leakage current in various silicon wafers, *J. Appl. Phys.*, V.75 (7), p. 3548-3552 (1994).
10. R. S. Muller and T. I. Kamins, Device electronics for integrated circuits, ISBN 0-471-88758-7.
11. D. K. Schröder, J.M. Hwang, J.S. Kang, A.M. Goodman, B.L.Sopori, Lifetime and recombination concepts for oxygen-precipitated silicon, *Proceedings of the Third International Symposium on Very Large Scale Integration Science and Technology. VLSI Science and Technology/1985*, p. 419-428 (1985).
12. D. K. Schröder, Semiconductor material and device characterization, ISBN 0-471-24139-3.
13. G. W. Book, K. Pfeifer, S. Smith, Barrier integrity testing of Ta using triangular voltage sweep and a novel CV-BTS structure, *Microelectronic Engineering*, 64, p. 255-260 (2002).

Chapter 3

Thermodynamics

3.1 Introduction

Thermodynamic calculations are commonly used to describe chemical vapor deposition (CVD) processes. They can be used to predict the formation of a solid phase and products in the gas phase. Parameters like temperature and partial pressure of the gaseous species along with thermochemical data are used as input.

The conditions of thermodynamic equilibrium (when a system is characterised by a minimal Gibbs free energy) can be determined as a result of the thermodynamic calculations. The Gibbs free energy for a system, which consists of n_{gas} gaseous species and n_s solid species is given by:

$$G = \sum_{i}^{n_{gas}} \left(n_i \Delta G^{o}_{gas} + RT \ln P + 2T \ln \frac{n_i}{N_{gas}} \right) + \sum_{j}^{n_s} n_j \Delta G^{o}_{s} \qquad \textit{Equation 3-1}$$

where n_i and n_j are the number of moles of gaseous species and solid species, respectively; N_g the total number of moles of gaseous species; P total pressure;
$\Delta G_{gas}{}^{o}$, $\Delta G_s{}^{o}$ is the Gibbs free energy at standard pressure of gaseous and solid species, respectively. This is defined by the enthalpy of the species i (or j) $\Delta H^{o}{}_i$ and entropy $S^{o}{}_i$ at temperature T as follows:

$$\Delta G^{o}_{i} = \Delta H_i{}^{o} - T \Delta S_i{}^{o} \qquad \textit{Equation 3-2}$$

where $\Delta H^{o}{}_i$ and $S^{o}{}_i$ are dependent on the heat capacity of the species i, $c_p{}^{i}$, which changes non-linearly with temperature (see Appendix). The thermodynamic calculations aim to obtain the set of n_i and n_j such that the Gibbs free energy has a minimum value. For a system with multiple species this optimization can be done effectively only by a computing program. In this case the accuracy of the calculations depends on the

availability of the thermochemical data and their quality for all possible species in the system.

In this study the thermodynamical calculations were performed with a thermochemical code called "ChemSage" [1]. This code uses a data base of the Scientific Group Thermodata Europe (SGTE) bank. Data for tungsten nitride species were selected carefully from available literature [2]. Some lacking data for carbon containing species were obtained from literature additionally [3, 4]. Thermodynamical properties such as entropy (S_{298}^{o}), enthalpy (ΔH_{298}^{o}) at standard pressure, and temperature, and specific heat capacity at constant pressure (c_p) or $\Delta G(T)$ are listed in Table A in the Appendix.

3.2 Thermodynamic calculations

Not much is known about the deposition conditions of LPCVD $W_xSi_yN_{1-x-y}$ layers. An experimental study of the system WF_6-NH_3-Si_2H_6-H_2-N_2-Ar and WF_6-NH_3-H_2 showed that WF_6 reacts with NH_3 even at low temperatures with formation of solid adducts such as NH_4F [5] and/or $WF_6{\cdot}NH_3$ [6]. In order to eliminate gas phase reactions and adducts formation, NH_3 was replaced by NF_3 in this research. WF_6 and SiH_4 were used as precursors of W and Si, respectively. There is a limitation on the N and Si content in the films. The nitrogen content should be kept lower than the W content, N/W< 1 [7] in order to obtain a material with a low resistivity [5]. The silicon content must be low to avoid a reaction between Si and Cu. $W_xSi_yN_{1-x-y}$ compounds with a Si/W ratio of 1.5 are reported as good diffusion barriers [8]. The thermodynamic calculations for the system WF_6-NF_3-SiH_4-Ar must be done to obtain input for the gas flow ratio's of precursors resulting in the deposition of compounds with an appropriate composition to act as diffusion barrier. The results are presented in *Section* 3.2.1.

The sequence of precursors for the ALD (Atomic Layer Deposition) process of $W_xC_yN_{1-x-y}$ compounds using WF_6, NH_3, TEB (triethyl borane, $(C_2H_5)_3B$) has already been established [9]. The ALD process of the same compound but using precursors such as WF_6, NH_3, and C_2H_4 is being studied for the first time. The ALD process is based on a cycling sequence of different precursors separated by inert gas (N_2) and each precursor

chemisorbs on a surface of a growing film (see Chapter 6, Introduction). However, we do not know what species are formed as a result of chemisorption. Moreover, no data on these species (WF_x^*, SiH_x^*, etc.) are available. That is why in this case the thermodynamic calculations can be used only to suggest a probable outcome of the reactions between two precursors.

3.2.1 CVD of $W_xSi_yN_{1-x-y}$

Figure 3-1 shows the results of the thermodynamical calculations for a varying mole ratio of SiH_4 and WF_6 at 385°C. The amount of WF_6 was fixed to 1 mole, the amount of NF_3 to zero. Growth of W takes place up to a SiH_4/WF_6 ratio of 1.5. At larger ratio's the formation of the W_5Si_3 phase is predicted in parallel to the W growth. The very small increase of a SiH_4/WF_6 ratio from 1.5 up to 2.1 results in a growth of WSi_2 phase in addition to W_5Si_3. Thus, the Si content in the product is strongly dependent on the ratio of SiH_4 to WF_6. This trend was confirmed experimentally by Schmitz [10]. The majority of gas species formed during the process were SiF_4, H_2 and HF (see Figure 3-1). The formation of HF, however, was not detected by experimental studies. Here SiF_4, H_2 [11] and $SiHF_3$ [12] were mainly found in the gas phase.

Figure 3-2 and Figure 3-3 show the calculated equilibrium amount of species versus mole ratio of SiH_4/WF_6 at 385 °C with 0.5 and 1 mole of NF_3, respectively. Tungsten nitrides are not formed, because they are unstable under the studied conditions from a thermodynamics point of view. This is due to the fact that the thermodynamic functions for W-nitrides are available for the high- pressure region (10-200 bar) only [2]. Despite this fact, for the WF_6-NF_3-SiH_4-Ar system it was still useful to evaluate partial pressures of species in the gas phase and to predict the possible regimes for deposition of compounds with a certain composition. As can be seen, the amounts in Figure 3-1, Figure 3-2 and Figure 3-3 are rather similar exept that curves are shifted along the x- axes towards larger ratio of SiH_4/WF_6. The Si content in the material formed is also strongly dependent on the ratio of SiH_4 to WF_6. At low SiH_4/WF_6 ratio the addition of NF_3 leads to an increase of HF formation in the gas phase.

The situation at 250 ^{o}C is somewhat different. At SiH_4/WF_6<1.1 at 250 ^{o}C the calculations predict the formation of WF_4-solid adduct. With the input ratio of SiH_4/WF_6>1.1 the outcome of the reaction is the same as at 385 ^{o}C.

In order to satisfy the requirement on Si content (see 3.2) the layers should be rich in W and should contain Si with a ratio of Si/W<1.5 [8]. That is a W-Si-N compound, which consists of W, W_5Si_3, and Si_3N_4 phase. This material may be formed at equilibrium conditions at SiH_4/WF_6=3÷3.6, if NF_3=WF_6=1 mol (see dashed area in Figure 3-3).

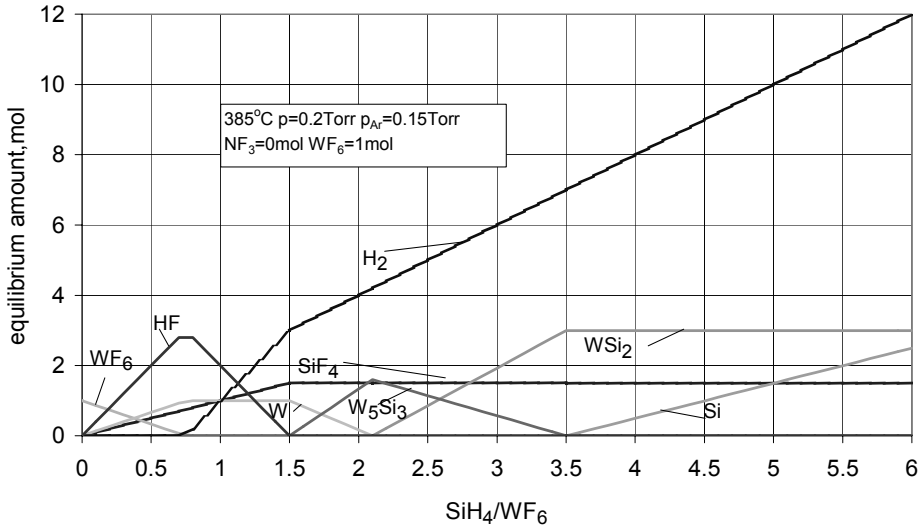

Figure 3-1. The equilibrium amount of the species versus mole ratio of SiH_4/WF_6 at 385 ^{o}C and a total pressure of 0.2 Torr. Partial pressure of Ar is 0.15 Torr. Input amount of WF_6 and NF_3 is 0 mol.

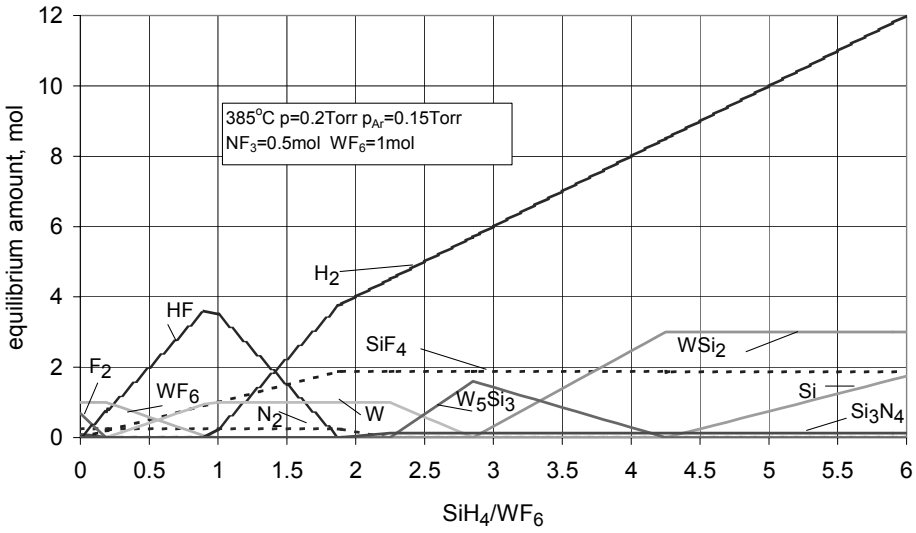

Figure 3-2. The equilibrium amount of the species versus mole ratio of SiH_4/WF_6 at 385 ^oC and a total pressure of 0.2 Torr. Partial pressure of Ar is 0.15 Torr. Input amount of WF_6 and NF_3 is 0.5 mol.

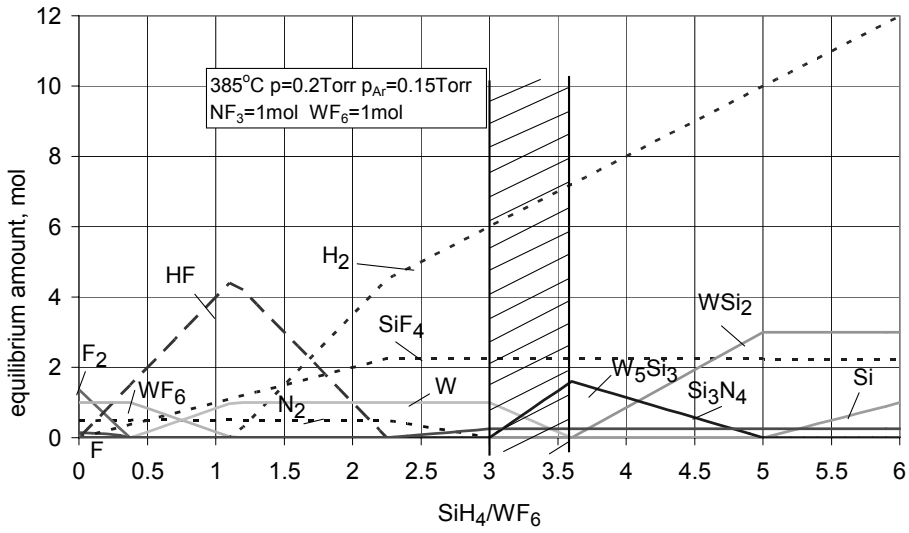

Figure 3-3. The equilibrium amount of the species versus mole ratio of SiH_4/WF_6 at 385 ^oC and a total pressure of 0.2 Torr. Partial pressure of Ar is 0.15Torr. Input amount of WF_6 and NF_3 is 1 mol. Dashed area indicates the range of flow ratio's for the products with the Si-content allowed.

3.2.2 ALD of $W_xC_yN_{1-x-y}$

Growth experiments were performed in parallel to the thermodynamic calculations. Initially a sequence of $WF_6/C_2H_4/NH_3$ was studied.

When the pulse of C_2H_4 is introduced, two reactions can take place: between C_2H_4 and W or C_2H_4 and WF_6 (used in the calculations instead of WF_x). Both reactions result in the formation of WC and C:

$$W + xC_2H_4 = WC + 1.91x\,C + 1.82x\,H_2 + 0.089x\,CH_4 \quad \textit{Equation 3-3}$$

$$WF_6 + xC_2H_4 = WC + (1.93x-0.83)\,C + (1.86x-2.66)H_2 + (0.07x-0.17)CH_4 + 6HF \quad \textit{Equation 3-4}$$

with $x > 2$

In the gas phase mainly HF, H_2 and CH_4 are present in equilibrium. Minor amounts of the species CF_4, CH_3F, i.e. $\sim 10^{-10}$ Torr are found.

The results of experiments with a cycling sequence of $WF_6/C_2H_4/NH_3$ showed no film growth (*Chapter 6 ALD Table 6-2, p. 116*) at 350 °C. This disagreement with the results of the calculations can be explained either by the thermochemical data used (e. g. for WF_6 instead of WF_x), resulting in a wrong ΔG (see eq.3-1, 3-2) or by the kinetics of the growth process. In the last case it could be that either the real conditions during the growth do not allow a reaction to take place or a reaction takes place, but stops when W or WC is passivated. Most probably, the growing surface is passivated with CH_2^* species, which are present after decomposition of C_2H_4 on the W surface [13].

Considering that WF_6 reacts with NH_3 with a growth of tungsten nitride [14], a cycling sequence of $WF_6/NH_3/C_2H_4$ was tried. The obtained films were hardly continuous. It can be that either CH_2^* or some products of reaction between CH_2^* and WF_6 decrease the amount of reactive sites available for a continuous growth. These products can be compounds with C-F bonds, for example CF_4 or CH_3F, which were predicted to be stable thermodynamically.

Removal of these species could enable further reaction. SiH_4 was introduced to promote further growth, because it forms with fluorine a

volatile SiF_4 or $SiHF_3$ and with carbon $SiCH_3F_3$. The thermodynamic calculations were performed, assuming that products of the reaction between WF_6 and C_2H_4, i. e. CF_4, CH_3F, C and SiH_4, are present as input. Figure 3-4 shows the equilibrium amounts of species calculated for this case. The equation for the reaction between CF_4, CH_3F and SiH_4 is written as:

$$0.5\ CF_4 + 0.5\ CH_3F + 0.5\ C + xSiH_4 = 1.5\ \beta SiC + (x-2.13)Si + (2x+0.75)H_2 + 0.62\ SiF_4 \qquad \text{Equation 3-5}$$

for x> 2.1.

H_2 and SiF_4 are obtained mainly in the gas phase with formation of βSiC and Si. For x< 2.1 it is possible to form CH_4 and a small amount of $SiCH_3F_3$ phase at a pressure less than 10^{-10} Torr.

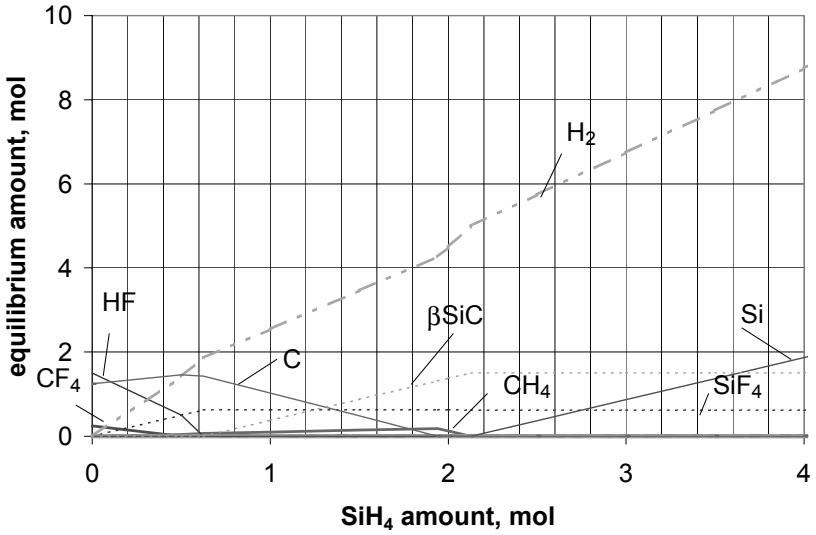

Figure 3-4. The equilibrium amount of species versus the amount of SiH_4 at 350°C and a total pressure of 0.75 Torr. Input amount of CF_4, CH_3F and C is 0.5 mole.

Experiments showed that the sequence of $WF_6/NH_3/C_2H_4/SiH_4$ resulted in the growth of continuous films, which did not contain carbon and Si. Moreover, virtually no fluorine was found in the film. Whereas in tungsten nitride grown with a sequence of WF_6/NH_3 [15] concentrations of F were found up to 4 at%. This indicates that NH_3 alone can not reduce all F-bonds. In our case fluorine was removed along with carbon and silicon.

This suggests that the formation of CHF_3, $SiCH_3F_3$ or SiF_4 or other species containing Si, C and F is preferred to the formation of βSiC, as predicted with thermodynamics. It could also be that or the calculations resulted in a wrong ΔG due to the thermochemical data used (see above).

Thus, in the case of the ALD the thermodynamic calculations with available data are not suitable for (qualitative) analysis of the process.

3.3 Summary and conclusions

For the deposition of the ternary compounds of $W_xSi_yN_{1-x-y}$ in the WF_6-SiH_4-NF_3-Ar system the thermodynamic calculations show no formation of tungsten nitrides. This result is, however, due to the available thermodynamic data obtained for a high pressure range.

The stoichiometry of the predicted compounds (Si content) is strongly influenced by the ratio of SiH_4/WF_6 in the temperature range of 250-385^{o}C. In order to deposit W-compounds containing a small amount of Si a flow ratio of SiH_4 to WF_6 should be kept in the narrow range between 3 and 3.6.

Thermodynamic calculations for the ALD process of the $W_xC_yN_{1-x-y}$ compound were performed in parallel with the growth experiments. The disagreement between thermodynamics and growth kinetics can be explained either by replacement of WF_x chemisorbed species by WF_6 in the calculations or by the kinetics of the growth process. The calculations with available data are not suitable for qualitative analysis of the process.

References

1. GTT- ChemSage, Thermochemical Software, 1998.
2. A. F. Guillermet and S. Jonsson, Thermodynamic Analysis of Stable and Metastable W Nitrides and Calculation of the W-N Phase Diagram, *Z. Metallkd*., 84 iss. 2, p. 106-117 (1993).
3. M. W. Chase et al., Janaf thermochemical tables, Washington, DC: American Chemical Society, 1986, ISBN: 0-88318-473-7.
4. I. Barin and O. Knacke, Thermochemical properties of inorganic substances, Berlin: Springer-Verlag, 1973, ISBN: 0-387-06053-7.

5. J. G. Fleming et al., Growth and properties of W-Si-N diffusion barriers deposited by chemical vapor deposition, *Thin Solid Films*, 320 p. 10-14 (1998).
6. T. Nakajiama,K. Watanabe and N. Watanabe, Preparation of Tungsten Nitride Film by CVD Method Using WF_6, *J. Electrochem. Soc.*, 134(12), p. 3175-3178 (1987).
7. B.S. Suh, Y. J. Lee, J. S. Hwang and C. O. Park, Properties of reactively sputtered WN_x as Cu diffusion barrier, *Thin Solid Films*, 348, p. 299-303 (1999).
8. J.S. Reid, E. Kolawa, R.P. Ruiz and M.- A. Nicolet, Evaluation of amorphous (Mo, Ta, W)-Si-N diffusion barriers for <Si>/Cu metallizations, *Thin Solid Films*, 236, p. 319-324 (1993).
9. W.-M. Li, K.-E. Elers, J. Kostamo, S. Kaipio, H. Huotari, M. Soininen, P. J. Soininen, M. Tuominen, S. Haukka, S. Smith, and W. Besling, Deposition of WNxCy thin films by ALCVD™ method for diffusion barriers in metallization, *Proceedings of the IEEE 2002 International Interconnect Technology Conference*, 3–5 June, 2002, CA IEEE, New York, p. 191-193 (2002).
10. J. E. J. Schmitz, M. J. Buiting and R. C. Ellwanger, Study of the SiH_4-WF_6 chemistry used in selective W deposition, in Tungsten and other Refractory Metals for VLSI Applications IV, edited by R. S. Blewer and C. M. McConica. MRS, Pittsburg, PA, p.27- 33, 1989, ISBN 093 1837 987.
11. M. L. Yu et al. in Tungsten and other Refractory Metals for VLSI Applications IV, edited by R. S. Blewer and C. M. McConica. MRS, Pittsburg, PA, 1989, p.221, ISBN 093 1837 987.
12. N. Kobayashi, H. Goto, M. Suzuki, Study on mechanism of selective chemical vapor deposition of tungsten using in situ infrared spectroscopy and Auger electron spectroscopy, *J.Appl. Phys*. 69, p. 1013-1019 (1991).
13. G. Robertshaw and P. J. Estrup, Kinetics of thermal desorption and thermal conversion of adsorbates: AES studies, *J. Vac. Sci. Technol*. 15(2), p. 554-558 (1978).
14. J. W. Klaus, S. J. Ferro and S. M. George, Atomic layer deposition of tungsten nitride films using sequential surface reactions, *J. Electrochem. Soc.*, Vol. 147, N 3, p. 1175-1181 (2000).
15. K.- E. Elers, V. Saanila, P. J. Soininen, W.- M. Li, J. T. Kostamo, S. Haukka, J. Juhanoja and W. F. A. Besling, Diffusion Barrier Deposition on a Copper Surface by Atomic Layer Deposition, *Chem. Vap. Deposition*, 8, No. 4, p. 149-153 (2002).

APPENDIX

A standard heat capacity was described with a polynomial equation as given:

$$C_p = A + B \cdot T + C \cdot T^2 + \frac{D}{T^2} \qquad \textit{Equation 3-6}$$

Gibbs free energy was described as:

$$G(T) = A + B \cdot T + C \cdot T \cdot \ln T + D \cdot T^2 + E \cdot T^3 + \frac{F}{T} \qquad \textit{Equation 3-7}$$

Table A. Thermodynamical properties of gas species included in calculations.

species	ΔH_{298}^{o}, Jmole^{-1}	S_{298}^{o} J K^{-1}mol^{-1}	$C_{p,}$ J K^{-1}mol^{-1}			
			A	B	C	D
Ar	0	154.84	20.786			
F	79380	158.75	23.591	-3.88E-03	1.52E-06	1.65E+04
F2	0	202.79	29.085	1.49E-02	-6.97E-06	-1.44E+05
FH	-273300	173.77	29.954	-3.15E-03	3.38E-06	-1.55E+04
F2H2	-572664	238.85	33.652	5.28E-02	-2.28E-05	-2.23E+05
F3H3	-879100	288.46	75.002	4.94E-02	-1.43E-05	-1.12E+06
F4H4	-1183820	349.21	105.534	6.60E-02	-1.91E-05	-1.50E+06
F5H5	-1489710	408.44	136.073	8.24E-02	-2.38E-05	-1.89E+06
F6H6	-1807660	466.42	169.970	9.05E-02	-2.32E-05	-2.39E+06
F7H7	-2102540	523.43	201.065	1.06E-01	-2.71E-05	-2.79E+06
FHN	112000	230.80	25.432	3.55E-02	-1.32E-05	3.42E+04
CFN	35980	225.40	31.390	4.29E-02	-1.89E-05	0.00E+00
FH2N	-75000	229.53	14.867	7.09E-02	-2.48E-05	2.38E+05
F2HN	-103000	252.81	24.093	8.16E-02	-3.71E-05	-1.57E+05
C2F3N	-495390	298.53	38.460	1.60E-01	-7.94E-05	0.00E+00
FHSi	-162657	238.69	31.047	3.36E-02	-1.16E-05	-2.01E+05
FH3Si	-376560	238.40	21.110	1.15E-01	-4.86E-05	-3.51E+05
F2H2Si	-790776	262.13	33.250	1.08E-01	-4.94E-05	-6.04E+05
F3HSi	-1200810	277.27	47.487	9.66E-02	-4.76E-05	-7.61E+05
FN	232990	213.02	25.144	2.04E-02	-9.55E-06	-1.44E+04
F2N	34421	249.63	33.319	4.48E-02	-2.34E-05	-3.17E+05
F2N2_CIS	62030	266.50	41.659	6.98E-02	-3.49E-05	-4.49E+05
F2N2_TRANS	67311	262.10	40.183	7.18E-02	-3.57E-05	-4.47E+05
F3N	-131700	260.82	39.012	8.82E-02	-4.91E-05	-6.60E+05
F4N2_GAUCH	-20549	315.02	78.034	1.00E-01	-5.30E-05	-1.32E+06
F4N2_TRANS	-23001	308.99	68.234	1.27E-01	-7.28E-05	-1.25E+06
FSi	-25232	225.79	30.976	1.11E-02	-5.08E-06	-1.05E+05
F2Si	-592838	256.58	41.001	3.18E-02	-1.70E-05	-3.97E+05
F3Si	-996437	279.70	53.734	5.39E-02	-2.87E-05	-7.61E+05
F4Si	-1615000	282.76	63.600	8.00E-02	-4.19E-05	-8.99E+05
FW	386000	254.22	34.654	2.32E-03	1.34E-06	-2.64E+05
F2W	-86000	275.86	53.023	1.59E-02	-7.69E-06	-5.22E+05

F3W	-507000	310.16	69.398	2.48E-02	-1.28E-05	-1.03E+06
F4W	-929000	344.80	99.206	1.23E-02	-3.70E-06	-1.13E+06
F5W	-1293000	365.00	104.462	6.33E-02	-3.39E-05	-1.32E+06
F6W	-1721720	341.12	109.302	1.10E-01	-7.22E-05	-1.47E+06
H	217999	114.72	20.786	0.00E+00	0.00E+00	0.00E+00
H2	0	130.68	31.357	-5.52E-03	4.48E-06	-1.13E+05
HN	358433	181.22	29.254	-2.27E-03	4.32E-06	2.12E+04
HN3	294000	239.33	31.620	5.72E-02	-2.10E-05	-2.30E+05
H2N	190000	194.99	27.174	1.66E-02	-3.01E-07	1.58E+05
H2N2_1	283962	228.23	11.294	7.92E-02	-3.04E-05	3.58E+05
H2N2_CIS	247885	218.43	10.046	7.71E-02	-2.66E-05	4.21E+05
H2N2_TRANS	211859	218.33	8.430	7.96E-02	-2.79E-05	4.77E+05
H3N	-45940	192.77	21.218	4.57E-02	-1.08E-05	1.53E+05
H4N2	95180	238.46	9.501	1.45E-01	-6.57E-05	1.34E+05
HSi	368636	198.05	23.285	1.43E-02	-3.83E-06	2.53E+05
H2Si	273333	207.48	22.831	3.68E-02	-9.71E-06	1.81E+05
H3Si	204520	216.85	23.372	6.54E-02	-2.18E-05	-4.59E+04
H4Si	34309	204.65	14.356	1.10E-01	-3.98E-05	-6.91E+04
H6Si2	80300	272.66	54.020	1.36E-01	-4.48E-05	-1.03E+06
SiCH3F3	-1232001	314.20	43.360	1.86E-01	-8.26E-05	0.00E+00
SiC4H12	-286604	361.19	38.857	3.75E-01	-1.33E-04	0.00E+00
N	472687	153.30	20.894	-1.69E-04	6.01E-08	-5.58E+03
N3	436000	223.07	24.402	5.02E-02	-2.05E-05	-1.23E+05
NSi	378000	216.81	11.488	5.52E-02	-2.49E-05	4.02E+05
NSi2	384000	256.48	47.115	2.82E-02	-1.51E-05	-3.82E+05
CSi	734950	226.21	28.290	1.45E-02	-5.88E-06	-9.56E+04
C2Si	615048	236.73	34.860	4.24E-02	-1.96E-05	0.00E+00
CSi2	535600	242.30	37.170	4.08E-02	-1.95E-05	0.00E+00
Si	450000	167.98	21.041	-7.59E-04	5.84E-07	1.24E+05
Si2	583862	238.00	35.983	1.88E-03	2.90E-07	-2.50E+04
Si3	627869	279.18	46.874	3.47E-02	-2.12E-05	-3.90E+05
C	716680	158.10	20.975	-4.00E-04	2.01E-07	-3.36E+03
C2	830457	197.10	97.481	-1.64E-01	1.18E-04	-1.38E+06
C3	839958	237.61	32.216	2.91E-02	-1.07E-05	2.01E+05
CF	244072	213.03	23.163	2.24E-02	-1.01E-05	9.80E+04
CF2	-182004	240.83	19.473	7.57E-02	-4.47E-05	7.85E+04
CF3	-470282	265.08	21.251	1.20E-01	-7.07E-05	-8.77E+04
CF4	-933200	261.45	33.721	1.35E-01	-7.31E-05	-5.71E+05
C2F2	20900	244.10	36.010	8.33E-02	-4.00E-05	0.00E+00
C2F4	-658600	300.00	36.310	1.79E-01	1.02E-04	0.00E+00
C2F6	-1343900	332.19	47.874	2.72E-01	-1.67E-04	-6.68E+05
CH2	390421	194.90	27.632	1.58E-02	2.33E-07	1.25E+05
CH3	146300	193.96	25.844	4.25E-02	-9.52E-06	6.65E+04
CH4	-74600	186.37	2.235	9.69E-02	-2.60E-05	6.11E+05
C2H2	227400	200.93	43.333	3.19E-02	-6.58E-06	-7.34E+05
C2H4	52400	219.32	-1.510	1.59E-01	-6.69E-05	2.53E+05
C3H4_1	192129	244.04	10.206	1.91E-01	-9.05E-05	0.00E+00
C3H6	20418	266.67	5.297	2.21E-01	-8.35E-05	5.98E+04
C3H6_1	53304	237.55	-238.356	1.03E+00	-8.06E-04	5.32E+06
CHN	135140	201.83	25.730	3.88E-02	-1.45E-05	0.00E+00
CN	440287	202.64	23.312	1.36E-02	-3.67E-06	1.88E+05
C2N2	309100	242.20	52.476	3.47E-02	-9.85E-06	-4.32E+05
CH2F2	-450659	246.70	12.250	1.15E-02	-4.41E-05	0.00E+00
CH3F	-234300	222.80	37.500	0.00E+00	0.00E+00	0.00E+00

C2HF	125500	231.60	34.900	6.96E-02	-3.18E-05	0.00E+00
CHF	125500	223.40	25.900	3.16E-02	-9.47E-06	0.00E+00
CHF3	-697100	259.70	16.020	1.37E-01	-6.25E-05	0.00E+00

Table B. Thermodynamical properties, ΔH_{298}^{o}, S_{298}^{o} and C_p, of solid phases, included in calculations.

species	ΔH_{298}^{o}	S_{298}^{o}	C_p			
			A	B	C	D
C	0	5.69	-3.026	4.75E-02	-2.35E-05	-4.56E+04
αSiC	-71546	16.49	26.496	4.07E-02	-1.85E-05	-9.08E+05
βSiC	-73220	16.61	25.924	4.20E-02	-1.92E-05	-8.80E+05
WC	-40041	32.38	43.376	8.64E-03	-1.02E-06	-9.32E+05
W2C	-46024	81.59	89.747	1.09E-02	0.00E+00	-1.46E+06
W	-7646	130.40	-24.100	-1.94E-03	2.07E-07	4.45E+04
NH4F	-467560	71.97	12.967	1.75E-01	-1.09E-07	8.10E+02
WF4	-1237000	142.00	105.659	3.47E-02	-2.22E-10	9.48E+01
WF5	-1448000	165.00	125.362	4.91E-02	-6.45E-11	5.81E+01
WF6	-1747300	268.00	169.000	0.00E+00	0.00E+00	0.00E+00
Si3N4	-737639	107.11	70.417	9.87E-02	0.00E+00	0.00E+00

Table C. Temperature dependence of Gibbs free energy for solid phases.

species	ΔG(T), Jmol-1					
	A	B	C	D	E	F
W2N	-7646	130.40	-24.100	-1.94E-03	2.07E-07	4.45E+04
delta_WN	-66519	272.76	-45.645	-3.53E-03	0.00E+00	3.93E+05
Si	-8163	137.24	-22.832	-1.91E-03	-3.55E-09	1.77E+05
WSi2	-39030	135.66	-23.255	-1.92E-03	6.66E-08	1.33E+05
W5Si3	-27044	131.19	-23.624	-1.93E-03	1.28E-07	9.41E+04

Chapter 4

Ta-based barrier films on SiLK

4.1 Introduction

Interconnection signal delay, characterised by the resistance-capacitance constant-RC, can exceed the transistor gate delay significantly for circuits for the 0.18 μm technology node and beyond. In order to reduce the RC delay, first of all, the interconnects resistance is reduced by using Cu with a bulk resistivity of 1.7 μΩ·cm instead of Al with a resistivity of 2.7 μΩ·cm [1]. However, to prevent Cu diffusion Cu must be separated from the active area of devices by a diffusion barrier. Ta-based films, i.e. Ta [2], Ta_xN_{1-x} [2], [3], Ta_xSi_{1-x} [4], Ta_xC_{1-x} [5], have shown to be excellent diffusion barriers. A Cu/Ta-based barrier combination is characterised with a high thermal stability at back end processing temperatures, which can be as high as 400 ^oC. Secondly, RC delay can be reduced by making the interconnect capacitance in Si IC's smaller. In this case, cross-talk and power dissipation are also reduced. In order to reduce the interconnects capacitance the conventional dielectric, SiO_2 should be replaced by materials with a low dielectric constant k (low-k materials). SiLK™ is one of the possible candidates having a dielectric constant of 2.65 [6]. SiLK™ is an aromatic hydrocarbon polymer. Pores introduced into SiLK™ decrease the dielectric constant. The porous SiLK (with pores of about 10 nm diameter), pSiLK, has a dielectric constant of 2.1. The lower dielectric constant makes pSiLK the more advantageous low-k dielectric. On the other hand, as a material with pores it can exhibit integrity problems, for example due to poor adhesion.

The high back-end temperatures may lead to chemical reactions between a barrier and SiLK or pSiLK during the processing of the barrier/low-k dielectric stack with Cu. As a result a change in the resistivity of the barrier and even adhesion failure may occur. The thermal stability of a Ta-based barrier (Ta or Ta_xN_{1-x} or Ta_xSi_{1-x} or Ta_xC_{1-x})/SiLK or pSiLK combinations is the focus of our study in this chapter.

4.2 Experimental

4.2.1 Sample preparation for reactivity test

(100) Si wafers with 700 nm SiO_2 were used. SiLK or pSiLK layers were formed by spin coating on the top of the SiO_2 using an oligomeric solution, SiLK^{TM}. After curing at 400 ^{o}C the thickness of the SiLK or pSiLK layers was 400 nm. Barrier layers (Ta or Ta_xN_{1-x} or $Ta_{95}Si_5$ or $Ta_{90}C_{10}$) with a thickness of 20 or 25 nm were deposited by RF- sputtering. The pure Ta films were deposited in Ar. Tantalum nitrides and tantalum carbide films were sputtered in ($Ar+N_2$) and ($Ar+CH_4$) gas mixtures, respectively. For the Ta_xN_{1-x} films x varied between 0.94 and 0.84. The films of Ta containing silicon were deposited by co-sputtering from a Ta and a Si target. A 2-3 nm αSi film was sputtered on top of the barrier without breaking vacuum to prevent oxidation in air ambient. shows a schematic of the prepared stacks.

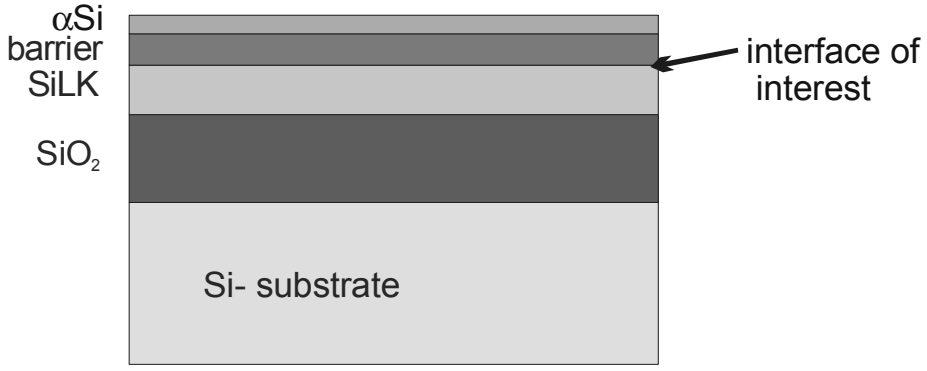

Figure 4-1. Schematic of the prepared stack.

4.2.2 Sample preparation for adhesion test

The test structure for adhesion test consists of two diced out pieces of the samples with a size of 60mm (length) x 10mm (width). The pieces were cut from as deposited wafers and wafers annealed in N_2 at 250 or 400 ^{o}C for 15 minutes. The pieces were glued with Epotek 353ND (1:10) together with films face to face. The glued stripes were cured at 130ºC for 1 hour. Finally, a notch was sawn on one side of the samples with a depth of ¾ of the wafer thickness to form a pre-crack. Figure 4-2 shows a principal scheme of the measurements and a schematic of the test structure.

4.2.3 Measurements

4.2.3.1 Four-point probe sheet resistance measurements

In order to study the reactivity of the low- k dielectrics with Ta-based barriers four-point probe in situ sheet resistance measurements were performed at elevated temperature. The measurements were carried out up to 400 ^{o}C under vacuum with a pressure lower than $4 \cdot 10^{-6}$ mbar. A temperature ramp of 3 degree/min for heating up and cooling down was used. The time step at constant temperature was 120 min. The resistivity of the Ta or Ta-based films was calculated by multiplying the sheet resistance and the film thickness.

4.2.3.2 Four-point bend adhesion test

The four point bend technique was used to quantify the adhesion of the different stacks. Samples were tested in a so-called universal mechanical test station. Figure 4-2 shows the principal 2-dimensional scheme of the measurement with a cross-section of the tested structure. A sample is placed on the lower two bars, represented by the triangles in a cross-section scheme. During the measurements, a constantly increasing force is applied to the top bars (see P/2 in Figure 4-2) of the sample in such a way that the loading points (P/2) are displaced with respect to the lower points as shown in Figure 4-2. The dependence of the increasing load P versus displacement is measured during the test. Figure 4-3 presents a load-displacement plot for a sample with a $Ta_{0.9}N_{0.1}$ film on SiLK. At the beginning of the test the displacement increases linearly (see part 1 of the plot in Figure 4-3). At some critical displacement the pre-crack notch collapses and the load drops instantaneously (see part 2 in Figure 4-3). Now a crack propagates under a constant load along the weakest interface. This shows up as the plateau in part 3 in Figure 4-3. When the crack reaches the position of two lower bars, the sample breaks and the load drops to zero (part 4 in Figure 4-3).

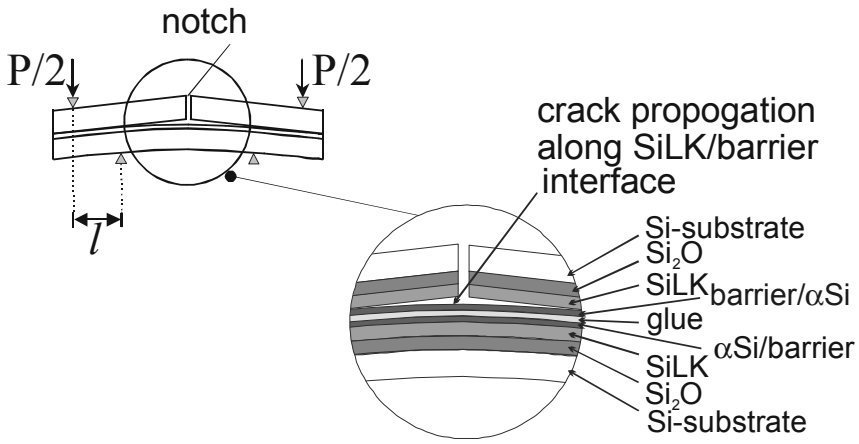

Figure 4-2. Principal 2d scheme for the four-point bend adhesion test.

The constant load P at which the adhesion failure occurs is used to calculate the adhesion energy for the failed interface. Adhesion energy G (J/m^2) is calculated with following equation 4-1 [7]:

$$G = \frac{21 \cdot \left(1 - \nu^2\right) \cdot P^2 \cdot l^2}{16 \cdot E \cdot b^2 \cdot h^3}, \qquad \textit{Equation 4-1}$$

where ν is the Poisson's ratio;
P is the load (N);
l is the horizontal distance between the top bars on the top and the lower bars (m);
E is the elastic modulus of the Si substrate (N/m^2);
b is the sample width (m);
h is half the height of the sample (m).

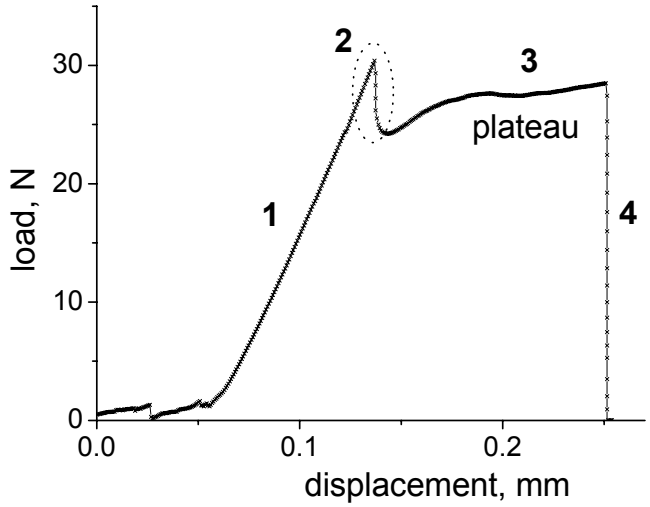

Figure 4-3. The load versus displacement for as deposited stack of glue/αSi/$Ta_{0.9}N_{0.1}$/SiLK/SiO_2 films on Si substrate.

4.2.3.3 XPS analysis

For the reactivity test, compositional analysis of the films was done with profiling XPS (X-Ray Photoelectron Spectroscopy) with a 4 kV Ar^+ ion beam with an area 4x4 mm^2. Samples before and after heating were analysed.

For the four-point bend adhesion tests, surface scan XPS was applied after the adhesion test to determine the failed interface or where a fracture took place. The information depth of surface scan XPS is about 6 nm. Standard sensitivity factors were used to calculate concentrations.

4.3 Results and discussion

4.3.1 Four-point probe sheet resistance measurements

The sheet resistance measurements were performed for 20 or 25 nm films of Ta, $Ta_{0.94}N_{0.06}$, $Ta_{0.92}N_{0.08}$, $Ta_{0.9}N_{0.1}$, $Ta_{0.84}N_{0.16}$, $Ta_{0.95}Si_{0.05}$ and $Ta_{0.9}C_{0.1}$ at elevated temperatures. It should be noted that the big difference in the thermal expansion coefficient of the barrier and the SiLK ($6.5 \cdot 10^{-6}$ K^{-1} (Ta) and $66 \cdot 10^{-6}$ K^{-1}, respectively) and a difference in hardness sometimes caused some instabilities in the temperature- biased measurements. XPS-

depth profiles were made for as deposited samples and samples after sheet resistance measurements up to 400 °C.

- The αSi/Ta/SiLK/SiO_2 and the αSi/Ta/pSiLK/SiO_2 stack

The resistivity of the as deposited Ta films on SiLK and pSiLK was in the range of 30-100 μΩ·cm. The resistivity for α-Ta phase and for β-Ta phase has been reported to be 25 μΩ·cm and 196 μΩ·cm, respectively [8]. Thus, as deposited layers consisted mainly of the low resistivity α-Ta phase.

Figure 4-4 shows a plot of the normalized resistance of the Ta/SiLK combination versus temperature with a step at constant temperature of 400 °C for 120 min and 5 min (see curve 1 and 2, respectively). The slope of the normalised resistance-temperature dependence represents the TCR (Temperature Coefficient of Resistance). For curve 1 at heating below 160 °C the normalised resistance increases linear with temperature. At about 160 °C normalised resistance begins to deviate from the linear dependence (see curve 1, part a in Figure 4-4). During heating and at the constant temperature step of 400 °C the resistance increases (see curve 1, part a and b in Figure 4-4). This increase is mainly due to diffusion of oxygen into Ta-film as determined from XPS depth profile.

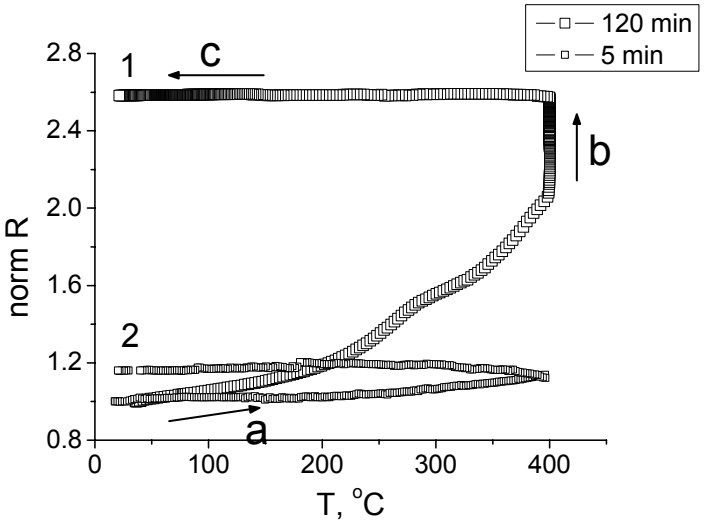

Figure 4-4. Normalised resistance of the αSi/Ta(20 nm)/SiLK/SiO_2/Si stack versus temperature: 1. the first heat treatment for 120 min; 2. the second heat treatment for 5 minutes. Arrows indicate: a) heating up; b) 120 min step at constant temperature; c) cooling down.

Figure 4-5 shows the XPS concentration depth profile for an as deposited sample with the αSi(3nm)/Ta/SiLK combination. The top of the protective film of amorphous Si on the stack was oxidized. At the interface with the underlying Ta film no oxygen signal was measured. At the lower interface of Ta/SiLK some oxygen was present (see filled circles in Figure 4-5). XPS detected no bond formation for stoichiometric tantalum oxide compounds, for example a Ta_2O_5 or Ta_2O_3 insulating layer. The oxygen was incorporated in the Ta film possibly with the formation of the β-Ta phase. The solubility of oxygen in β-Ta is up to 19 at% [8]. Also tantalum carbide was present at the Ta/SiLK interface (see filled squares in Figure 4-5). Obviously it was formed during the sputter deposition process of the Ta film.

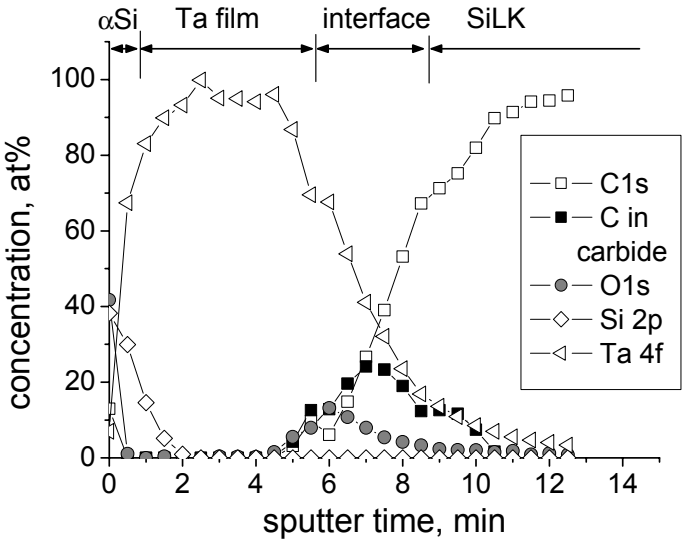

Figure 4-5. XPS depth sputter profile for the as deposited αSi/Ta/SiLK stack.

Figure 4-6 shows the XPS concentration depth profile for the sample with αSi(3nm)/Ta/SiLK combination after heat treatment at 400 ^{o}C for 120 minutes in vacuum. The amount of Ta-C bonds hardly changed compared to the as deposited sample (see filled squares). Therefore no further reaction between the barrier and hydrocarbons from SiLK occurs. However, after heating the O-concentration at the Ta/SiLK interface increased from 13 up to 17 at% (see filled circles). At the same time a homogeneous O distribution at the level of 8 at% was found throughout the film. The O concentration lowers at the αSi/Ta interface. From this profile it is concluded that the source of oxygen is the SiLK-underlayer.

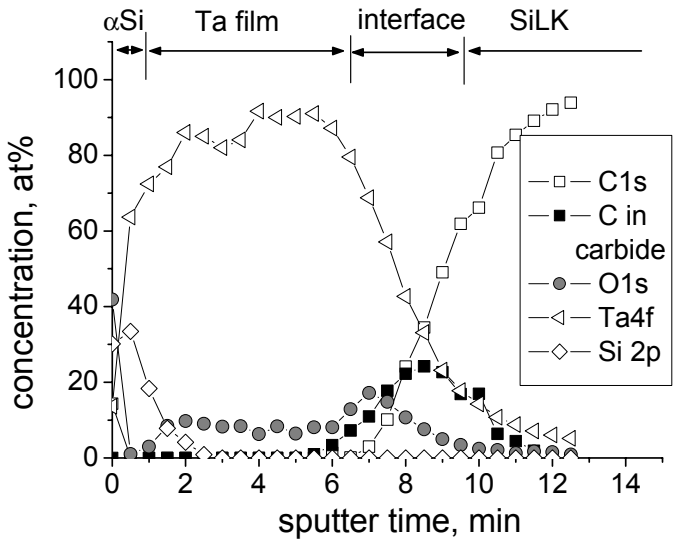

Figure 4-6. XPS depth sputter profile for the αSi/Ta/SiLK stack annealed at 400°C for 120 minutes.

In order to check the stability of the O-containing Ta/SiLK stack heated once for 120 min at 400 °C, this sample was heated additionally for 5 min at 400°C. Figure 4-4 shows how the normalised resistance changes with temperature during the first heat treatment and the second heating treatment (see curve 1 and curve 2). The increase of resistance was by a factor of 2.58 after the first heating and by a factor of 1.16 after the second. This confirms that the limit of O in Ta was not reached after the 120 min thermal treatment at 400 °C and that O-diffusion will continue.

During the cooling step the slope of the (resistance-temperature) plot differs from the slope at the beginning of measurements (see curve 1, part c and a in Figure 4-4). This change is attributed to a TCR (temperature coefficient of resistance) change, which indicates a modification of the tested material, i.e. a change of composition of Ta film. The increase of resistance at the end of the test by a factor of 2.58 is attributed to oxygen diffusion from the SiLK into the Ta-film.

Figure 4-7 shows the normalised resistance of the Ta/pSiLK combination versus temperature with a step at constant temperature at 400, 370 and 280 °C (see curve 1, 2 and 3, respectively). Unlike Ta/SiLK, the

temperature dependence of resistance for the Ta/pSiLK demonstrated a deviation from the linear behavior at lower temperature of about 100 °C. The difference in the temperature for this deviation can be explained by the liberation of contaminants from the pores in pSiLK, starting at a lower temperature than from the SiLK film. At the constant temperature step at 400 °C the resistance increases (see part b in curve 1, 2 and 3 in Figure 4-7). This increase is due to oxygen diffusion into the Ta-film similar to the case of the Ta film with the SiLK underlayer.

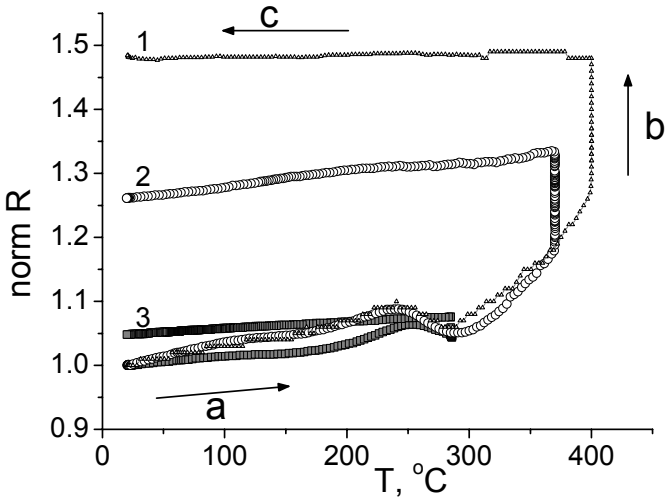

Figure 4-7. Normalised resistance of the aSi/Ta/pSiLK/SiO_2 stack on Si versus temperature. Arrows indicate: a) heating up; b) 120 min step at constant temperature; c) cooling down.

Figure 4-8 and Figure 4-9 show XPS depth profiles for the as deposited and the 400 °C heated stack of the Ta/pSiLK combination. Unlike the Ta/SiLK stack the as-deposited barrier film on pSiLK contains oxygen at a concentration of 3 at%. At the same time at the barrier/dielectric interface the peaks of O and C are similar to the ones observed in the stack with the SiLK underlayer. One explanation of the O-signal detected within the film can be a higher roughness of the barrier film on pSiLK, which is increasing during XPS sputtering. As a result, the O-signal can have a larger tail in the barrier film itself. On the other hand, the oxygen can be incorporated into the barrier film during the sputter deposition process, being released from the pores of the pSiLK, which can contain contaminants. After the heat

treatment at 400 °C the O-concentration in the barrier on pSiLK was equal to the value in these films on SiLK, about 8 at % O.

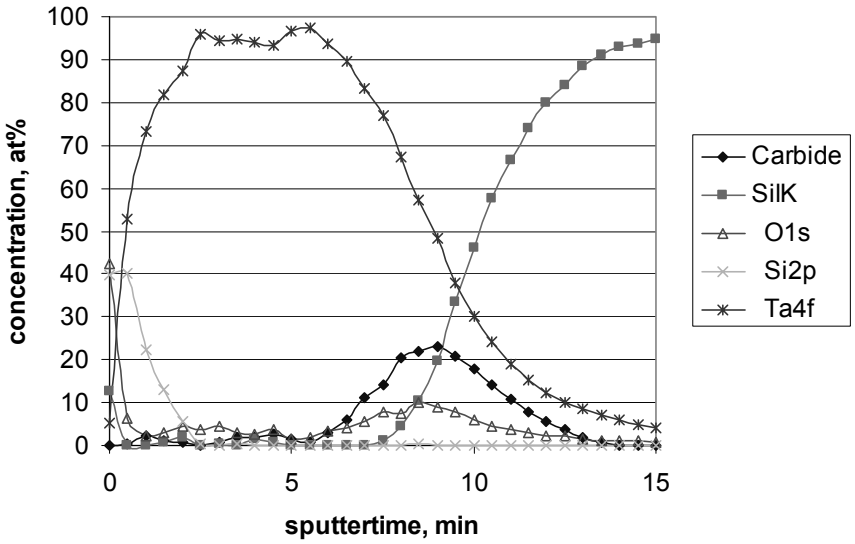

Figure 4-8. XPS depth sputter profile for the as deposited αSi/Ta/pSiLK stack.

The slope of the measured curve (TCR) during cooling differs from the slope during heating. This indicates that changes of material properties have occurred. Measurements at lower temperature, 370 and 280 °C, resulted in similar effects (see curve 2, 3 in Figure 4-7) with a change of TCR. The lower the temperature the smaller the final increase of the resistance. The measurements up to 280 °C show an increase of normalised resistance by a factor of only 1.05 and virtually no change in TCR. Thus, the Ta film/pSiLK combination is stable up to at least 280 °C.

The increase of the resistance after testing is larger for the Ta- film on SiLK layer than for the Ta- film on pSiLK for different test temperatures. For instance, after 400 °C this increase was by a factor of 2.58 for the Ta on SiLK and 1.48 for the Ta on pSiLK (see Figure 4-4 and Figure 4-7). Thus, the reactivity of the Ta barrier layer with pSiLK, referred to as the increase in normalized resistance, is lower than the reactivity with SiLK in the range of measured temperatures. An explanation is that the as-deposited Ta films on pSiLK already contain oxygen and, possibly, other contaminants that makes the oxygen diffusion slower and the related resistance increase lower.

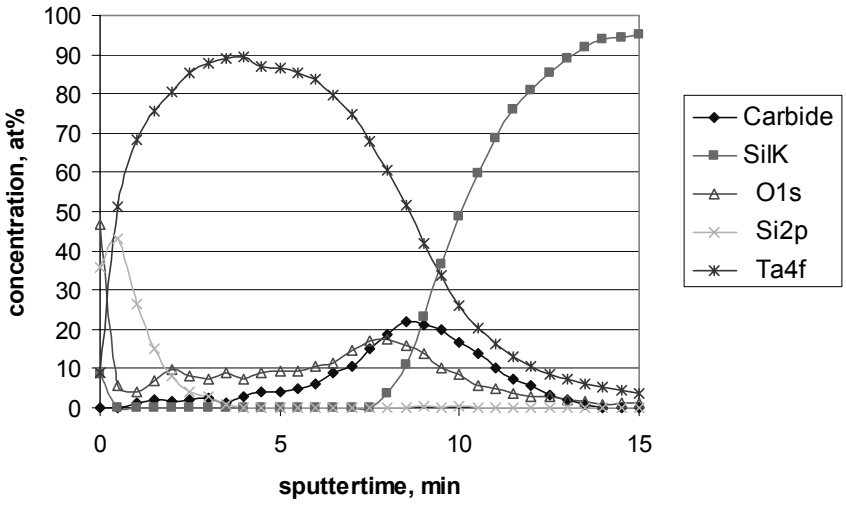

Figure 4-9. XPS depth sputter profile for the αSi/Ta/pSiLK stack annealed at 400°C for 120minutes.

The TCR of Ta film on SiLK and pSiLK changes after the heat treatments. This change is attributed to oxygen diffusion in the Ta film out from the underlying low-k dielectric.

- The $\alpha Si/Ta_{0.95}Si_{0.05}/SiLK/SiO_2$ stack

Figure 4-10 shows the normalised resistance of a stack with $Ta_{0.95}Si_{0.05}$ on SiLK during the heat treatment with maximum temperature of 400 °C. The resistance decreases linearly with temperature up to 200 °C. The $Ta_{0.95}Si_{0.05}$ shows a negative TCR unlike Ta. There is no general universal explanation why some materials show a negative TCR [9]. But it is known that the resistance of films with a negative TCR will not change linear with

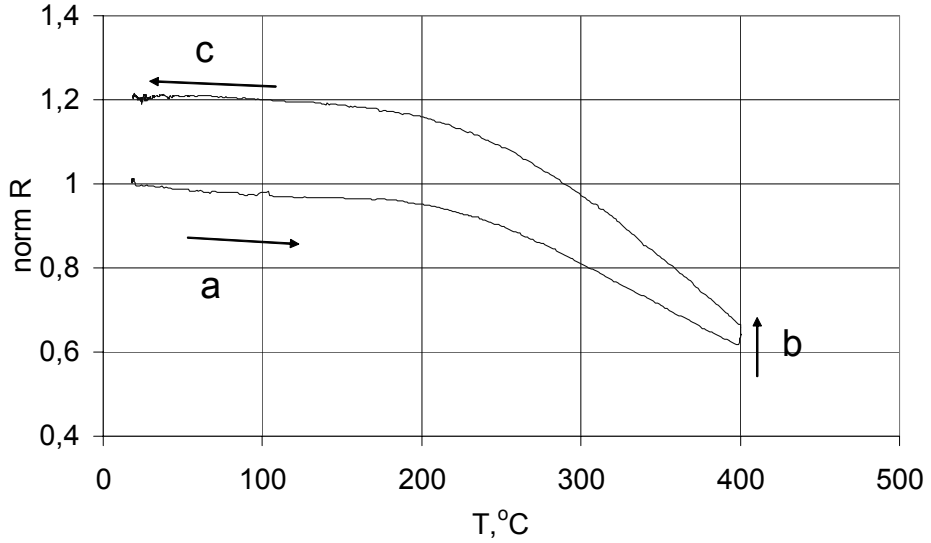

Figure 4-10. Normalised resistance of αSi/$Ta_{0.95}Si_{0.05}$/SiLK/SiO_2/Si stack versus temperature for 400 °C heat treatment for 120 min. Arrows indicate: a) heating up; b) 120 min step at constant temperature; c) cooling down.

temperature [10]. This is also clearly observed in Figure 4-10. After the test the TCR becomes less negative in the lower temperature range. At the same time an increase of resistance is observed by a factor of 1.19. Again, these changes are ascribed to oxygen diffused from the SiLK into the barrier film.

Figure 4-11 presents O- and C concentration (circles and diamonds) determined with XPS for the as deposited and the heat-treated at 400 °C samples (empty and filled shapes). XPS depth profile shows no changes in C concentration at the barrier/SiLK interface after the heat treatment. In opposite, O peak at this interface and in the film itself increases. The concentration of oxygen determined in the film was about 8−9% like in the Ta films. Obviously, the Si in the $Ta_{0.95}Si_{0.05}$ film does not restrict O-content, which can be limited either by the maximum solubility of O in the material or by a slower diffusion.

The surface of the films stack was changed to "orange skin" look, indicating worsening of adhesion.

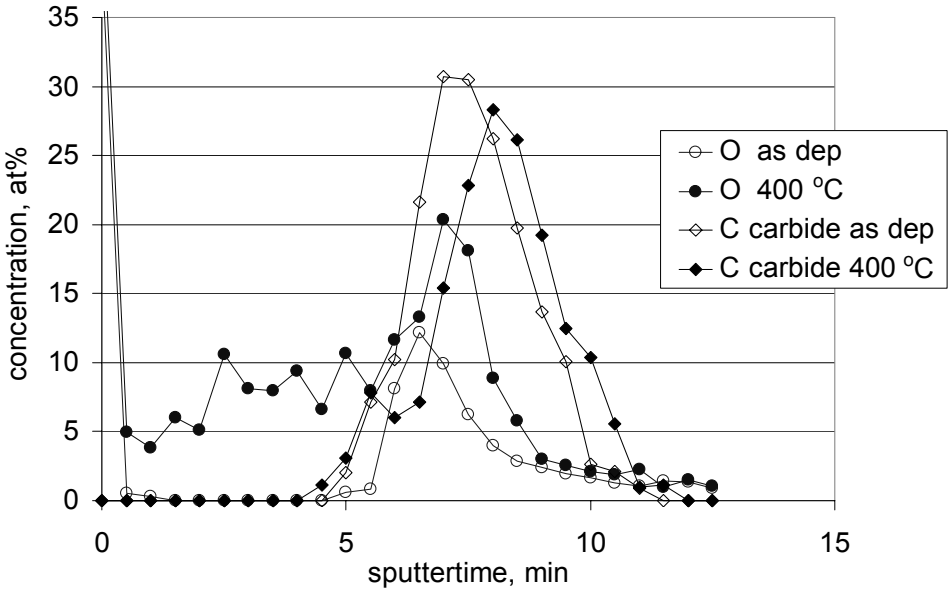

Figure 4-11. XPS depth sputter profile of O- and C concentration in the as deposited αSi/$Ta_{0.95}Si_{0.05}$/SiLK stack and the heat treated samples at 400 °C for 120 min.

- The αSi/$Ta_{0.9}C_{0.1}$/SiLK/SiO_2 stack

Figure 4-12 presents a surface image of the αSi/$Ta_{0.9}C_{0.1}$/SiLK/SiO_2 stack after 400 °C heating. The $Ta_{0.9}C_{0.1}$ has got a vivid bulging on the SiLK. This starts at temperatures as low as 250 °C and continues at higher temperatures. This bulging occurs because of the large difference in mechanical properties of tantalum carbide and SiLK. Among our tested barriers tantalum carbide has the smallest thermal expansion coefficient and the largest elastic modulus, i.e. 6.29 10^{-6} K^{-1} and $28.5 \cdot 10^{10}$ N/m^2, respectively. For SiLK this is $66 \cdot 10^{-6}$ K^{-1} and $7.17 \cdot 10^{10}$ N/m^2, respectively. Thus, the tantalum carbide/SiLK combination is the least stable under thermal stress conditions. During heat treatment the density of the bulging stripes grows, leading to instability of the four-point probe sheet resistance measurements.

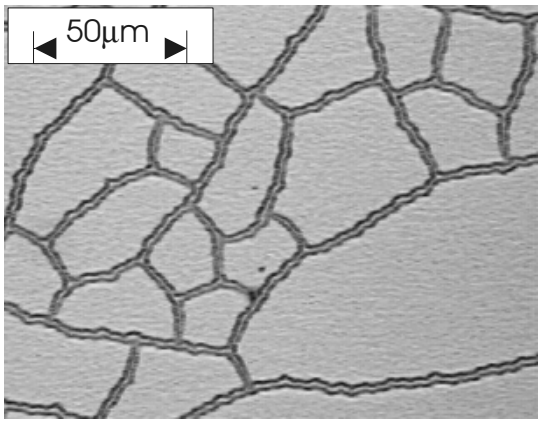

Figure 4-12. Surface image of the αSi/$Ta_{90}C_{10}$/SiLK/SiO_2/Si stack heat treated at 400 °C for 120 minutes.

Figure 4-13 shows the normalised resistance versus temperature plot for the $Ta_{0.9}C_{0.1}$/SiLK at different temperatures. The course is similar to the measurements for the Ta-film on pSiLK at 400 °C (see curve 1 in Figure 4-13 and in Figure 4-7). This demonstrates the same nature of the process during heating. Also in this case the increase of resistance at 400 °C is owed to oxygen diffusion in the barrier film.

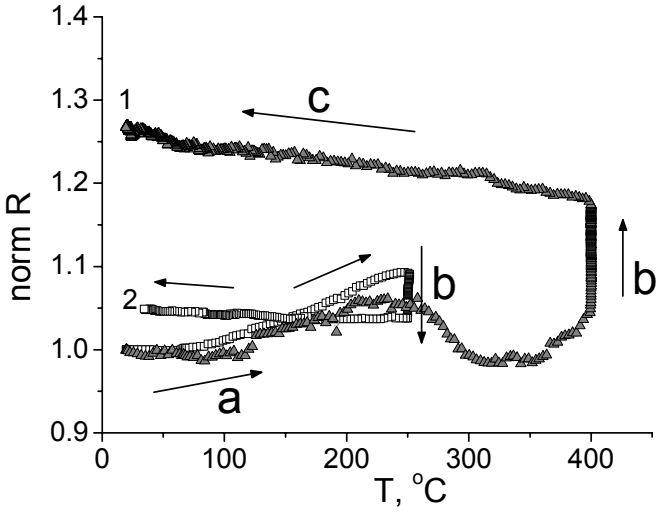

Figure 4-13. Normalised resistance versus temperature for the αSi/$Ta_{90}C_{10}$/SiLK/SiO_2/Si stack. Arrows indicate: a) heating up step; b) 120 min step at constant temperature; c) cooling down.

Figure 4-14 shows XPS depth sputter profile for O- and C (in carbide) concentration (circles and diamonds) in the $\alpha Si/Ta_{0.9}C_{0.1}/SiLK$ for the as deposited and the annealed stack (filled shapes). No changes are observed in O- and C concentrations at the barrier/SiLK interface after heating. In the film itself the oxygen concentration increase from zero up to about 9 at%. This concentration is constant throughout the film, like in the silicon-containing barrier. Also C in the $Ta_{0.9}C_{0.1}$ film does not restrict O-content in the heat treated films. An increase of normalised resistance related to oxygen in the $Ta_{0.9}C_{0.1}$ film is by a factor of 1.26. In addition, after the heating TCR of the barrier changes. This confirms changes of material properties of the film.

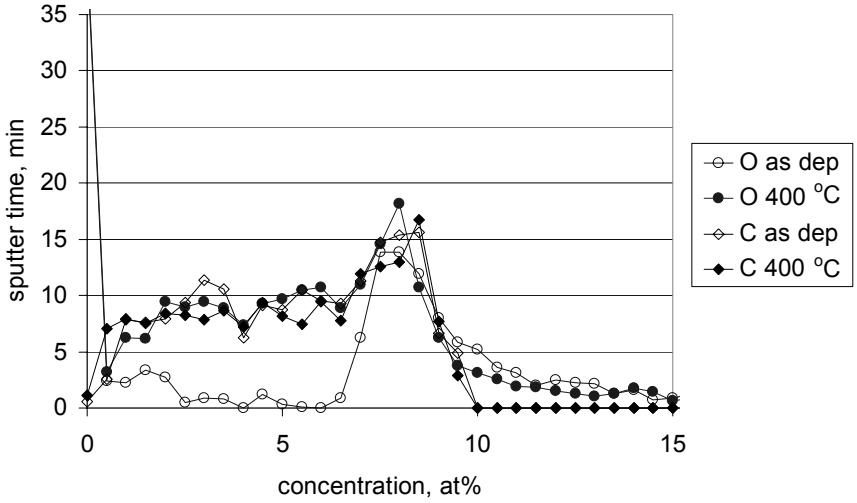

Figure 4-14. XPS depth sputter profile for O- and C concentration in the $\alpha Si/Ta_{0.9}C_{0.1}/SiLK$ stack as deposited and the heat treated stack at 400 °C for 120 min.

During heat treatment at a constant temperature of 250 °C the resistivity of the stack decreases (see arrow b for curve 2 in Figure 4-14). This can be due to a larger contribution of the resistance decrease by structural ordering of barrier and/or gas release from barrier than the resistance increase by oxygen diffusion in the barrier. The resistance after the heat treatment was increased by a factor of 1.05. This is not significant enough to draw conclusions about substantial O diffusion at 250 °C.

- The $\alpha Si/Ta_xN_{1-x}/SiLK/SiO_2$ and the $\alpha Si/Ta_xN_{1-x}/pSiLKSiO_2$ stack

The resistance of stacks with nitrogen-containing tantalum with a verified

nitrogen content, 6, 8, 10 and 16 at%, was also measured. The thickness of the film with 10 at% N was 25 nm. The thickness of the films with the other nitrogen concentration was 20 nm. Unfortunately, some measurement cycles suffered from loosing good electrical contact at elevated temperatures due to the large difference of the thermal expansion coefficients and mechanical instabilities in the barrier layer/low-k dielectric combinations. This holds especially for the films on pSiLK.

Figure 4-15 shows the normalised resistance versus temperature for the $\alpha Si/Ta_{0.94}N_{0.06}/SiLK/SiO_2/Si$ stack. The constant temperature step was at 400, 340, 280 and 240 ^oC (see curve 1, 2, 3 and 4, respectively).

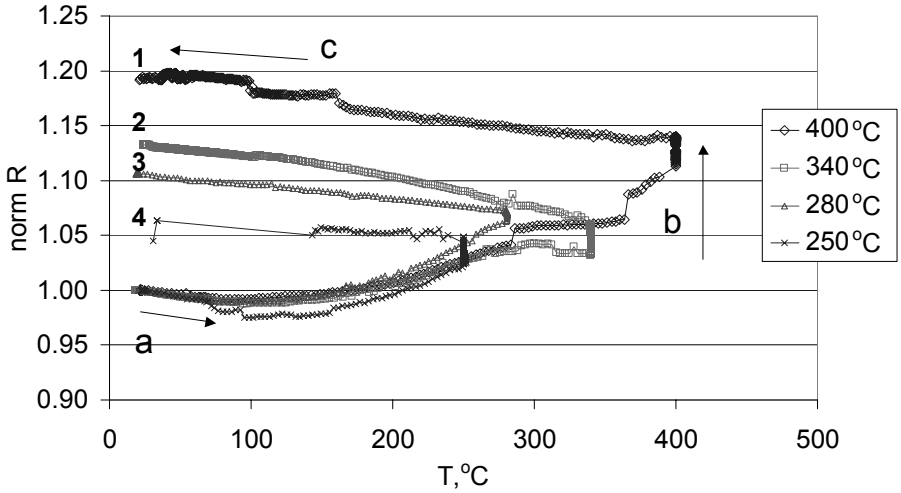

Figure 4-15. Normalised resistance versus temperature for the $aSi/Ta_{0.94}N_{0.06}/SiLK/SiO_2/Si$ stack. Arrows indicate: a) heating up step; b) 120 min step at constant temperature; c) cooling down.

$Ta_{0.94}N_{0.06}$ shows a negative TCR as the other nitrides in this study. Changes of resistance with temperature can be ascribed to changes in the film and/or the change in TCR as a function of temperature (see also section on $Ta_{0.95}Si_{0.05}$, p. 60). No accurate value of the TCR can be obtained from the measurements.

As a result of the heat treatment at 400 °C the normalised resistance increases by a factor of 1.19 (curve 1 in Figure 4-15). The related XPS depth profile in Figure 4-16 (filled circles) shows an O concentration of about 5 at% throughout the film. This is lower than in the films discussed earlier. Unlike Si and C, N in the Ta based films restricts O-incorporation either due to a lower limit of O-solubility or due to a slower diffusion. No changes of the C peak at the barrier/SiLK interface is observed after the heat treatment (empty and filled diamonds), while O peak increases (empty and filled circles).

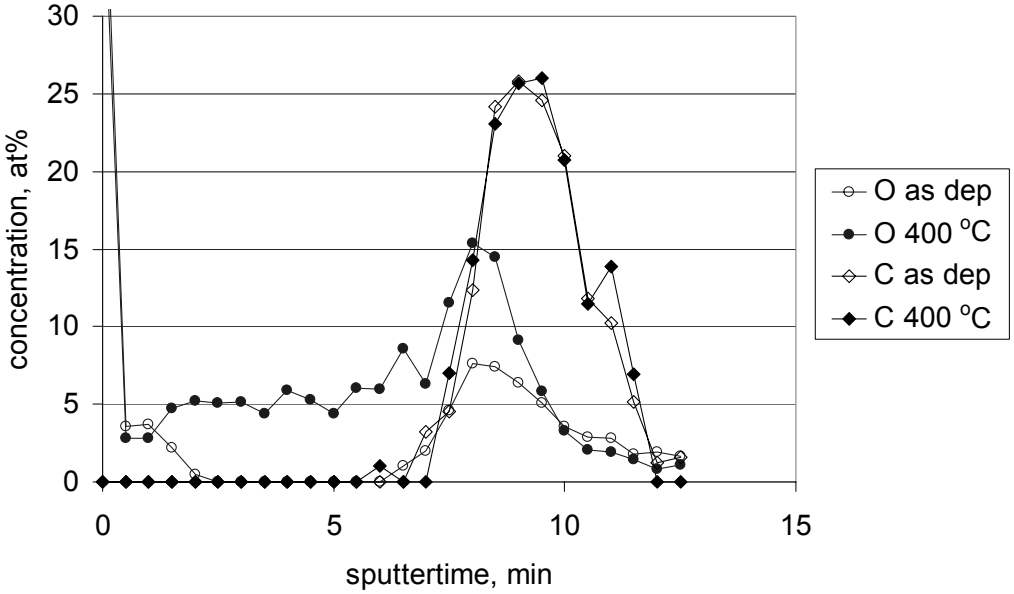

Figure 4-16. XPS depth sputter profile for O- and C concentration in the αSi/$Ta_{0.94}N_{0.06}$/SiLK stack as deposited and the heat treated stack at 400 °C for 120 min.

The gradual increase of the resistance after the heat treatments treatment (see curve 4, 3, 2 and 1 in Figure 4-15) suggests that oxygen diffusion starts at temperatures above 280 °C.

The (resistance-temperature) dependence for the films with a nitrogen concentration of 8 at% and 10 at% N are similar to the presented curves in Figure 4-15. After the 400 °C heat treatment the increase of resistance was by a factor of 1.13 and 1.04, respectively. Those films contain also about 5at % O. So far, Ta films containing 6-10 at% N show the least resistance

increase and the least amount of oxygen. Films with 16 at% N showed some dissimilarity and will be discussed below.

Figure 4-17 shows the dependence of the normalised resistance on temperature for the nitrogen rich $Ta_{0.84}N_{0.16}$/SiLK stack with a constant temperature step at 400, 340 and 280 ^{o}C (curve 1, 2 and 3). The slope of the line during cooling is the same as the slope during heating up to 100 ^{o}C. This means that the TCR has not changed significantly. The resistance, however, has increased after heating by a factor of 1.4. XPS depth profile clarifies the changes, which occurred in the $Ta_{0.84}N_{0.16}$/SiLK stack.

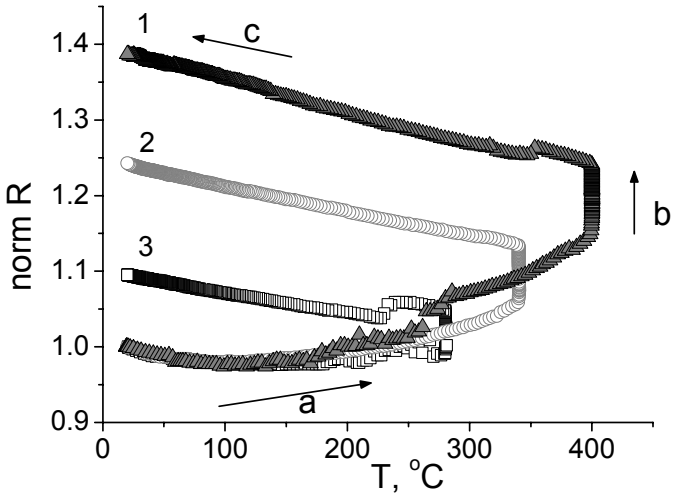

Figure 4-17. Normalised resistance versus temperature for the aSi/$Ta_{0.84}N_{0.16}$/SiLK/SiO_2/Si stack. Arrows indicate: a) heating up step; b) 120 min step at constant temperature; c) cooling down.

Figure 4-18 shows XPS depth profile for O- and C (in carbide) concentration for the as deposited αSi/$Ta_{0.84}N_{0.16}$/SiLK stack and the annealed stack. There is a high C concentration (~37 at%) at the barrier/ SiLK interface and oxygen present within $Ta_{0.84}N_{0.16}$ film (~3 at%) in the as deposited sample. No change of the C peak is observed after the heat treatment. Also in this case the hydro-carbon bonds do not react with the barrier. Also no change of oxygen content is observed within the barrier film itself (circles). On the other hand, the formation of an oxygen-enriched layer at the SiLK interface took place. Thus, this nitrogen rich $Ta_{0.84}N_{0.16}$ prevents oxygen diffusion in the film. As a result, no change in

material properties affecting TCR occurs. This is shown in the four-point probe sheet resistance measurements. However, this barrier film has a very poor adhesion after heat treatment. This is due the formation of the oxygen rich layer at the barrier/SiLK interface. As a result, the $Ta_{0.84}N_{0.16}$ layers are bulging on the organic dielectric and they fail the criterion of good adhesion to SiLK. There were no cracks in the film, but only bulging or so-called "orange skin" is observed. This is a typical failure for films under compressed stress.

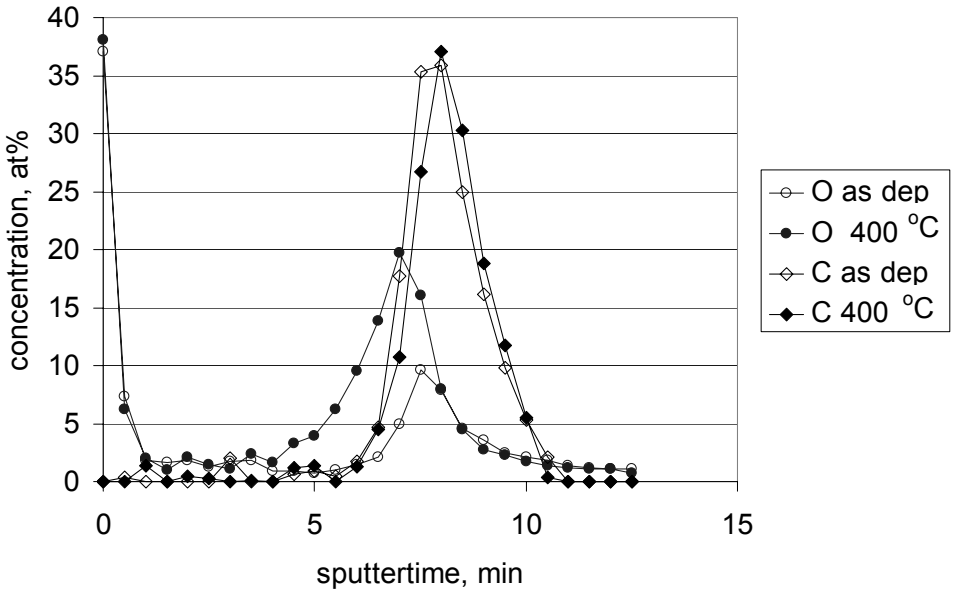

Figure 4-18. XPS depth sputter profile for O- and C concentration for the αSi/$Ta_{0.84}N_{0.16}$/SiLK stack as deposited and the heat treated stack at 400 °C for 120 min.

In order to obtain an overview of the O concentrations in the films the XPS depth profiles were normalised for thickness. Here the film thickness is made proportional to the sputter time, at which the maximum O-concentration at barrier/SiLK interface is observed. Figure 4-19 shows the O-concentration in the nitrogen containing Ta film with 6, 8 and 16 at% N. After heat treatment the O-concentration has a constant level of 5at% throughout the $Ta_{0.94}N_{0.06}$ film. In the case of the $Ta_{0.92}N_{0.08}$ film the concentration of oxygen decreases strongly towards the films surface. No change of oxygen profile was detected in the $Ta_{0.84}N_{0.16}$ film (see filled shapes). Obviously nitrogen containing tantalum films are capable to restrict O-incorporation. The film with the highest nitrogen content, i. e.

$Ta_{0.84}N_{0.16}$, demonstrated the best properties limiting oxygen content. However, in this case, oxygen from the SiLK underlayer was piling up at the lower interface and the $Ta_{0.84}N_{0.16}$ layer was partly delaminated.

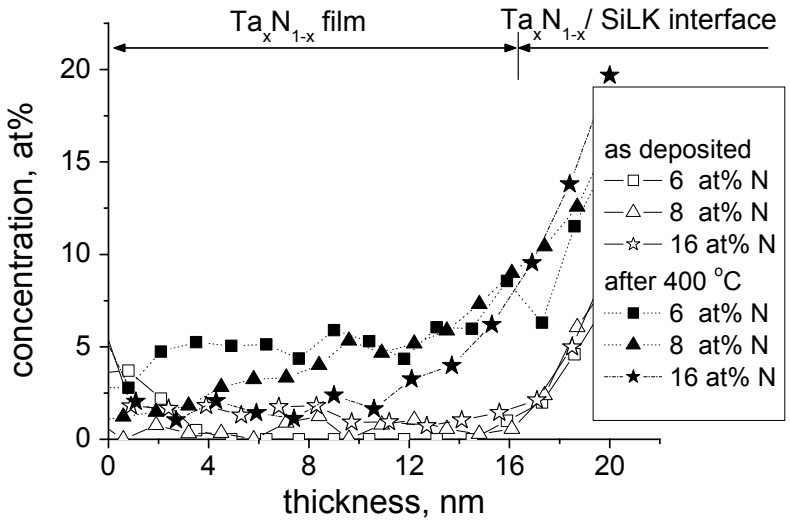

Figure 4-19. Depth profile of O-concentration for the αSi/$Ta_{1-x}N_x$/SiLK stack as deposited and the heat treated stack at 400 °C for 120 minutes with x=0.06; 0.08 and 0.16

Nitrogen containing Ta films on pSiLK showed a consistently smaller increase of resistance compared to the same films on SiLK. This is similar to the case of the Ta/pSiLK combination (see p. 57). The depth profiles of O-concentration are presented in Figure 4-20 for the $Ta_{0.92}N_{0.08}$/pSiLK and the $Ta_{0.84}N_{0.16}$/pSiLK stack. It is shown that the as deposited films include some oxygen (~3-5 at%). Like in the Ta/pSiLK combination, this can be due to an artifact of XPS for rough surfaces or O coming out of pSiLK during the deposition process of the barrier films. After heat treatment the O-concentration at the barrier/pSiLK interface increases. In the films themselves no substantial increase of oxygen concentration occurs. After the test the films surface had an "orange skin" appearance.

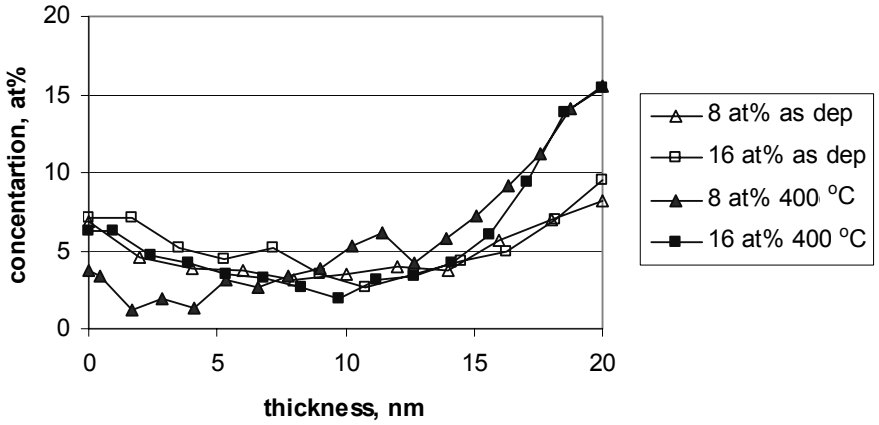

Figure 4-20. Depth profile of O-concentration for the αSi/$Ta_{1-x}N_x$/pSiLK stack as deposited and heat treated at 400 °C for 120 minutes with x= 0.08 and 0.16

Summary for sheet resistance measurements

Figure 4-21 presents a summary of the sheet resistance of the films before and after heat treatment at 400 °C and the concentration of oxygen in the films. The largest change of resistance, i.e. from 35 to 90 Ω/sq, and oxygen incorporation occurs in pure Ta films. The related oxygen concentration is about 8 at%. The increase of resistance for the $Ta_{0.95}Si_{0.05}$ and $Ta_{0.90}C_{0.10}$ films is substantially smaller, e.g. from 85 up to 107 Ω/sq for the $Ta_{0.90}C_{0.10}$. In this case, the concentration of oxygen is also about 8-9 at%. Obviously the incorporated Si or C does not restrict the oxygen incorporation in the barrier. The Ta film with 6 at% N shows a smaller increase of the resistance than the pure Ta film. After heat treatment the concentration of oxygen in the film is about 5 at%. Thus the oxygen incorporation was restricted either by a lower amount of O allowed in the material or by a slower O diffusion. The least changes of resistance and O-concentrations of 5 at% are observed in the Ta films with 8 and 10 at% N. Films containing 16 at% N showed excellent blocking properties against O diffusion, but failed adhesion requirements for diffusion barriers. Therefore Ta-films containing up to 10 at% nitrogen are the most suitable regarding the combination of a small resistance change at elevated temperatures, blocking properties against oxygen diffusion and a satisfactory adhesion with SiLK.

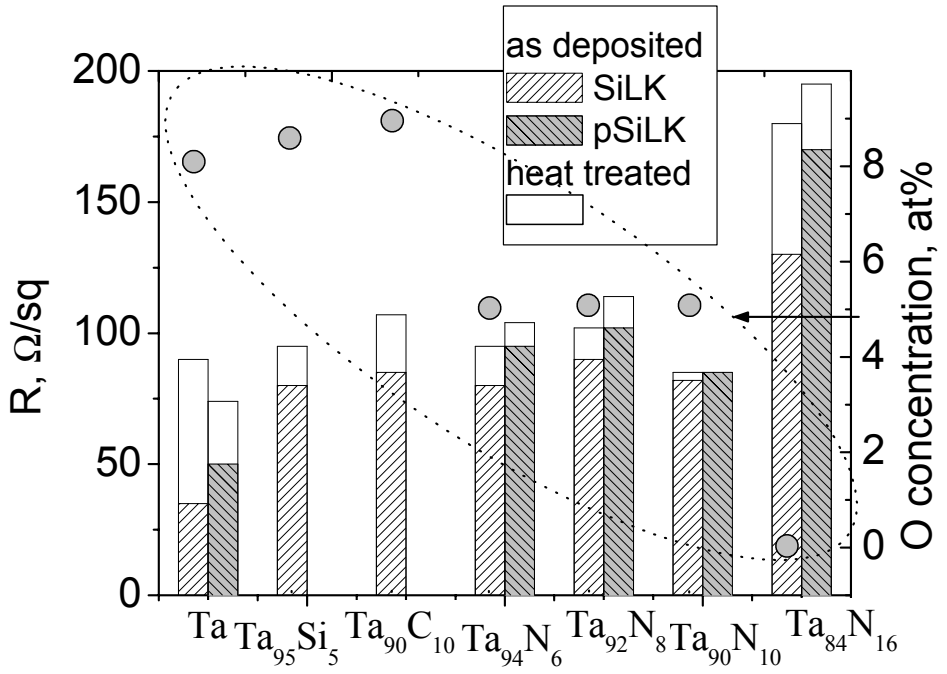

Figure 4-21. Sheet resistance of the samples as deposited and heat heated at 400 °C for 120 min and the oxygen concentration in Ta-based films with XPS. The films thickness is 20 nm, except for $Ta_{90}N_{10}$ (25 nm).

For the Ta based films on pSiLK the increase of the resistance is consistently smaller after heat treatment. This is probably due to impurities incorporated in the barrier film or at the pSiLK interface during the deposition of the barrier layer. These impurities can retard or block the O incorporation in the films.

The combination of the resistance changes and the adhesion aspects has to be considered to characterize the ability of the barrier/SiLK combination to withstand elevated temperatures (see 4.3.3 Adhesion test), i.e. its suitability for integration in back- end processing.

4.3.2 Resistivity calculations

From the resistance measurements and the measured oxygen concentration in the films from XPS depth profiles it is possible to calculate the dependence of the film resistivity on oxygen concentration in the film. For our calculations it was assumed that diffusion occurred through the inherent Ta_xC_{1-x} and Ta_xO_{1-x} layers present at the barrier/SiLK interface immediately after the barrier deposition. In our case the measured

resistance is the resistance of several conducting layers in parallel: the barrier/SiLK interfacial layer and the overlying barrier consisting of number of slabs, *i*, with incorporated oxygen from the SiLK, $C_{iOxygen}^{average}$. The oxygen distribution in the barrier was extracted from the XPS depth profiles. The Ta_xC_{1-x} film at the SiLK interface is excluded from calculations because of the unknown thickness (information depth of XPS was about 6 nm) and composition. Moreover, the contribution of this interfacial layer to the total resistance is probably negligible. The concentration coefficient of resistivity for oxygen *K* (μΩ·cm/at% O) was calculated using the depth distribution of oxygen, the sheet resistance before heat treatment, R_{ini}, and after heat treatment, *R,* following equation 4-2:

$$\begin{cases} \dfrac{1}{R_{ini}} = \dfrac{th_0}{\rho^0_{barrier}} + \sum_i \dfrac{th_i}{\rho^0_{barrier} + K * C^{average}_{i\,Oxygen}} \\ \dfrac{1}{R} = \sum_i \dfrac{th_i}{\rho^0_{barrier} + K * C^{average}_{i\,Oxygen}} \end{cases}$$

Equation 4-2

where th_o the thickness of barrier without incorporated oxygen;
th_i the thickness of the barrier slab *i* with the average oxygen concentration $C_{iOxygen}^{average}$ at%, extracted from the XPS depth profiles;
$\rho^o_{barrier}$ the resistivity of barrier film without oxygen.

Table 4-1 shows the results of the calculations. The calculated concentration coefficient of resistivity for oxygen in pure Ta-films is about 6.7 μΩ·cm/at% (see № 1, 2 in Table 4-1). A value of 5-6 μΩ·cm/at% is reported in literature [11]. *K* calculated for the carbon- containing Ta film is in the same range (see № 3 in Table 4-1). The oxygen in Ta films containing nitrogen and silicon gives a significant smaller concentration coefficient of about 2.65 in films with 8-10 at% nitrogen and 2.3 μΩ·cm/at% in the films with 5at% Si (see № 4, 5, 6, 7 in Table 4-1). The *K* values for the films on pSiLK are consistently higher (see № 8, 9, 10, 11 in Table 4-1). It should be noted, however, that these calculations are based on oxygen concentrations derived from the XPS depth profiles (Figure 4-8,

Figure 4-9, Figure 4-20) but the oxygen detected in as deposited samples can be too high due to an artifact of XPS depth profiling (see p. 57). This could explain these high values.

Table 4-1. Results of resistivity calculations.

№	tested combination	$\rho^{O}_{barrier}$, μΩcm	K, μΩ·cm/
1	Ta(20 nm)/SiLK	68.9	6.8
2	Ta(25 nm)/SiLK	25.8	6.6
3	$Ta_{0.9}C_{0.1}$(20 nm)/SiLK	167.0	6.5
4	$Ta_{90.94}N_{0.06}$(20 nm)/SiLK	176.8	5.6
5	$Ta_{0.92}N_{0.08}$(20 nm)/SiLK	176.6	2.8
6	$Ta_{0.9}N_{0.1}$ (25 nm)/SiLK	192.2	2.5
7	$Ta_{0.95}Si_{0.05}$ (20 nm)/SiLK	171.0	2.3
8	Ta(20 nm)/pSiLK	70.4	8.9
9	$Ta_{0.92}N_{0.08}$(20 nm)/pSiLK	184.0	8.8
10	$Ta_{0.84}N_{0.16}$(20 nm)/SiLK	260.0	30.5
11	$Ta_{0.84}N_{0.16}$(20 nm)/pSiLK	340.0	19.1

4.3.3 Adhesion test

All samples showed a modified surface after the four-point probe sheet resistance measurements at elevated temperature. Figure 4-22 presents a surface image of a Ta film on SiLK. The surface has an “orange skin” appearance. Ta films containing nitrogen (≤10 at%) showed the least changes of the surface. Therefore, these films are expected to have a better adhesion with SiLK film with respect to other Ta-based films.

The four-point bend test was performed on test structures with αSi/barrier/SiLK/SiO_2 stacks on a Si substrate. The Ta film and Ta film containing nitrogen were used as a barrier. The structure breaks at the end of the test.

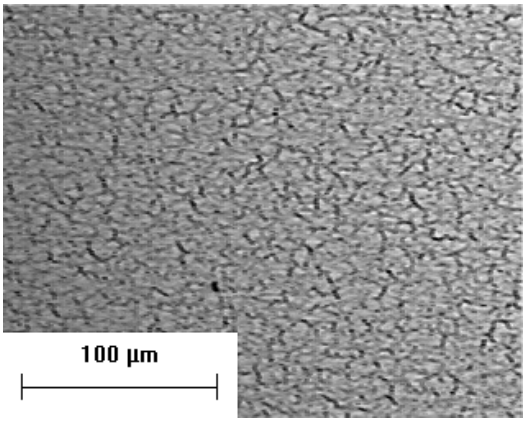

Figure 4-22. Surface image of the αSi/Ta(25 nm)/SiLK/SiO_2/Si stack after 400 ^oC heating in vacuum for 120 minutes.

Figure 4-23 shows an example of two pieces of a tested sample with pure Ta film heated at 250 ^oC. Each part has an open surface of the interface, along which delamination took place. In order to locate the failure in the tested stack, a surface scan of the film on both sides of the breakage is performed with XPS. Figure 4-24 shows these XPS surface scans at the place of delamination. The surface survey shows a Ta signal and a C signal on one side of the breakage (see curve 1 in Figure 4-24). The C signal lies at 284.8 eV, indicating the presence of C_xH_y, which is a common contaminant. On the mirrored side no Ta and an increased C- signal is measured (see curve 2 in Figure 4-24). The detected C-signal lies at 284.8 eV and there is an extra shake-up peak at 292 eV specific for aromatic groups, i.e. in our case SiLK. Thus, the adhesion failure is located at the Ta/SiLK interface. For this interface the adhesion energy can be calculated with the results of the four-point bend test. In some cases, i.e. in samples with $Ta_{0.94}N_{0.06}$ film, the fracture area of the failed interface is not large enough to be evaluated. After the thermal treatment the samples with Ta films containing 8-16 at% nitrogen show delamination due to the thermal treatment. No adhesion energy could be derived from these samples.

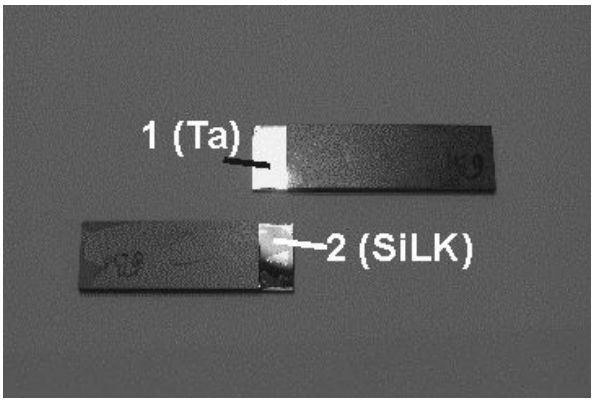

Figure 4-23. Image of a sample broken at the end of four-point bend probe with a failure along Ta/SiLK interface as determined with XPS.

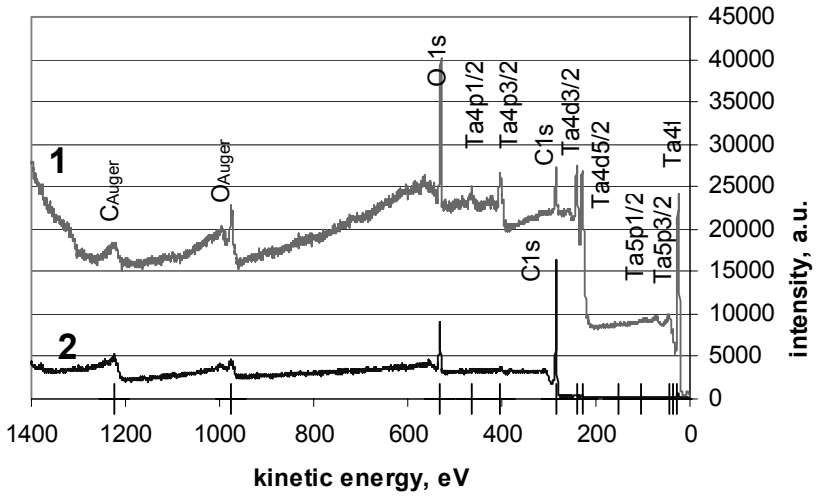

Figure 4-24. Surface scan of failed interface for the sample with a stack of αSi/Ta/SiLK/SiO_2on Si-substrate heated at 250 ^oC for 15 min in N_2 ambient: 1. Ta surface; 2. SiLK surface.

Figure 4-25 presents the adhesion energy calculated from the results of the test for structures with Ta based films (dotted stripes, grey stripes and black stripes in Figure 4-25). The standard deviation is shown as bars. The failed interface, determined with Surface Scan XPS, is noted next to the stripes. In the failed interface of the as deposited stack with the pure Ta film XPS detected signals from Si, Ta and C (dotted stripe in Figure 4-25). The C signal lies at 287.6 eV and belongs to $C_{C=O}$ in glue. In our samples the αSi layer on the Ta film was 2-3 nm thick. As the information depth of XPS is 6 nm, this means that the failure of adhesion occurred either at the Ta/glue or at the αSi/Ta interface. The adhesion energy for this interface is

calculated to be 29 J/m^2. This value, being the least in the stack of glue/αSi/Ta/SiLK/SiO_2/ films on Si substrate, indicates that adhesion energy of the Ta/SiLK and other interfaces is larger. Moreover, this value is relatively high. In similar samples heated at 250 ^{o}C and 400 ^{o}C the adhesion energy between Ta and SiLK is 19.1 J/m^2 and 10.4 J/m^2, respectively (grey and black stripes in Figure 4-25). Thus the adhesion deteriorates after a heat treatment. In practice, the critical energy for an adhesion failure between inorganic materials during CMP (Chemical Mechanical Polishing) is about 5 J/m^2 [13]. This means, that the value of 10.4 J/m^2 is still sufficient to satisfy requirements of CMP (Chemical Mechanical Polishing). The adhesion energy of the interface of SiLK/Ta films containing nitrogen is ≥ 10.5 J/m^2. After a heat treatment, however, the adhesion deteriorates, resulting in films partly delaminated from the SiLK. This is probably due to the good barrier properties regarding oxygen diffusion. This results in the formation of an oxygen- enriched layer at the barrier/SiLK interface and a weakening of this interface. This oxygen enrichment and the high intrinsic stress level in the barrier film (2÷3 GPa) are responsible for the delamination.

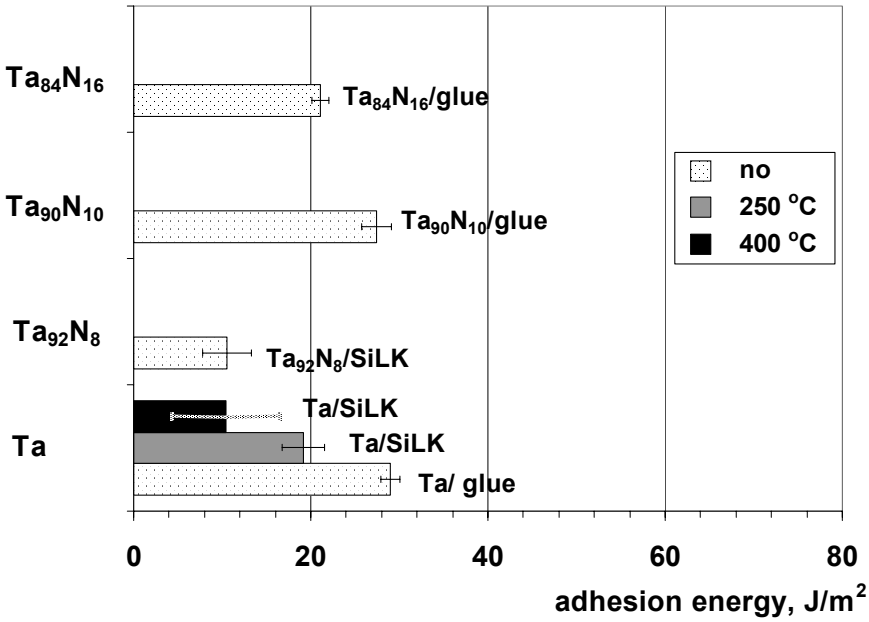

Figure 4-25. Adhesion energy for samples with Ta-based films before and after 15 min heating treatment at 250 ^{o}C and 400 ^{o}C in N_2 ambient.

4.4 Summary and conclusions

After the deposition of the Ta-based barriers on SiLK Ta-C bonds and oxygen present at the barrier/SiLK interface.

During a heat treatment the resistance and the TCR of the barrier film changes. The increase in the resistance of the Ta-based film is mainly caused by the incorporation of oxygen. The SiLK layer serves as the source of oxygen. No further reaction with hydrocarbons from the SiLK has been observed.

The concentration coefficient of the resistivity of Ta is about 6.7 μΩ·cm/at% O. For Ta films containing 8-10 at% N this is about 2.6 μΩ·cm/at% O. The maximum amount of oxygen from SiLK in Ta after heat treatment at 400 ^{o}C is estimated to be 10 at %.

Nitrogen in the barrier limits the incorporation of oxygen. During heating the oxygen is piling up at the barrier/SiLK interface. As a result the adhesion energy decreases and occasionally delamination occurs. The better the barrier against oxygen diffusion, the worse the adhesion at the barrier/SiLK interface.

Four-point bend measurements were performed to determine the adhesion energy of barrier/SiLK interfaces. The adhesion energy for the Ta/SiLK is larger that 29 J/m^2 in the as deposited sample. After heating at 400 ^{o}C the adhesion energy decreases down to 10.4 J/m^2. For as deposited nitrogen containing films (8-16 at% N) similar values have been found.

Ta films containing 8-10 at% N show better performance than pure Ta films being based on the resistance measurements, which show better thermal stability on SiLK, and on the suitable adhesion from the four-point bend tests.

References

1. S. P. Murarka, Metallization: theory and practice for VLSI and ULSI, 1993, ISBN: 0-7506-9001-1.
2. M. T. Wang, Y. C. Lin, and M. C. Chen, Barrier Properties of Very Thin Ta and TaN Layers Against Copper Diffusion, *J. Electrochem. Soc.*, Vol. 145, № 7, p. 2538-2545, (1998).

3. Alain E. Kaloyeros, Xiaomeng Chen, Tanja Stark, Kaushik Kumar, Soon-Cheon Seo, Gregory G. Peterson, Harry L. Frish, Barry Arcles, and John Sullivan, Tantalum Nitride Films Grown by Inorganic Low Temperature Thermal Chemical Vapor Deposition. Diffusion Barrier Properties in Copper Metallization, *J. Electrochem. Soc.*, 146(1), p. 170-176 (1999).
4. E. Kolawa, J. S. Chen, J. S. Reid, P. J. Pokela, and M. A. Nicolet, Tantalum-based diffusion barriers in Si/Cu VLSI metallization, *J. Appl. Phys.* 70(3), p. 1369-1373 (1991).
5. J. Imahori, T. Oku, M. Murakami, Diffusion barrier properties of TaC between Si and Cu, *Thin Solid Films*, 301, p. 142-148 (1997).
6. P. H. Townsend, S.J. Martin, J. Godschalx, D. R. Romer, D.W Smith, Jr. D. Castillo, R. DeVries, G. Buske, N. Rondan, S. Froelicher, J. Marshall, E. O. Shaffer, and J- H. Im, SiLK polymer coating with low dielectric constant and high thermal stability for ULSI interlayer dielectric, *Mat. Res. Soc. Symp. Proc.* Vol. 476, p. 9-17 (1997).
7. P.G. Charalambides, J. Lund, A.G. Evans and R. M. McMeeking, A test specimen for determining the fracture resistance of bimaterial interfaces, *J. Appl. Mech*., 56, p. 77-82 (1989).
8. H. Donohue, H. Gris, J.C. Yeoh, K. Buchanan, Low resistivity PVD α-Ta: Phase formation and integration in ultra low-k dielectric/ copper damascene structures, *International Interconnects Technology Conference 2002*, IEEE catalog number 02EX519C, ISBN 0-7803-72174-4.
9. C.C. Tsuei, Nonuniversality of the Mooij Correlation- the Temperature Coefficient of Electrical Resistivity of Disordered Metals, *Phys. Rev. Lett*., Vol.57, N 15, p.1943-1946 (1986).
10. J.J. van den Broek, J.J.T.M. Donkers, R.A.F. Van Der Rijt, J.T.M Janssen, Metal film precision resistors: resistive metal films and a new resistor concept, *Philips J.Res*. 51, p. 429-447, (1998).
11. W. D. Westwood et al., Tantalum Thin Films, 1975, ISBN: 0127447504.
12. M. Hansen, Constitution of binary alloys, London, McGraw- Hill, 1958.
13. T. Scherban, B. Sun, J. Blaine, C. Block, B. Jin and E. Andideh, Interfacial Adhesion of Copper-Low k Interconnects, *Proc. of the IEEE 2001 International Interconnect Technology Conference (Cat. No.01EX461)*, p. 257-259 (2001).

Chapter 5

Chemical Vapour Deposition of $W_xSi_yN_{1-x-y}$ films

5.1 Introduction

Surface morphology, microstructure and composition are important factors determining the properties of the diffusion barriers. For the deposition of ultra thin layers with conformal step coverage in high aspect ratio features, CVD processes (ALD) are more favorable compared to PVD.

Amorphous films are superior to crystalline regarding Cu diffusion, as enhanced Cu diffusion occurs along the grain boundaries in crystalline barriers.

Tungsten nitrides are promising materials as diffusion barriers due to their non-reactivity with Cu. Tungsten nitrides, however, decompose at 820-850 ^{o}C [1, 2] and some phases crystallize at 450 ^{o}C [2]. Incorporation of Si in tungsten nitrides results in the formation of W-Si-N ternary compounds with a better thermal stability. Reactivity studies of these ternaries showed that Si in the compound can interact with Cu. A N-rich W-Si-N compound with a ratio of W/Si = 1/1.5 was reported as an excellent diffusion barrier [3]. One of the aims of this study is to find the conditions for the growth of tungsten nitride compounds with a low Si content to reduce the reactivity of barriers with Cu.

In this study we used WF_6 as a source for W. WF_6 is a liquid at room temperature. It is easier to use as a precursor than the solid WCl_6, for example. The melting temperature of WF_6 is 275.4 K and its boiling temperature is 290 K, while the melting- and boiling temperature for WCl_6 is 548 K and 619.9 K respectively [4]. Monosilane SiH_4 was used as a Si-source, although the use of disilane is preferable from a thermodynamic point of view [5]. For the incorporation of nitrogen in the ternary compounds NH_3 and NF_3 gas components can be used. Nakajiama [6] reported about adduct formation as a product of reaction between WF_6 and NH_3. In a mixture of WF_6 and NH_3 no reactions occur, at

temperatures up to 600°C, but in the low temperature parts of the reactor it produces an adduct $WF_6 \cdot 4NH_3$. To facilitate the reaction between WF_6 and NH_3 the activation energy for the reaction should be decreased by breaking the W-F bond of WF_6 or the N-H bond of NH_3. This may be reached by adding H_2 gas to the binary mixtures [6, 7, 8, 9]. In this study we used NF_3 as the precursor for the incorporation of N.

Electrical tests are most sensitive for barrier characterisation compared to analytical techniques like AES, XPS and RBS. The reactivity of the barrier to Cu was determined using *in situ* sheet resistance measurements. Because of the presence of Si in W-Si-N, diffusion of Si in Cu could take place. The resistivity of Cu increases from 1.67 to 4.67 μΩcm [10] when only 1 at% of Si is dissolved in Cu. Resistivity changes due to diffusion of Si into the Cu interconnect lead to higher RC delays in devices. C-V and TVS measurements were used to test the diffusion properties of the barriers.

5.2 Process study

5.2.1 Deposition equipment

The growth of $W_xSi_yN_{1-x-y}$ was studied in a cold wall single wafer LPCVD reactor. Schematic of the reactor is shown in Figure 5-1. SiH_4 and WF_6 gases are introduced into the reactor chamber radially via 20 cm diameter injection ring. A system of holes in this ring is configured for more uniform distribution of gases. Ar and NF_3 are injected directly. The system is operated with a roots blower pump with an N_2 purge. The end pressure of the system is $2 \cdot 10^{-3}$mbar and limited by the pump's pressure.

WF_6 served as a W-precursor, SiH_4 as a Si-precursor and NF_3 as a N-precursor. Ar is used as a carrier gas. The WF_6 line was heated at 65°C. The process pressure was 0.2 Torr.

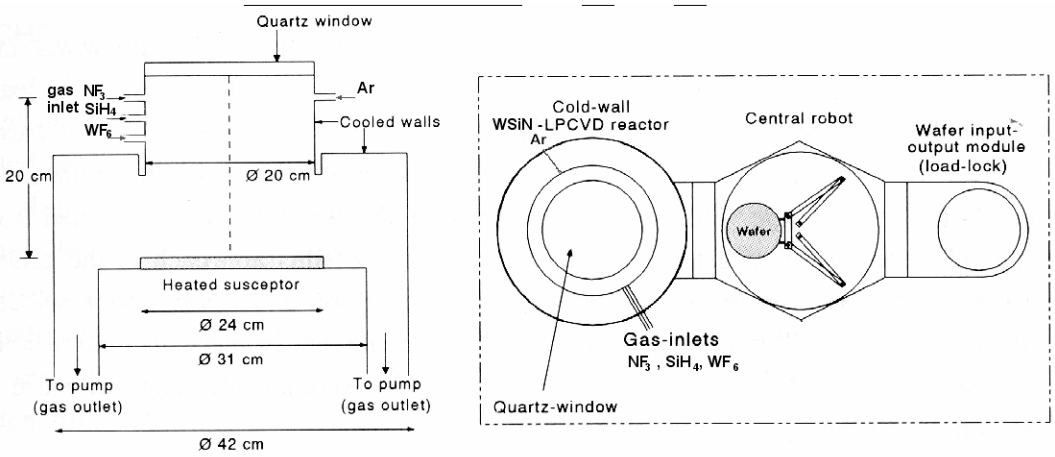

Figure 5-1. Schematic of the LPCVD reactor for W-Si-N layers deposition.

5.2.2 Experimental procedure

5.2.2.1 Film growth

Wafers of n type Si (100) with 3 inch diameter were used. The deposition was carried out on 700 nm thermal oxide grown using water vapor as the oxidizing species (see Chapter 2). The annealing of the interface states was performed at 450 ^oC in N_2/H_2O atmosphere for one hour. Then, wafers were cleaned in fuming nitric acid and in boiling 69 % HNO_3, then rinsed in DI water. After a final dip into a 1 % HF solution for 20 sec, wafers were rinsed in DI water and spin- dried. The prepared wafer was transferred into the deposition equipment. The variable parameters for the process study were flow rate of the gas components SiH_4, WF_6, NF_3 and Ar. The total gas flow was kept at 260 or 1570 sccm. The susceptor temperatures used, were 250 and 385 ^oC. A nucleation step was applied to deposit Si-nuclei before barrier deposition. SiH_4 was used for this purpose for 10 min at 1 Torr.

5.2.2.2 Film properties

AES (Auger Electron Spectroscopy) was applied to determine the film composition. Depth profiling was done with an Ar^+ ion beam of 1.5 kV. RBS and XPS profile analysis were applied for a comparative study of film composition. XPS depth profiles were obtained with a 5 kV Ar^+ ion beam with an area of 3 x 3 mm^2. Standard sensitivity factors were used to calculate concentrations. RBS was done with 2 MeV He^+ ions on an area of 1 mm^2. RMS-roughness was measured with AFM. Thickness was

measured with an SEM and a Dektak profilometer. The resistivity of films was calculated based on sheet resistance (measured with four-point probe method) and the measured thickness. The density of the layers was calculated as weight increase divided by measured thickness and wafer area.

5.2.3 Results and discussion

5.2.3.1 Composition and morphology

A study of $W_xN_ySi_{1-x-y}$ deposition showed the existence of ternary compounds with different concentration of each element. N-rich compounds were reported as effective diffusion barriers [5] with diffusion properties tested on n^+/p diodes.

CVD of films was carried out with a gas mixture of WF_6, NF_3, SiH_4 and Ar. The Ar flow was balanced to keep the total flow constant. In order to study the influence of reactive gasses on the composition, we changed the flow of one of the gasses. Under this condition the partial pressure of the gas was changed. The ratio between reactive gasses in the gas mixture was also altered. Results of our thermodynamical calculations (see Chapter 3) were used as an input to define the deposition conditions and the compound formation versus ratio of reactive gasses.

Deposition at 385 ^oC

The influence of the fraction of SiH_4

The fraction of SiH_4 was varied between 0.60 and 0.78 at a flow ratio of NF_3/WF_6 of 1. Composition and density of the films are shown in Table 5-1, №1- 5. When the ratios of SiH_4/WF_6 and SiH_4/NF_3 were equal to 3 the layers contained W, N, O, but no Si (see № 1 in Table 5-1). These layers were porous with a low density, 3.8 g/cm^3. Figure 5-2 shows a SEM picture of the film deposited at a SiH_4/WF_6 ratio of 3. These films containing ~13 at% O had an open porous structure and a poor adhesion to SiO_2.

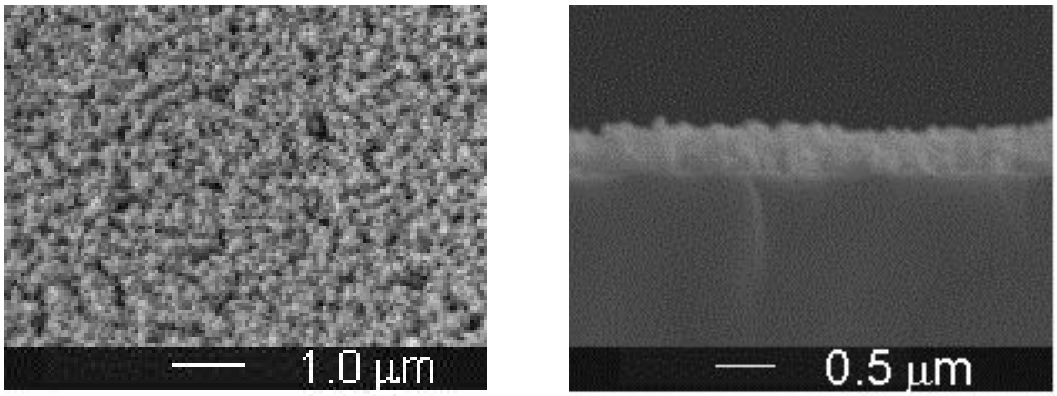

Figure 5-2. SEM image for a film deposited at WF_6:NF_3:SiH_4=10:10:30 at 385°C deposition time 3min. with a composition $W_{0.55}N_{0.32}O_{0.13}$: a) surface; b) cross- section.

Table 5-1. Composition of films measured with AES. The deposition is carried out at 385°C and 0.2 Torr for 6 ½ min.

№	SiH_4/ WF_6	NF_3/ WF_6	density, g/cm^3	compound W-Si-N-O*, at%	fraction of SiH_4**
1	3	1	3.8±5%	55-0-32-13	0.60
2	4	1	9.2±8%	52-7-41-0	0.67
3	5	1	10.0±16%	53-5-42-0	0.71
4	6	1	7.0	57-35-8-0	0.75
5	7	1	8.9	55-36-9-0	0.78
6	6	2		53-32-6-9	0.67

**AES analysis gives a mismatch with real compositions due to uncertain sensitivity factors and preferential sputtering of N.*

*** The fraction of SiH_4 in the reactive gas mixture was calculated as the flow of SiH_4 divided by the sum of flows of reactive gases.*

Our thermodynamical calculations show the onset of Si incorporation (as W_5Si_3) is postponed by the use of NF_3. Without NF_3 in the gas phase Si inclusion starts if the SiH_4/WF_6 ratio is 1.5 (see Chapter 3, figure 3-1). This is in agreement with results of W deposition from WF_6 and SiH_4 where the onset of a considerable Si incorporation is reported to start when the SiH_4/WF_6 ratio is 1.5 [11]. The use of NF_3 (NF_3/WF_6 = 1) moves the Si incorporation to the ratio of SiH_4/WF_6 equal to 3. It means that any Si formed locally will be etched by NF_3, probably with inclusion of fluorine products in the growing layer. Due to a high reactivity of

fluorine with moisture from the air the reaction with liberation of HF can occur with a substitution of fluorine by –OH groups. This could explain why the layers, deposited at a ratio of SiH_4/WF_6 equal to 3, had a high concentration of oxygen (13 at.%) and no Si.

When the SiH_4/WF_6 and SiH_4/NF_3 ratio was increased to 4-5, a small amount of Si was incorporated. The composition of these films was $W_{0.52}Si_{0.07}N_{0.41}$ (see № 2, 3 in Table 5-1) as determined by AES. This can be written as $W_{1.3}NSi_{0.2}$. These films have a substantially higher density, 9.2-10 g/cm^3. A SEM image of such a layer is shown in Figure 5-3. These films passed the conventional "scratch and scotch-tape" adhesion test on SiO_2.

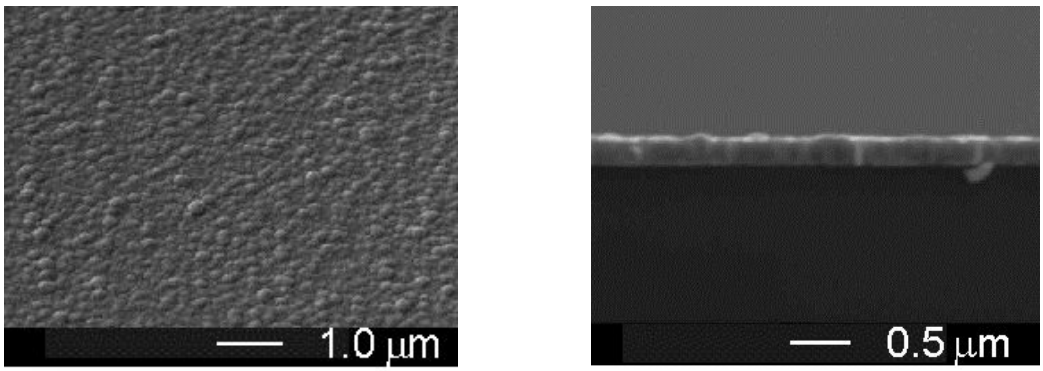

Figure 5-3. SEM image for a film deposited with a flow ratio of WF_6:NF_3:SiH_4=10:10:50 at 385^{o}C. Deposition time 6$^1/_2$ min. Composition $W_{0.53}Si_{0.05}N_{0.42}$: a) surface; b) cross-section.

When the ratio of SiH_4/WF_6 is increased up to 6-7, the layers are tungsten silicide with a small amount of N, $W_{57}Si_{35}N_8$ (see № 4, 5 in Table 5-1). The composition can be written as $W_{1.6}SiN_{0.2}$. These films had a good adhesion to SiO_2. Figure 5-4 shows the SEM image of the film deposited with a SiH_4/WF_6 ratio of 7. It is a polycrystalline film with grains of 50-70 nm in diameter.

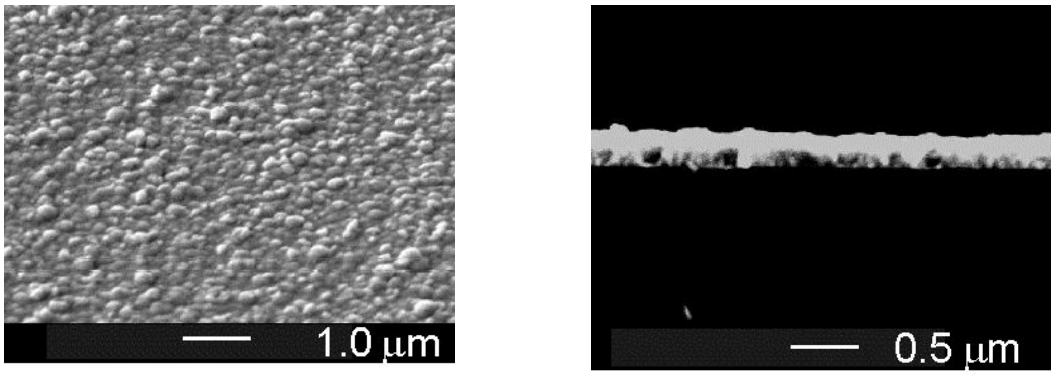

Figure 5-4. SEM image for the film grown at WF_6:NF_3:SiH_4=10:10:60 at 385°C. Deposition time $6^1/_2$ min. Composition $W_{0.57}Si_{0.35}N_{0.08}$: a) surface; b) cross- section.

We found that at conditions studied two kinds of ternaries $W_xSi_yN_{1-x-y}$ could be grown, N-rich and N-poor. The composition of these compounds was $W_{1.3}NSi_{0.2}$ and $W_{1.6}SiN_{0.2}$, respectively. The growth of compounds with a low silicon and a large N content is possible only within a narrow range of SiH_4/WF_6 ratios, 4-5. The compound obtained at a flow ratio of SiH_4/WF_6 of 3 was tungsten nitride. The films grown at a flow ratio of 6 and 7 were tungsten silicides with a low N concentration. Thus, a small increase of the SiH_4/WF_6 ratio results in a large change of the Si incorporation. This effect is similar to the one for CVD of W-based films using WF_6 and SiH_4 as precursors.

In that system the W-growth occurred without Si inclusion within a narrow range of SiH_4/WF_6 flow ratio of 0.55-1.3 [11]. For the flow ratio of SiH_4/WF_6 between 1.5 and 2 a sharp increase of Si content was observed, i.e. from 7 at% of Si in films up to 35 at% as determined with AES [11].

In our case the use of extra reducing gas NF_3 moves the starting conditions for the Si incorporation (5-7 at%) towards a larger ratio of SiH_4/WF_6 than in the study of Schmitz [11], i.e. from 1.5 up to 4. An abrupt increase of the Si inclusion (35 at%) is postponed till the ratio SiH_4/WF_6 of 6. Therefore, in our case it is possible to deposit a film with a desirable low Si content in a very narrow range of the SiH_4/WF_6 ratios, i.e. 4-5, at a flow ratio of NF_3/WF_6 of 1.

At the beginning of the process the substrate surface is covered with Si-nuclei (see 5.2.2 Experimental procedure). At the surface of the growing film three gas components compete for adsorption sites. SiH_4 can be adsorbed as SiH_x, WF_6 as WF_x and NF_3 as NF_x, alike NH_3 on W [12]. The sticking probability of NF_3 is lower than that of WF_6 and SiH_4. As soon as W or W-silicide is formed and the surface conditions have been changed, the probability of adsorption for gas components is changing. If the SiH_4 fraction is not high enough to reduce all WF_x and NF_x, some F-products will be trapped into the growing film. As a result, the deposited film can be porous and will be oxidized easily, as we have observed for the SiH_4/WF_6 ratio of 3. With an increase of SiH_4/WF_6 ratio up to 4-5, the SiH_4 fraction becomes high enough for the reduction of both WF_6 and NF_3 species. Almost all Si will be removed as SiF_4 or $SiHF_3$. In this case, films of tungsten nitride with a low Si content are deposited. The higher fraction of SiH_4 (at ratio of $SiH_4/WF_6 \geq 6$, in our case) with a combination of high reactivity with WF_x, the less NF_3 fraction can be adsorbed at the growing surface. This results in the growth of tungsten silicides with a corresponding decrease of N-content in deposited films.

RMS roughness was measured with AFM for the layers deposited at the SiH_4/WF_6 ratios in the range of 4-7. Films with a thickness of about 70 nm were characterized with an RMS in the range of 2.9-5.9 nm.

The influence of the fraction of NF_3

No substantial change of W, N, Si concentrations is obtained at an increase of the NF_3 fraction from 0.13 up to 0.22 at a SiH_4/WF_6 ratio of 6 (see Table 5-1, № 4, 6). However, a morphology modification has been observed. Figure 5-5 shows SEM images of such a layer. There are porous clusters on the surface of the grown film (see Figure 5-5 a). The clusters have a poor adhesion to the underlying film, adhering to the film in a much smaller area than the cross section of the cluster (see a tilted ($<10^{o}$) cross section image in Figure 5-5 b). The Si/W ratio in these clusters and in the film are the same as observed with Scanning Auger Microscopy (SAM). All clusters have a similar size. These observations suggest that the growth mechanism was changed from non-selective (the film growth controlled by mass-transport) to selective (the cluster growth

controlled by surface reactions). The clusters grew selectively on a few active sites available for adsorption, where the growth continued. The equal size of the clusters indicates that the selective growth occurred with the same rate, where active sites were available at the beginning of selective growth. The big size of the clusters (with a diameter of ~1 μm) indicates a very high growth rate (see Figure 5-5 a).

The phenomenon of selective growth has been observed in the W-CVD on Si wafers partly covered with SiO_2 [11, 13]. In this case W grows selectively on Si. No growth occurs on SiO_2, therefore the concentration gradient within a boundary layer is negligibly small. As a result, the growth on Si occurs under high concentrations of precursors in a regime limited by surface reactions with an extremely high deposition rate.

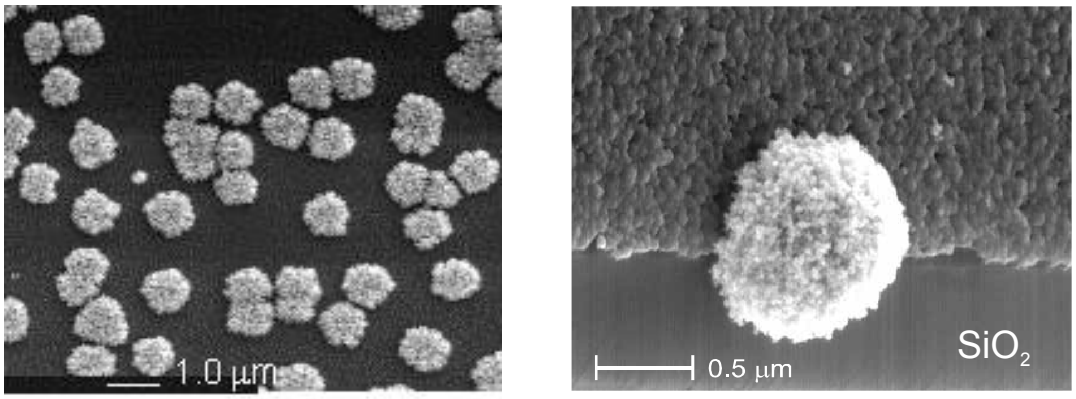

Figure 5-5. SEM image for the films deposited at 385 ^oC at 0.2Torr and total gas flow 260 sccm with Ar used as a diluent gas. Flow ratio NF_3/WF_6 = 2, and SiH_4/WF_6= 6. Deposition time 6 $^1/_2$ min. a). surface; b). tilted cross section.

Before selective growth of clusters started the deposition process passes two stages: at first the growth of W nuclei at the cost of the Si-nucleation film, then a reaction occurs between WF_6 and SiH* preferentially adsorbed on the W film. The ratio of SiH_4/WF_6 is so high that a tungsten silicide can be formed. The adsorption of NF_3 species on the growing film takes place in parallel with the growth of tungsten silicide. When the W-nuclei are covered with tungsten silicide the sticking probabilities are changed. In this case (compared with a NF_3/WF_6 ratio of 1) the NF_3 fraction in a reactive gas mixture is so high that the surface coverage of other species is diminished. The amount of SiH* (reducing species) on

the surface is not enough for a reaction resulting in a W-N bond formation and removing of F-products. As a result, the film growth is stopped. A few reactive sites are, however, available for the chemisorption of SiH_x species and their reaction with WF_6 providing a continuous (in time) growth of tungsten silicide clusters. The equally large size of clusters and their local growth indicate that the growth occurs at the same high rate and therefore equal high partial pressures of reactive gases at all locations of growth. Thus, this process is limited by surface reaction. Thus, a large fraction of NF_3 a preferential NF_3 adsorption can block the free surface sites, either stopping growth of the film or changing the growth mechanism, e.g. from non-selective (continuous films) to selective (clusters). In our study, the transition occurs at a slight increase of NF_3 fraction in the reactive gas mixture from 0.13 up to 0.22. Thus, the growth process is very sensitive to the fraction of NF_3. The varying NF_3 fraction does not influence the N-content in films at high flow ratios of SiH_4/WF_6.

Thus, the increase of the NF_3 fraction can result in the poisoning of the available reactive sites followed by a change of the growth mechanism and, as a result, the morphology change of the film.

The study of the growth at these conditions (at increased NF_3 fraction) was complicated due to the change in morphology (growth mechanism) and poor reproducibility (about ±40%) of the process after the cluster formation. The poor reproducibility can be caused by readsorption of secondary products, such as tungsten subfluorides coming off the reactor walls and susceptor.

Deposition at 250 ^oC

Experiments carried out at 250 ^oC resulted in film growth without N incorporation. This was determined with AES and XPS. No bonds with N were measured. The deposited layers represented tungsten silicides. Thus, this temperature was too low for a formation of W-N bonds.

5.2.3.2 Results XRD

XRD 2θ spectra are presented in Figure 5-6 for films grown at a different ratio of SiH_4/WF_6. A summary of the XRD measurements is presented in Table 5-2. The spectrum for a layer deposited with a SiH_4/WF_6 ratio of 3 shows peaks at $2\theta \approx 40^o$, 60^o, 74^o (see Figure 5-6, curve 1). These peaks could be assigned to (β-W, W_3O), (W_2O, WO_2) and (δ-WN), respectively. Thus, this film can be a mixture of tungsten oxides and tungsten nitride phases. The XRD spectrum for the film grown with a ratio of SiH_4/WF_6 ratio equal to 4÷5 reveals peaks at $2\theta \approx 38^o$, 44^o, 64^o, 76.5^o (see Figure 5-6, curve 2). Each peak can be attributed to β-W_2N. No peaks for a phase, containing Si, were observed although some Si (<7 at%) was detected by AES (see Table 5-1). The density of the grown films was ~ 10 g/cm^3, which is substantially lower than the standard density of β-W_2N, 17.8g/cm^3 [4]. This large difference in density could be due to porosity or a second amorphous phase of e.g. WN_2 or Si which cannot be detected by XRD. E.g the density of WN_2 can be as low as 7.7 g/cm^3 and a fraction of this in the amorphous phase could explain the lower density.

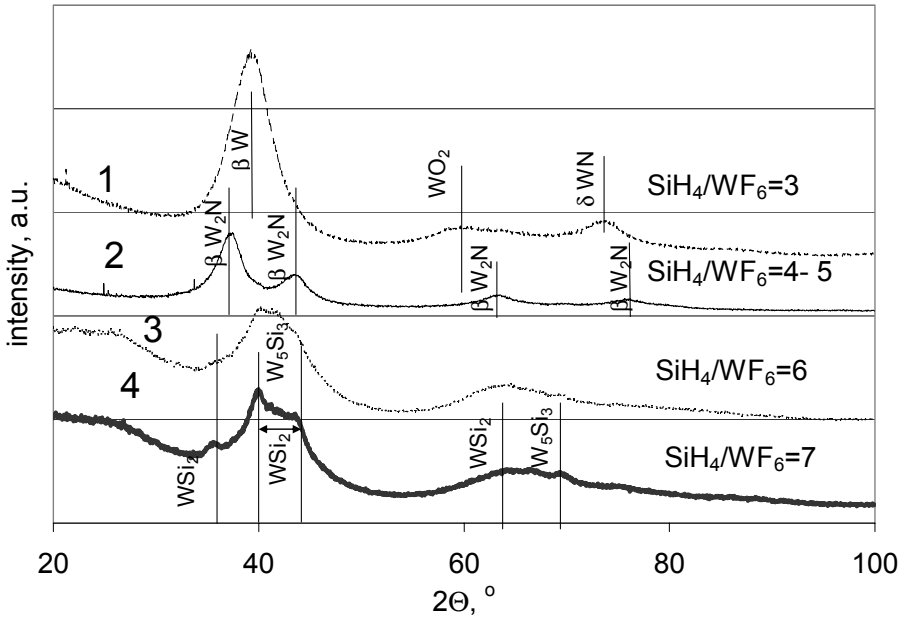

Figure 5-6. Θ-2Θ XRD spectra for the films grown at 385 °C under 0.2 Torr with a varying ratio of SiH_4/WF_6 and a constant ratio of NF_3/WF_6 equal to 1.

There are several wide peaks in the spectra of layers grown with a ratio of SiH_4/WF_6 of 6-7 (see Figure 5-6, curves 3, 4). Peaks at $2\theta \approx 36^o$ and 64.6^o could belong to a cubic phase of WSi_2. A peak at $2\theta \approx 70^o$ can be due to the tetragonal phase of W_5Si_3. Peaks in the range of 40-44° could belong to a cubic WSi_2 or tetragonal W_5Si_3 phase. Thus, compounds grown with a ratio of $SiH_4/WF_6 > 5$ consist mainly of tungsten silicides. The small amount of nitrogen (<9 at %) as determined with AES is not visible to XRD, being included in a tungsten nitride amorphous phase in the films, which cannot be determined with XRD.

Table 5-2. Peaks determined with XRD, composition with AES for films grown with a varying ratio of SiH_4/WF_6.

№	SiH_4/WF_6	Peak by XRD	Composition with AES
1	3	for a hexagonal δ-WN, tungsten oxides	$W_{1.7}NO_{0.4}$
2	4-5	for a cubic β-W_2N	$W_{1.3}NSi_{0.2}$
3	6	a very broad peak: for tetragonal W_5Si_3, cubic WSi_2	$W_{1.6}SiN_{0.2}$
4	7	for tetragonal W_5Si_3, cubic WSi_2	$W_{1.6}SiN_{0.2}$

XRD results confirmed a change of the growth of phases from cubic β-W_2N with a Si-concentration < 7 at% to the growth of tungsten silicide with a concentration of N< 9 at%, when the ratio of SiH_4/WF_6 increases from 5 up to 6. A further increase up to 7 results in more prominent and narrow peaks. This can be due to the formation of films with bigger grains than at the ratio of 6.

5.2.3.3 Growth rate

For the growth study $W_xN_ySi_{1-x-y}$ films were deposited at 385 °C at a total pressure of 0.2 Torr. No ternary compounds were deposited at 250 °C, therefore the film growth at this temperature was out of further interest in this study. The deposition of $W_xN_ySi_{1-x-y}$ was investigated at a different flow ratio of SiH_4/WF_6 (4, 5, 6) and a fixed flow ratio of NF_3/WF_6 of 1. The total gas flow was 260 or 1570 sccm. Figure 5-7 shows the weight increase of the films grown as a function of time. The deposition rate is proportional to the slope (weight increase/time) of the line. For a total gas flow of 260 sccm, the deposition rate was 2.28 and 1.48 mg/min for a

SiH_4/WF_6 ratio of 4 and 5, respectively (see squares and triangles in Figure 5-7). The grown films were N-rich compounds. When the density of the layers is included in the calculations, the growth rate is 55 and 35nm/min, correspondingly. This is too high from the point of barrier application, as the required thickness is less than 10 nm. Table 5-3 presents the summary of density and growth rate of the grown layers. To decrease the growth rate, we lowered the inlet partial pressure of reactive gases by a factor of ~7.5. For this purpose the Ar flow was increased, providing a total gas flow equal to 1570 sccm at a total pressure of 0.2 Torr. At these conditions the growth rate was 2.48 mg/min for a SiH_4/WF_6 ratio of 5 (see diamonds in Figure 5-7). The density of the layers decreased, resulting in an increase of the growth rate up to 70 nm/min. The composition of films changed: the nitrogen content became substantially lower and the Si content considerably higher. The deposited compound had a composition of $W_{0.63}Si_{0.31}N_{0.06}$. This can be written as $W_2SiN_{0.1}$. This change occurred due to the influence of the total gas flow on the boundary layer [14]. A change of the composition of the layers indicates the change at the surface of partial pressures of the reactive gases available for a growth of films. Thus, the influence of the total gas flow rate on the growth rate and composition shows that the growth occurs in a mass-transport regime limited by a diffusion.

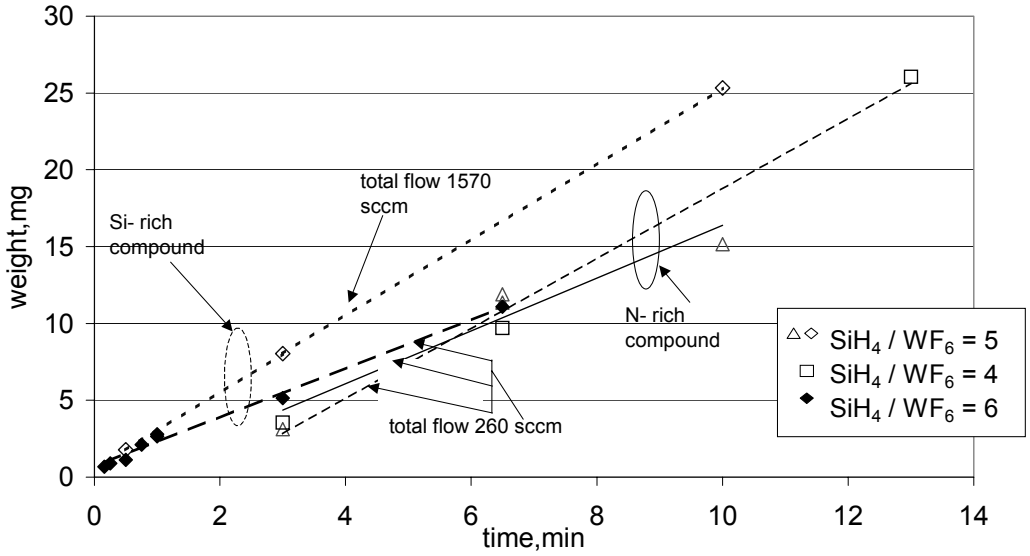

Figure 5-7. (Weight increase-time) dependence for films grown at 385 ^oC and 0.2 Torr.

Table 5-3. Growth rate and density of the films grown with NF_3/WF_6=3 at 385 ^oC and 0.2 Torr.

№	SiH_4/ WF_6	total flow, sccm	growth rate mg/min	growth rate, nm/min	density, g/cm^3
1	4	260	2.28	55± 5	9.2± 0.8
2	5	260	1.72	35± 6	10± 1.6
3	6	260	1.59	46± 4	7.6± 0.6
4	5	1570	2.48	70± 3	7.8± 0.2

5.2.3.4 Comparison AES, RBS and XPS results

It is known that the N concentration determined with analytical profiling techniques is lower than the real concentration due to preferential sputtering of N and the sensitivity factors used for the calculations of concentrations [15]. In order to find the real N-content in the films a comparative study of composition with AES, RBS and XPS was carried out. The measurements were performed on an N-rich ($W_{1.3}NSi_{0.2}$) and an N-poor ($W_2SiN_{0.1}$) compound, as determined with AES. The results of the study are presented in Table 5-4. For the N-rich compound the N content determined with RBS is much larger than that with AES or XPS (see № 1 in Table 5-4). This can be explained by preferential sputtering of N [15, 16] in the depth profiling. The amount of Si determined with RBS for the film with a low Si content is twice smaller than the value with AES, whereas no Si was determined with XPS (see № 1 in Table 5-4). The big difference between N and Si concentrations determined with AES and XPS is owed to the sensitivity factors used in these analyses.

Table 5-4. Composition of CVD- $W_xSi_yN_{1-x-y}$ compound.

composition / №	analytical techniques		
	AES	RBS	XPS
1	$W_{1.3}NSi_{0.2}$	$WNSi_{0.1}$	$W_{2.7}N$
2	$W_2SiN_{0.1}$	$W_2Si_{2.8}N_1$	W_2Si

For the film with a large Si content, RBS determined a much larger amount of Si and N than AES and XPS (see № 2 in Table 5-4). No W-N bonds were found with XPS. Only a small N concentration was determined with AES. The smaller N content determined with XPS and AES is also due to the preferential sputtering. Also in this case, the difference between N and Si concentrations determined with these profiling techniques is owed to the sensitivity factors used.

Thus, the real N concentration in the studied compounds is higher than determined with AES, whereas the real Si content is lower in the N-rich compounds and higher in the N-poor compounds.

5.2.3.5 Film resistivity

Figure 5-8 shows the isothermal cut of the ternary phase diagram with the resistivity of the films grown at 385 ^{o}C. The composition plotted in Figure 5-8 is determined with AES. The real position for compounds in the diagram will be shifted towards higher N or Si concentration due to effects described in 5.2.3.4 as it is shown by the arrows. As it is shown in Figure 5-8, layers of $W_2SiN_{0.1}$have the lowest resistivity, 550-600 μΩcm, compared to resistivities of the films grown with a high W and N-content, 1300-3000 μΩ·cm. This is in good agreement with literature [5, 8]. $W_{1.3}SiN_{0.2}$ compounds are characterised with a resistivity of 830, 890 μΩcm. The compounds with resistivities of 550-880 μΩcm satisfy the requirements for barriers on resistivity. No conditions for deposition of films rich in N and W with a suitable resistivity have been found.

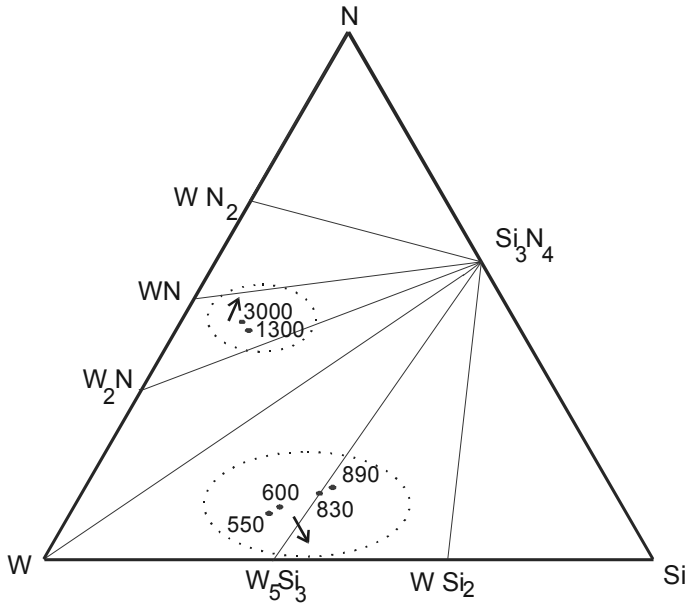

Figure 5-8. Resistivity of compounds, μΩcm in the isothermal cut of the ternary phase diagram for W-Si-N. The plotted composition has been determined with AES. The actual composition is expected to shift along arrows within the dashed areas due to sensitivity factors used and preferential sputtering.

Thus the resistivity of $W_2SiN_{0.1}$ and $W_{1.3}SiN_{0.2}$ compounds (<1000 μΩ·cm) is appropriate for barrier application. The growth rate of $W_{1.3}SiN_{0.2}$ and $W_2SiN_{0.1}$ is 46 and 70 nm/min (see Table 5-3, № 3, 4), respectively. Thus, the combination of the lower growth rate and satisfactory resistivity makes $W_{1.3}SiN_{0.2}$ a good candidate for the Cu-diffusion barrier, providing that the Si present will not react with Cu (see 5.3.2). In N-rich ternaries the Si/W ratio can be as high as 1.5 [3]. A low N content and a high Si content suggest that special attention should be paid to the reactivity of this material with Cu.

5.2.3.6 Summary

Experiments showed a strong dependence of composition on temperature and fraction of SiH_4 in the gas mixture. Additionally, there is a dependence of the growth rate and composition on the flow of Ar-diluent gas. The growth is limited by diffusion of precursors. Tungsten nitrides with Si< 7 at% ($W_{1.3}NSi_{0.2}$) and tungsten silicides with N< 9 at% ($W_{1.6}SiN_{0.2}$) were grown at 385 ^oC. The composition of the ternaries changes abruptly with an increase of SiH_4 in the gas mixture from 50 to

60 sccm. This change results in a rise of Si by a factor of 5. The respective decrease of N is also by a factor of 5. Such a dramatic change makes a control of the composition in this range not feasible.

An increase of NF_3 flow from 10 to 20 sccm at a fixed SiH_4/WF_6 ratio of 6 results in a transition of non- selective growth mechanism to selective. There is no influence of the NF_3 fraction in the gas mixture on the N-content in films at high flow ratios of SiH_4/WF_6.

The deposition rate of the films was 35-70 nm/min. The RMS roughness of 70 nm W-Si-N films was 2.9-5.9 nm.

The resistivities of $W_{1.3}NSi_{0.2}$ and $W_{1.6}SiN_{0.2}$ are 1300-3500 and 550-890 $\mu\Omega$·cm, respectively.

No detectable W-N bonds were formed in compounds obtained at 250 ^oC.

The combination of resistivity and composition makes $W_{1.6}SiN_{0.2}$ a good candidate for a Cu- diffusion barrier. However, the actual Si content can be much higher. Based on RBS the ratio Si/W can be larger than 1.4. This requires a study of a reaction between Cu and the Si in the compound.

5.3 Electrical characterisation

First, the reactivity of the compounds with Cu has been tested. When Si dissolves in Cu, the resistivity increases by 3 $\mu\Omega$cm per 1 at% of Si [10]. From this point of view a good diagnostic tool of barrier reaction is sheet resistance measurements during temperature treatment.

Investigation of behavior of Cu/barrier/SiO_2/Si system is important for the application of the material in multilevel interconnection.

5.3.1 Experimental procedure

Cu/barrier/SiO_2/Si stacks were prepared by the thermal oxidation of Si wafers followed by the deposition of the barrier and Cu. Barriers with a thickness of 70 nm were deposited at a ratio of NF_3/WF_6 equal to 1 with

different flows of SiH_4 to deposit compounds with different Si content. The Cu-films were DC sputtered with a thickness of 200 nm. Samples $Cu/SiO_2/Si$ stack (without barrier) and with sputtered 100 nm layer of Ta as a barrier were prepared as references. The obtained samples were used for a four-point probe *in situ* sheet resistance measurements under vacuum. During the measurements temperature was increased up to 150 ^oC with 0.01 grad/s and up to 690 ^oC with 0.00833 grad/s. The heater was switched off and the sample cooled down to 25 ^oC. The composition of layers in the stacks was determined by RBS (Rutherford Backscattering Spectroscopy) before and after the test.

Capacitors with Cu/barrier-contact to SiO_2 were fabricated on n-type Si wafers (1-10 Ωcm) with a thermal oxide grown 700 nm thick. Barrier films ($W_{1.6}SiN_{0.2}$ and $W_2SiN_{0.1}$) were deposited with a thickness of 70 or 100 nm. The Cu films 200 nm thick were deposited as it was described earlier. A contact area was defined by photolithography. Cu contact was formed in a 5% solution of HNO_3 and the barrier was etched in a CF_4+10% O_2 plasma. Capacitors with Cu-contact to SiO_2 were made as references. Samples received a heat treatment at 400 ^oC, 500 ^oC and 550 ^oC for 30 min. in vacuum under $2 \cdot 10^{-5}$ mbar. Samples as patterned and heat treated were measured. C-V measurements were done with a HP 4140B pA meter as a DC voltage source, a HP 4275 multi-frequency meter and the MDC CSMWin computer program at 10kHz. TVS (Triangular Voltage Sweep) measurements were performed at 250 ^oC after a stress in electrical field at +1 MV/cm.

5.3.2 Four-point probe resistance

5.3.2.1 Reference samples

Results of the four-point probe *in situ* sheet resistance measurements are shown in Figure 5-9 as the normalised resistance versus temperature.

$Cu/Ta/SiO_2/Si$

The increase of the normalised resistance by a factor of 2.4 during heating is caused by the resistivity dependence on temperature. The calculated temperature coefficient of resistivity (TCR) for Cu was about $2.85 \cdot 10^{-3} K^{-1}$, which is in agreement with literature, $2.99 \cdot 10^{-3} K^{-1}$ [17] and

in the same order of magnitude as $4.3 \cdot 10^{-3} K^{-1}$ [10]. After the annealing cycle the resistance of the Cu/Ta stack decreased by a factor of 0.92 due to curing of defects in the Cu and Ta. However this phenomenon was not in the focus of this study. This decrease in resistance demonstrated that the Cu was not doped with Si and the Ta is an appropriate reference sample for our investigation up to 690°C.

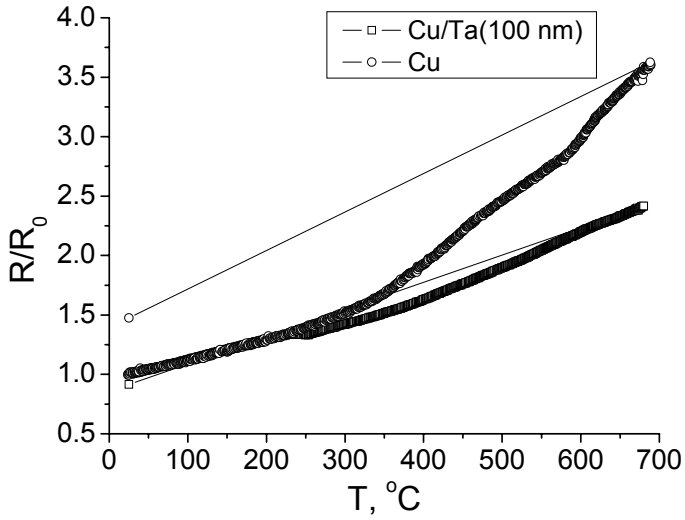

Figure 5-9. Normalised resistance versus temperature for Cu/Ta/SiO_2, Cu/SiO_2/Si stacks. Metallisation contact to SiO_2 is shown in the legend.

Cu/SiO_2/Si

Resistance increases up to 350 °C with the same TCR as for Cu/ Ta reference. Between 350 and 580 °C the slope of the plot increases. Above 580 °C the slope of resistance line changes again. These changes can indicate a reaction of Cu with underlying film. The resistance of a cooled down sample increased by a factor of 1.5. Additionally, the TCR of Cu after heating has changed. The resistance increase and change of TCR suggest that compositional changes have taken place in the Cu. The amount of Si of $3 \cdot 10^{15}$at/cm^2 in Cu after the test is in agreement with resistance measurements. This amount is equivalent to 0.5 at% of Si. It is not likely, however, that SiO_2 is a source of Si diffusion, because Cu is not likely to reduce SiO_2. RBS results show some Ar present at the Cu/SiO_2 interface. Therefore, ion (Ar) bombardment of the SiO_2-Cu

interface during the Cu deposition process can result in the breaking of Si-O bonds. Thus, some free Si can be available for a diffusion in Cu.

5.3.2.2 Samples with barriers

The Si/W ratio in the tested barriers is in the range of 0.8-1.4 as determined with RBS. The N concentration is about 6- 9 at%. Figure 5-10 shows a change of normalised resistance with temperature for the samples with Cu/Ta, as a reference, and Cu/barrier combinations deposited on SiO_2. The resistance of the reference sample increases according to the TCR of Cu (Figure 5-10, a). The resistance of samples with a Cu/barrier combination with a Si/W ratio of 0.8 follows the same line up to 350 ^oC (Figure 5-10, b). Above 350 ^oC the slight deviation from the reference line is observed. This can correspond to a start of the reaction between Cu and a barrier, i.e. alike to Cu/SiO_2 sample some free Si can be available for a reaction at the Cu/barrier interface. Above 550 ^oC the resistance increases drastically with temperature. This temperature was defined as the temperature of the failure of non- reactivity requirements for barriers. With the increase of Si/W ratio in the barrier up to 1.4 the temperature of abrupt increase of resistance decreases down to 450 ^oC, whereas the temperature of the slight deviation is 350 ^oC and the same for all kinds of tested compounds, (e.g. Figure 5-10 c). Cu was not detected in the barrier layer by RBS after a large change of resistance. On the other hand, Si was determined in the Cu layers. Thus, atomic Cu diffuses into the barrier much slower than Si from the barrier material. The increase in measured resistance is ascribed only to the Si diffused from the barrier into the Cu, because the resistance of Cu and barrier, as two resistors in parallel, is determined by the layer with the lowest resistance (Cu).

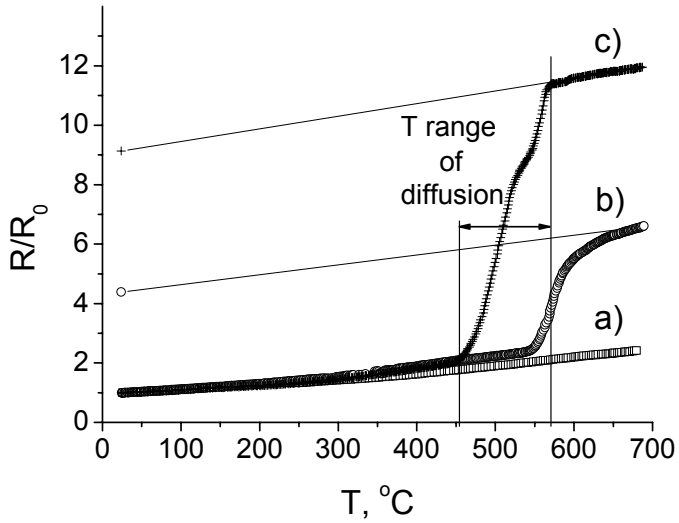

Figure 5-10. Typical plot of normalised resistance versus applied temperature: a) reference; b) Cu/barrier stack with Si/W ratio in a barrier equal to 0.8 before heating; c) Cu/barrier stack with Si/W ratio in a barrier equal to 1.4.

Figure 5-11 shows the Si/W ratio in barriers before the heating and corresponding temperature of the non-reactivity requirements failure in the range of 450-550 ^{o}C. The temperature of the failure for $WSi_{1.4}$ is different than for a ternary compound with the same Si/W ratio of 1.4 (dashed line in Figure 5-11). Therefore the ratio of Si/W in the barrier is not the only factor determining the diffusion process. The morphology of the layer and how Si is bonded to W are important parameters that determine the process of diffusion. If the comparison of barrier stability, in respect of Si release, is made among layers with a similar texture, whether $W_xSi_yN_{1-x-y}$, or W_xSi_{1-x}, the material with the lowest Si content serves as the best one.

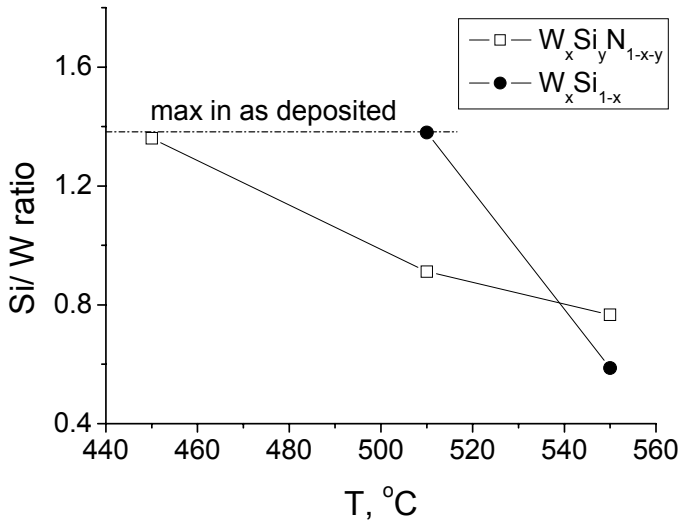

Figure 5-11. A Si/W ratio in the barrier layer before the test versus temperature of considerable rise of resistance.

Figure 5-12 presents the concentration of Si in Cu after heating and the corresponding temperature of the failure. The amount of Si dissolved in Cu is proportional to temperature, at which the reaction between a barrier and Cu starts. A comparison of Figure 5-11 and Figure 5-12 shows that the smaller Si/W ratio, the less Si is dissolved in Cu after heating. Thus, the reactivity of compounds with Si becomes less with decreasing Si/W ratio. The largest increase of resistance by a factor of 9.1 is related to ~10.4 at% of Si dissolved in Cu. This value approaches the solubility limit of Si in the Cu, which is 11.7 at% [18]. Thus, no copper silicide has been formed and a concentration coefficient of resistivity for Si can be calculated.

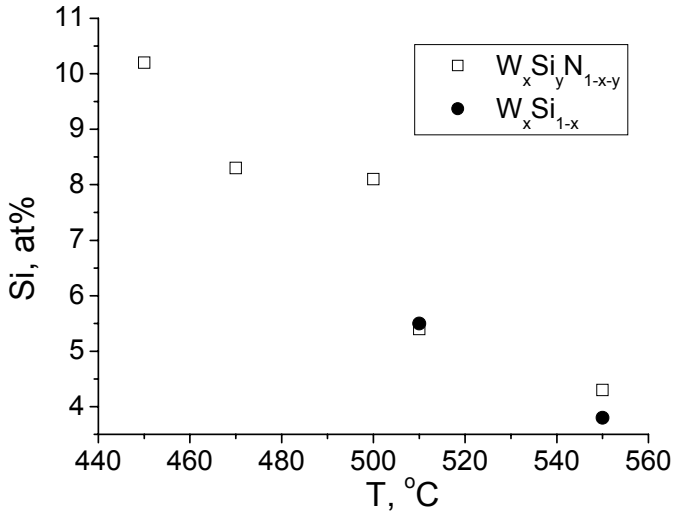

Figure 5-12. Si concentration in the Cu layer after the test versus temperature of considerable rise of resistance.

A combination of results of RBS with related resistance results is shown in Figure 5-13. It shows the resistivity for Cu-Si alloys as a function of Si, soluble in Cu. The resistivity of the alloys is linearly dependent on Si concentration with a coefficient about 2 μΩcm/at%. For comparison 3μΩcm/at% was reported by Murarka [10] and 5 μΩcm/at% by Schröder [17].

The results of RBS measurements show that Cu diffusion into barrier layers is much slower than the Si diffusion into Cu from $W_xSi_yN_{1-x-y}$ and W_xSi_{1-x} layers under vacuum at elevated temperature. The temperature of the reaction between Cu and barrier is determined by the Si/W ratio in the barrier material. The larger the Si/W ratio in a compound, the higher the reactivity of the compound with Cu and the Si diffusion out of the barrier starts at a lower temperature. Thus, barriers with the Si/W ratios in the range of 0.8-1.4 (with RBS) react with Cu at temperatures above 450 ^oC. This corresponds with the value of 0.6 reported by Reid [19]. A material with Si/W ratio of 0.8 is non-reactive with Cu up to 550 ^oC.

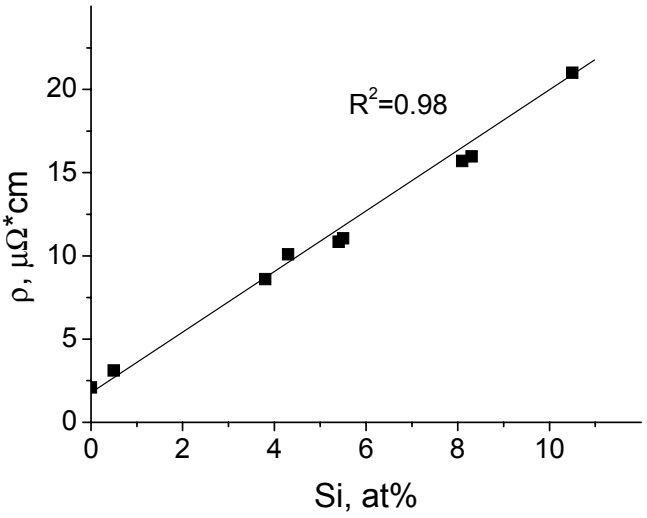

Figure 5-13. Resistivity of Cu-Si solutions at 25 °C. R^2 is the proportion of the variance in resistivity attributable to the variance in Si concentration.

The concentration coefficient of resistivity for Si in Cu is about 2 μΩ·cm for alloys with the Si concentration up to the solubility limit (~11.7 at%).

5.3.3 C-V measurements

C-V measurements were performed on capacitors with Cu and Cu/barrier contacts to SiO_2. Films of $W_{1.6}SiN_{0.2}$ and $W_2SiN_{0.1}$ with a thickness of 100, 70 nm were tested. Capacitors were measured before and after a heat treatment at 400 and 500 °C. Figure 5-14 shows results of C-V measurements for a Cu reference sample. C-V measurements for a sample with the Cu contact to SiO_2 showed no substantial changes after 400 °C temperature treatment, whereas after 500 °C the flatband voltage shifted to a negative voltage. This shift is due to the diffusion of Cu^+ ions into oxide [20, 21]. The shift of the flatband voltage does not give the reliable information about concentration of mobile ions or charges in SiO_2, because the exact distribution of ions or charges is not known. Therefore a failure of barriers could occur at T> 400 °C.

Typical C-V curves for capacitors with Cu/barrier contacts obtained in the test are shown in Figure 5-15. All samples after 400 °C heat treatment showed the positive shift in the flatband voltage. This shift can be due to anneal of positive charges [22] or introduction of negative charges in oxide. These charges could be a result of a plasma damage of oxide

during etching of barriers or some traps formed in oxide during barrier growth. A change of slope of C-V curve in a depletion indicates the anneal of interface states at the oxide/Si interface. The treatment at 500°C resulted in a smaller shift of flatband voltage than after 400 °C treatment. The slope of the C-V curve also has changed, showing a further anneal of the interface state in SiO_2/Si combination.

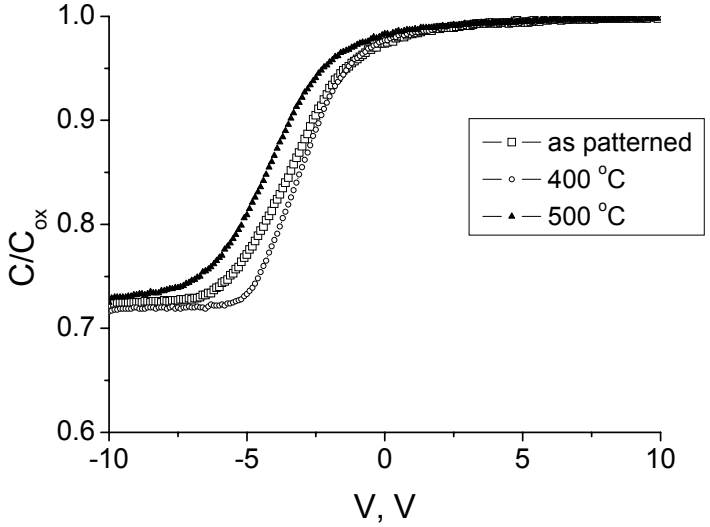

Figure 5-14. C-V plot for a capacitor with a Cu contact to SiO_2 as patterned, annealed at 400 °C and 500 °C.

A typical shift of flatband voltage by 0.45 V after 400 °C anneal is correlated to a little change of charges equivalent to $1.4 \cdot 10^{10}$ cm^{-2}. Thus, for thick 700 nm oxide even very small changes of oxide charge result in a measurable shift in flatband voltage.

After 550 °C temperature cycle the surface morphology of Cu/barrier/SiO_2 was changed due to poor adhesion of the barrier to SiO_2. Thus, the capacitors received the heat treatment at 550 °C were not measured.

C-V measurements do not reveal a flatband voltage shift ascribed to Cu^+ ions diffused into SiO_2 after the treatment at 400 °C. Some traps, introduced during the plasma etching of barriers or the barrier processing, can be annealed at 400 °C. The $W_xSi_yN_{1-x-y}$ film showed good diffusion properties at least up to 500 °C. As an alternative and complement to C-V

measurements the TVS method was applied to measure mobile charges in the oxide at 250 °C after a stress in an electrical field for 5 min at +1MV/cm.

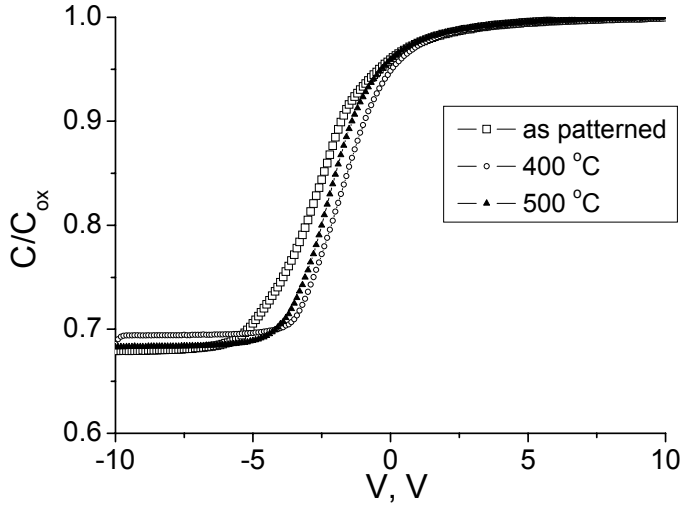

Figure 5-15. Typical C-V plot for a capacitor with a Cu/$W_{1.6}SiN_{0.2}$ contact as patterned, annealed at 400°C and 500°C. The thickness of the barrier was 70 nm.

A large current increase correlated to up to $2 \cdot 10^{12}$ cm^{-2} was measured with TVS in a bias range, which could not be ascribed neither to a Cu^+ ions drift nor to Na^+ ions, which are always present at low concentrations as contaminations. After the 400 and 500 °C annealing the unexpected current peak has been decreased by a factor of 10. This effect we also observed during a study of ALD grown tungsten nitrides. A discussion on this subject will be presented in Chapter 6*, 6.5.3.2. Capacitors, B. TVS*.

5.4 Summary

The CVD process of the growth of $W_xSi_yN_{1-x-y}$ films has been studied using WF_6, SiH_4 and NF_3. This process is characterized with a deposition rate of 35-70 nm/min. This is substantially higher than required for barrier application. N incorporation into a growing film occurs at 385 °C. No formation of W-N bond has been observed at 250 °C.

The limiting step of the growth is the diffusion of precursors to the growing surface. A change of total flow influences the film composition.

The process of growth of N-poor and N-rich compounds is limited to a range of 4-5 of SiH_4/WF_6 flow ratio at a fixed NF_3/WF_6 ratio of 1. The amount of N in films changes abruptly from 40 at% down to 5 at% with increase of SiH_4/WF_6 ratio from 5 to 6. The increase of NF_3 fraction at large flow ratio of SiH_4/WF_6 changes the growth mechanism from non-selective to selective, but has no influence on the N content in films. This makes it impossible to tune fine the composition.

The resistivity of the N-rich compounds is 1500-3000 $\mu\Omega$·cm, which is unacceptably high. A resistivity of Si-rich compound was in the range of 550-890 $\mu\Omega$·cm.

$W_xSi_yN_{1-x-y}$ films were characterised with an RMS roughness of 2.9-5.9 nm for films with a thickness of 70 nm.

The reactivity of the Si-rich compounds with Cu was tested with four-point probe in situ sheet resistance measurements up to 690 ^oC in vacuum. Barriers with a Si/W ratio ≥ 0.8 have shown a Si diffusion out of the barriers into Cu metallisation and a large increase of Cu-resistivity. Thus, these materials failed the criterion of low reactivity with Cu.

C-V test did not show the evidence of barrier failure. The capacitance measurements on a thick SiO_2 film demonstrated a high sensitivity of the flatband voltage to small changes of oxide charges.

References

1. Y. G. Shen, Y. W. Mai, W. E. McBride, Q. C. Zhang, D. R. McKenzie, Structural properties and nitrogen-loss characteristics in sputtered tungsten nitride films, *Thin Solid Films*, 372, p. 257-264 (2000).
2. B.S. Suh, Y.J. Lee, J.S. Hwang and C.O. Park et al., Properties of reactively sputtered WNx as Cu diffusion barrier, *Thin Solid Films*, 348, p. 299-303 (1999).
3. J. S. Reid, E. Kolawa, R.P. Ruiz and M.- A. Nicolet, Evaluation of amorphous (Mo, Ta, W)-Si-N diffusion barriers for <Si>/Cu metallization, *Thin Solid Films*, 236, p. 319-324 (1993).
4. CRC Handbook of Chemistry and Physics, Vol. 76, 1995, ISSN 0147-6262.
5. J. G. Fleming, E. Roherty-Osmun, P. M. Smith, J. S. Custer, Y.- D. Kim, T. Kacsich, M.- A. Nikolet, C. J. Galewski, Growth and properties of

diffusion barriers deposited by chemical vapor deposition, *Thin Solid Films*, 320, p.10-14 (1998).

6. T. Nakajiama,K. Watanabe and N. Watanabe, Preparation of Tungsten Nitride Film by CVD Method Using WF_6, *J. Electrochem. Soc*., 134(12), p. 3175-3178 (1987).
7. E. Blanquet, A. M. Dutron, V. Ghetta, C. Bernard, R. Madar, Evaluation of LPCVD Me-Si-N (Me=Ta, Ti, W, Re) diffusion barriers for Cu metallizations, *Microelectronic Engineering*,37/38, p. 189-195 (1997).
8. A. M. Dutron, E. Blanquet, V. Ghetta, R. Madar and C. Bernard, Morphology and Thermal Stability of Me- Si- N (Me=Re, W, Ta) for Microelectronics, *Journal De Physique* 1v, vol. 5, p. c5-1141-1148 (1995).
9. R. Somatri-Bouamrane, N. Chevarier, A. Chevarier, A. M. Dutron, E. Blanquet and R. Madar, Ion beam analysis of ternary silicides Me-Si-N (Me= Re,Ta, Ti, W) thin films used as diffusion barriers in advanced metallization, *Proceedings of the Fourteenth International Conference and EUROCVD-11*, *Electrochemical Society Proceedings* Vol. 97-25, p. 741-748 (1997).
10. S. P. Murarka, Advanced materials for future interconnections of the future need and strategy (Invited lecture), *Microelectronic Engineering* 37/38, p. 29-37 (1997).
11. J. E. J. Schmitz, M.J. Buiting and R.C. Ellwanger, Study of the SiH_4- WF_6 chemistry used in selective W deposition, *Material Research Soc*. 1989, ISBN 093 1837 987.
12. J. W. Klaus, S. J. Ferro, S. M. George, Atomic layer deposition of tungsten nitride films using sequential surface reactions, *J. Electrochem. Soc*., 147(3), p. 1175-1181 (2000).
13. J. Holleman, A. Hasper, C. R. Kleijn, Loading effects on kinetical and electrical aspects of silane-reduced low-pressure chemical vapor deposited selective tungsten, *J. Electrochem. Soc.*, v 140, n 3, p 818-825 (1993).
14. C. R. Kleijn, Transport phenomena in Chemical Vapor Deposition reactors, TU Delft, 1992, PhD. thesis, ISBN 90-9004669-0.
15. J. L. Alay, H. Bender, G. Brijs, A. Demesmaeker and W. Vandervorst, Quantative Analysis of W(N), TiW and TiW(N) Matrices using XPS, AES, RBS, EPMA and XRD, *Surface and Interface Analysis*, Vol. 17, p. 373-372 (1991).
16. O. H. Gorkce, S. Amin, N. M. Ravinda, D. J. Szostak, R. J. Paff, J. G. Fleming, C. J. Galewski, J. Shallenberger, R. Eby, Effects of annealing on X-ray-amorphous CVD W-Si-N barrier layer materials, *Thin Solid Films*, 353, p. 149-156 (1999).
17. Klaus Schröder, Handbook of electrical resistivities of binary metallic alloys, ISBN 0-8493-3520-5.

18. S. Arrhenius and A. Wesgren, *Z. physik. Chem*., B14, p. 66-79 (1931).
19. J. S. Reid, E. Kolawa, and M.-A. Nicolet, Thermodynamics of (Cr, Mo, Nb, Ta, V, or W)-Si-Cu ternary systems, *Journal of Materials Research*, v 7, n 9, p. 2424-2427 (1992).
20. S. A. Cohen, J. Liu, L. Gignac, T. Ivers, D. Armbrust, K. P. Rodbell and S. M. Gates, Characterization of thin dielectric films as copper diffusion barriers using triangular voltage sweep, *Mat. Res. Soc. Symp. Proc*. Vol. 565, p. 189-196 (1999).
21. Alvin L. S. Loke, Kinetics of Copper Drift in Low-k Polymer Interlevel Dielectrics, *IEEE Transactions on Electron Devices*, Vol. 46, N.11, p. 2178-2186 (1999).
22. B. J. O' Sullivan, P. K. Hurley, F. N. Cubaynes, P.A. Stolk, F .P. Widdershoven, Flat band voltage shift and oxide properties after rapid thermal anneal, *Microelectronics reliability*, 41, p.1053-1056 (2001).

Chapter 6

Atomic Layer Deposition of W-based films

6.1 Introduction

Diffusion barrier films are used in interconnects with Cu metallisation. The International Technology Roadmap for Semiconductors (ITRS) requires manufacturing of barrier layers against Cu diffusion scaled down to 5 nm in 2010. Among other requirements, such a thin layer must possess a low roughness and be conformal over small features with a high aspect ratio. Advanced ionized Physical Vapour Deposition (iPVD) cannot compete with the excellent step coverage and low roughness of films grown with Atomic Layer Deposition (ALD). The principle of ALD is a repeating-, sequential- and preferably saturated adsorption of reactive species at the surface, resulting in film growth [1].

Tungsten nitride layers are promising barriers against Cu diffusion [2, 3]. Chemical Vapor Deposition (CVD) of tungsten nitrides using WF_6 and NH_3 is known to suffer from an adduct $WF_6 \cdot 4NH_3$ [4]. ALD separates the reactants using a sequential pulsing. This eliminates the formation of the by-product. Successful deposition of tungsten nitride using ALD was reported by Klaus [5] and Elers [6]. A repeating cycle with WF_6 and NH_3 was used. The obtained layers are characterized, however, with a resistivity of 4500 μΩcm, which is unacceptably high for barrier application. In contrast, the resistivity of ALD-tungsten carbonitride films was reported to be 600-900 μΩcm for 7 nm films [7] and 350-400 μΩcm for 25 nm films [8]. This low resistivity makes tungsten carbonitrides also a promising diffusion barrier. The $W_xC_yN_{1-x-y}$ layers were grown with a cycling of WF_6, NH_3 and TEB (triethyl borane).

We studied the deposition of $W_xC_yN_{1-x-y}$ layers with the same sequence of the precursors. Also we tried ethene, C_2H_4, as a cheap and safe carbon precursor instead of TEB and we used SiH_4 as an additional reducing agent. The process of the growth was conducted with a cycling of WF_6, NH_3, SiH_4 and C_2H_4 gases. However, in contrast to thermodynamic predictions (See chapter 3) no carbon was found in the layers grown. The

obtained films were tungsten nitrides. The layers are characterized with a resistivity of about 480 μΩcm for layers thicker than 13 nm. This resistivity is much lower than the reported values. Detailed discussion about pulse sequences and film growth is presented in Section 6.3.2 Results.

The physical requirements to a barrier material include mainly low reactivity with Cu, low resistivity and good diffusion barrier properties (see Chapter 1, 1.2). The reactivity of the barrier material with Cu is tested by *in situ* four-point probe measurements during heat treatment. The diffusion barrier properties are evaluated after annealing treatments by testing diodes and capacitors. The results of these measurements showed that the obtained tungsten nitride and tungsten carbonitride films have a low reactivity with Cu and good blocking properties against both Cu and Al diffusion.

6.2 Deposition equipment

The ALD system we used is schematically presented in Figure 6-1 and 2. It consists of a loadlock for wafer transfer, an outer chamber and a small hot-wall reactor inner chamber. The outer chamber with a base pressure of 10^{-7}mbar is purged with N_2 during the process at the same pressure as the operating pressure of the inner chamber. The system is pumped with an oil-free turbo-pump with a capacity of 400 l/s. This turbo-pump is backed by a dry pump.

The wafer is placed in the loadlock on a molybdenum susceptor and after pump-down transferred into the chamber by an automated arm and placed on the hot chuck. The chuck goes up and forms the bottom of the hot-wall reactor, creating an enclosed space with a volume of about 24 ml. The upper part consists of the gas-block covered with the top heater and a thermoscreen, which protects the outer reactor against heat dissipation, see Figure 6-2. Gas reactants enter the hot-wall reactor via gas distribution channels, see Figure 6-3.

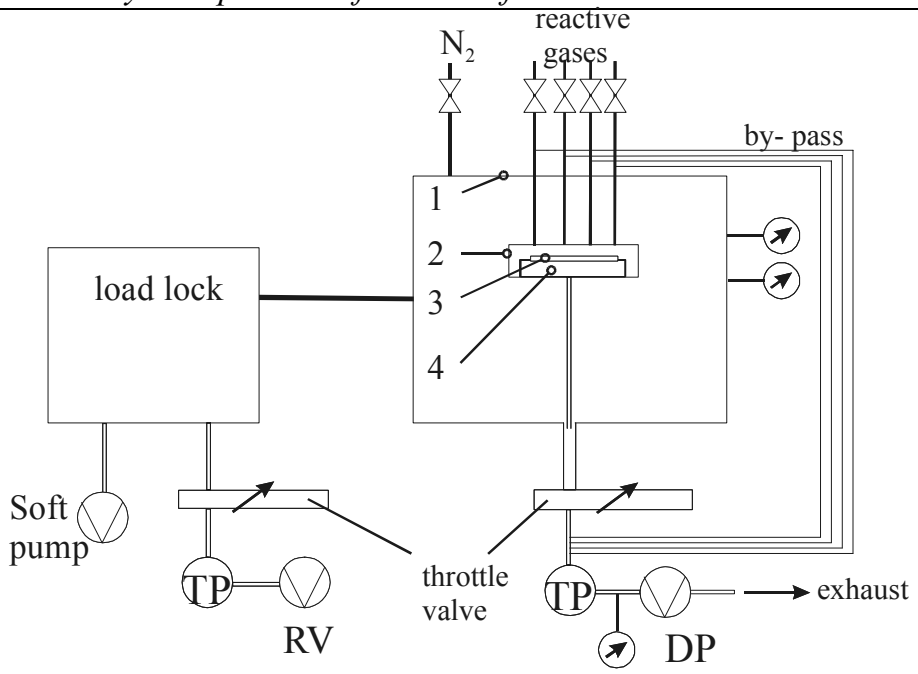

Figure 6-1.The principal scheme of the ALD-system for barrier deposition:

1. *outer chamber;*
2. *upper part of the hot-wall reactor;*
3. *volume of the hot-wall reactor;*
4. *hot chuck with susceptor and wafer;*

TP: turbo pump;
RV: rotary-vane pump;
DP: dry pump.

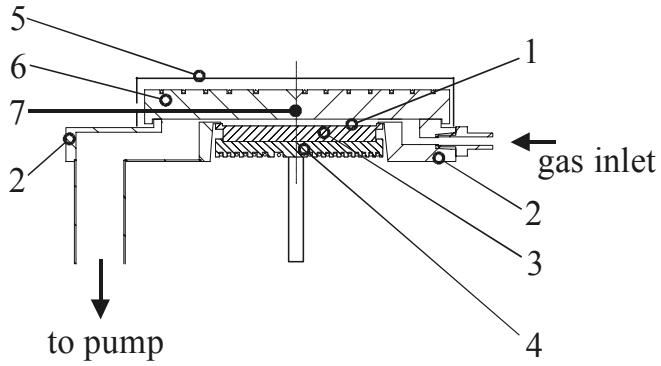

Figure 6-2. Schematic picture of the hot-wall reactor:

1. *closed volume of the hot-wall reactor;*
2. *gas block;*
3. *suceptor;*
4. *hot chuck;*
5. *thermoscreen against heat dissipation;*
6. *top heater;*
7. *thermocouple.*

During the deposition a constant flow of 80 sccm N_2 is flowing through the reactor at a total pressure of 0.75 Torr. The reactant gases were set to 5 sccm via mass flow controllers and are directed into the pump via a by-pass system. Sequentially the reactive gases are switched to the reactor chamber during typically 1-3 seconds. There they mix with the N_2. When the precursor gases are switched to the by-pass a nitrogen upstream-flow in the precursor line blocks any leaks of the precursor valve and outdiffusion of precursor from dead-end parts in the precursor gas line. In between each pulse of reactive gas the N_2 purged the reactor for 2 seconds. The typical exposure time to reactive gases is 1 sec at 0.75 Torr, which is equivalent to $4.7 \cdot 10^4$ L (Langmuir, $1L=10^{-6}$ Torr·sec). The temperature is regulated by a PID (Proportional-Integral-Derivative) controller via a thermocouple inserted in the top heater. The process temperatures we investigated are 325 and 350 ºC. Temperatures higher than 400 ^oC are unacceptable for the back-end processing and at T<325 ^oC incorporation of nitrogen becomes lower [5].

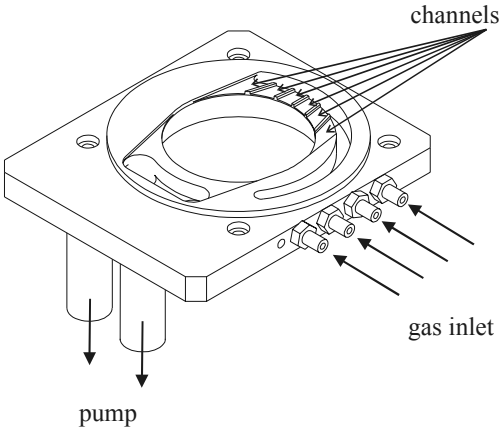

Figure 6-3. Gas block without heaters.

6.3 Process study

6.3.1 Experimental procedure

6.3.1.1 Growth of W_xN_{1-x}

Surface preparation

Si (100) n-type 100 mm substrates (1-10 Ωcm) with 700 nm of wet thermally grown SiO_2 were used. Wafers were cleaned with fuming HNO_3 and boiled in 69% HNO_3. Each wafer was dipped in 0.3% HF for

3 minutes and rinsed in DI before deposition. This procedure was reported to provide a surface on which dense Si-films could grow [9]. The spin-dried wafer was loaded into the reactor.

Nucleation step

After the process temperature was reached, a Si film was grown via the decomposition of Si_2H_6 to create reactive sites for the chemisorption of WF_6. The conditions of the nucleation were altered by varying the exposure to Si_2H_6 (see Table 6-1). The decomposition was carried out at 7.5 Torr. The experiments at both temperatures are divided into two groups: with a thick nucleation layer and a thin one. The thick film was made at $4.5 \cdot 10^9$ L at both temperatures. To grow the thin layer with approximately the same thickness at both temperatures, the Si_2H_6 exposures were adapted to $8.1 \cdot 10^8$ L and $2.0 \cdot 10^9$ L at 350 and 325 ^oC, respectively.

Table 6-1. Nucleation conditions.

	T, ^oC		Si_2H_6 exposure, L	thickness by ellipsometer, nm	thickness by XPS**, nm
*	350 ^oC	7.5 Torr 10min	4.5e9	8-10	
*	325 ^oC	7.5 Torr 5 min	2.0e9	1.2	
*	350 ^oC	7.5 Torr 2 min	8.1e8	1.5	
	350 ^oC	7.5 Torr 20min	8.1e9		12
	325 ^oC	7.5 Torr 20min	8.1e9		5

**. These nucleation conditions are used for a detailed study of the process.*
***. Thickness was calculated using standard sputter rates.*

Film growth

After the Si-nucleation step the reactor was pumped down from 7.5 to 0.75 Torr under Si_2H_6 atmosphere. A cycling sequence of $WF_6/NH_3/C_2H_4/SiH_4/NH_3$ was applied to deposit W_xN_{1-x} films after a purging pulse of N_2. Deposition conditions noted as e.g. 1/2/3/2/2 refer to the reactant pulse lengths in seconds: 1 s for the WF_6 pulse, 2 s for NH_3, 3s

for C_2H_4, 2 s for SiH_4 and 2 s for NH_3 with a 2 s purge of pure N_2 between each reactive gas pulse. The variable parameters were temperature, pulse time, number of cycles. The cycle time was 14-22 s.

The deposition process was always ended with a SiH_4 pulse in order to obtain a thin layer of Si, meant to protect the barrier against oxidation during unloading the wafer towards atmosphere. This top Si layer will be oxidized. Thus, a very thin SiO_2 is always present on top of the $W_{1-x}N_x$ films, which was confirmed by XPS measurements.

6.3.1.2 Growth of $W_xC_yN_{1-x-y}$

Surface preparation

The wafers were prepared in the same way as described for the growth of W_xN_{1-x} with a variation of the final dip-etch. A solution of 0.3 % HF or 0.3% HF: isopropanol (65:1) was used in this case.

Nucleation step

A nucleation step with exposure to TEB was applied before the growth sequence. The TEB exposure was equal to $0.9 \cdot 10^6$ and $2 \cdot 10^7$ L.

Film growth

The growth of $W_xC_yN_{1-x-y}$ layers was performed at 325 ^oC using a repeating pulse sequence with triethyle borane ($B(C_2H_5)_3$, TEB), WF_6 and NH_3. The temperature window for this ALD process is 300-350 ^oC [8]. Pulse times of TEB, WF_6 and NH_3 were 3 s, 3 s and 4 s, respectively. The gas flows of WF_6 and NH_3 were 5 sccm. The TEB flow was 5 sccm, 6 sccm or 7 sccm for the different experiments.

6.3.1.3 Compositional- and structural analysis

The composition of the deposited films was measured by XPS (X-Ray Photoelectron Spectroscopy) and RBS (Rutherford Backscattering Spectroscopy). XPS profiles were obtained by sputtering with a 1 kV Ar^+ ion beam with a cross section area of 3x3 mm^2. Standard sensitivity factors were used to calculate concentrations. RBS was done with 2 MeV He^+ ions on an area of 1 mm^2. The hydrogen content in the films was determined

with ERD (Elastic Recoil Detection). Surface roughness was measured with AFM (Atomic Force Microscopy). X-ray diffraction was applied to determine the crystalline structure of the barrier films.

6.3.1.4 Sheet resistance

The sheet resistance of the barrier films grown on wafers with thermal SiO_2 of 700 nm thick was measured with four-point probe method.

6.3.2 Results

6.3.2.1 Tungsten nitrides

Growth process

After a Si nucleation layer has been formed, each growth process starts with a pulse of WF_6. Here the Si nucleation layer reacts with WF_6 as
$3\ Si + 2\ WF_6 = 2\ W + 3\ SiF_4$.
The formed W film or nuclei modify the roughness. For instance, a thick Si nucleation film with an RMS roughness of 0.25 nm transforms into a W film with a roughness of 1.2 nm. The W nuclei serve as adsorption sites for the further deposition. Therefore, in this case, the starting roughness for the growing tungsten nitride film is about 1.2 nm.

Choice of the pulse sequence

Different sequences of the WF_6, NH_3, C_2H_4 and SiH_4 pulses were studied. The compositions of layers as determined with XPS, RBS, RMS-roughness, sheet resistance (R) and the layer thickness for different sequences after 100 cycles are presented in Table 6-2.

A pulse sequence of $WF_6/C_2H_4/NH_3$ (see №1 in Table 6-2) resulted in a roughness of 1.2 nm. This film and roughness is related to the reaction of WF_6 with the thick Si nucleation layer. No further growth was observed. A plausible explanation for the stopping of the growth is deactivation or poisoning of the W surface with C_2H_4, which decomposes into CH_2^* on the W surface [10].

A pulse sequence of $WF_6/NH_3/C_2H_4$ produced a 5 nm film with an RMS roughness of 2.79 nm (see №2 in Table 6-2). Thus, the layer is hardly continuous. This suggests that only a few reactive sites were available for

the reduction of WF_6. To facilitate the formation of new reactive sites an extra SiH_4 pulse was applied.

Table 6-2. Films properties for different pulse sequences after 100 cycles at 350 ^oC.

№	Nucle-ation exposure to Si_2H_6, L	Pulse sequence	Composition by RBS	Composition by XPS	RMS nm*	thick ness, nm **	R, Ω/sq
1	4.5e9	$WF_6/C_2H_4/NH_3$			1.20	1.4	
2	4.5e9	$WF_6/NH_3/C_2H_4$			2.79	5	2970
3	4.5e9	$WF_6/NH_3/C_2H_4$ / SiH_4	$W_{0.7}N_{0.3}$	$W_{0.84}N_{0.16}$	4.19	26	71
4	4.5e9	$WF_6/NH_3/C_2H_4$ / SiH_4/ NH_3	$W_{0.69}N_{0.31}$	$W_{0.83}N_{0.17}$	1.32	26	91
5	8.1e8	$WF_6/NH_3/C_2H_4$ / SiH_4/ NH_3	$W_{0.59}N_{0.41}$	$W_{0.80}N_{0.20}$	0.70	23	171
6	4.5e9	$WF_6/C_2H_4/SiH_4$ /NH_3	$W_{0.71}N_{0.24}Si_{0.05}$	$W_{0.9}N_{0.05}Si_{0.05}$	1.76	28	66
7	8.1e8	$WF_6/NH_3/SiH_4$/ NH_3	$W_{0.5}N_{0.45}Si_{0.05}$	$W_{0.75}N_{0.2}Si_{0.05}$	0.67	20	178

**. For a comparison of roughness, the nucleation conditions should be taken into account.*
***. Thickness was calculated using the weight of the film and a standard density of W_2N, 17.8 g/cm^3.*

A sequence of $WF_6/NH_3/C_2H_4/SiH_4$ resulted in a growth of continuous tungsten nitride films (see №3 in Table 6-2). No carbon is incorporated in the growing films, despite the C_2H_4 pulse. The Si and F content are at the detection limit of RBS and XPS (<0.5 at%). The film roughness of 4.2 nm (for 26 nm film) is higher than the roughness of the Si- nucleation layer initially (1.2 nm). This roughening is caused by a direct interaction of SiH_{4-x} adsorbed species with WF_6 in the used pulse sequence. Using a sequence of $WF_6/NH_3/C_2H_4/SiH_4/NH_3$, in which the SiH_4 and WF_6 pulses are separated by ammonia, the roughness decreased down to the base value of 1.32 nm (compare №3 with 4 in Table 6-2). No change of composition was observed. Even a lower RMS roughness of 0.7 nm is obtained, when we use a thin nucleation layer (see №5 in Table 6-2). It is well known that the thinner the W layer, growing at the cost of Si, the lower the roughness.

Thus, the less Si is available to be consumed, the thinner the formed W film is and the lower its roughness. The resistivity of the layers, calculated as thickness multiplied by sheet resistance, is ~400 μΩ·cm (see №5 in Table 6-2). For more accurate calculations see Section: 6.4 Film resistance p. 126). This value is about 10 times lower than reported by Elers et al. for their ALD tungsten nitrides grown with WF_6 and NH_3 [6]. In those films the amount of the residual F was 2.4 at%. Thus, the C_2H_4 and SiH_4, introduced in our growth sequence, strip off the F during the growth. This might explain why the resistivity of these layers is so much lower.

The films deposited with a sequence of $WF_6/(NH_3=0)/C_2H_4/SiH_4/NH_3$ contained about 5 at% Si and had a very low N- concentration (see №6 in Table 6-2). In the application as a diffusion barrier for Cu metallisation Si can diffuse out of the layer into the Cu, causing a rise of resistance. A 0.5 at% of Si in Cu causes a rise of 1 μΩ·cm [11].

Tungsten nitride, deposited with a cycling sequence without ethene $WF_6/NH_3/(C_2H_4=0)$ SiH_4/NH_3, also contains 5 at % Si (see №7 in Table 6-2).

The explanation for all these differences in composition lie in the reactivity of the W surface terminated by -F with the different precursors. The W-F bond is very reactive with both NH_3, SiH_4 and, probably, with C_2H_4. When NH_3 is offered as a first step after the WF_6 pulse, many sites will be covered with NH_x radicals. The subsequent offering of C_2H_4 and SiH_4 pulses will, probably, not push the W-NH_x bonds out of their position. The C_2H_4 adsorbing as CH_2 on this surface will further occupy sites, which are then no longer accessible to SiH_4 chemisorption. So it can be understood that the sequence $WF_6/NH_3/C_2H_4/SiH_4/NH_3$ has the highest N content and lowest Si content. The sequence $WF_6/NH_3/SiH_4/NH_3$ will have a high amounts of N as well, but also the Si in these films will be higher. This is because all sites available to C_2H_4 and SiH_4 in the previous sequence are now available to SiH_4 only. Finally, in the sequence of $WF_6/C_2H_4/SiH_4/NH_3$ most of the available sites will be occupied by CH_2 and SiH_x and very few to NH_3.

Taking into consideration the composition of the films and the roughness, the sequence of $WF_6/NH_3/C_2H_4/SiH_4/NH_3$ was chosen for further study with the nucleation exposure to SiH_4 of $8.1 \cdot 10^8$ L and $2.0 \cdot 10^9$ L at 350 and 325 ^oC, respectively.

Results of growth study

A study of the growth rate was done using the results of weight measurements and RBS data on the amount of W in the films.

The weight increase of the grown films versus number of cycles is presented in Figure 6-4 a) and b) for 325 and 350 ^oC, respectively. The films were grown with the sequence of $WF_6/NH_3/C_2H_4/SiH_4/NH_3$. The slope of the (weight-number of cycles) line represents the deposition rate. In Figure 6-4 a) it is shown that the deposition rate is the same for different nucleation conditions, (filled and empty circles). The lines, however, have a different offset, which is related to the W formed initially during the reaction of WF_6 with the silicon nucleation layer. The increase of the WF_6 exposure to 2 s leads to a rise of 9% of the deposition rate (triangles in Figure 6-4 a). It approaches about 1 monolayer of W_2N per cycle. It is assumed that only W atoms contribute to the weight change. The growth rate at 350 ^oC is presented in Figure 6-4 b). The deposition rate reaches about 1 monolayer per cycle even for the WF_6 exposure with the pulse of 1s. With a 3 times longer WF_6 pulse the growth rate becomes about 30% higher, (triangles in Figure 6-4 b). The growth rate is not affected by the nucleation conditions, (filled and empty circles). Moreover, it stays the same for the different C_2H_4 pulse, (empty circles and squares). Thus, the growth rate increases slightly with higher temperature and longer WF_6 exposure. A calculated deposition rate is in the region of one monolayer per cycle. In addition to the relatively inaccurate weight measurements the amount of W was measured with RBS.

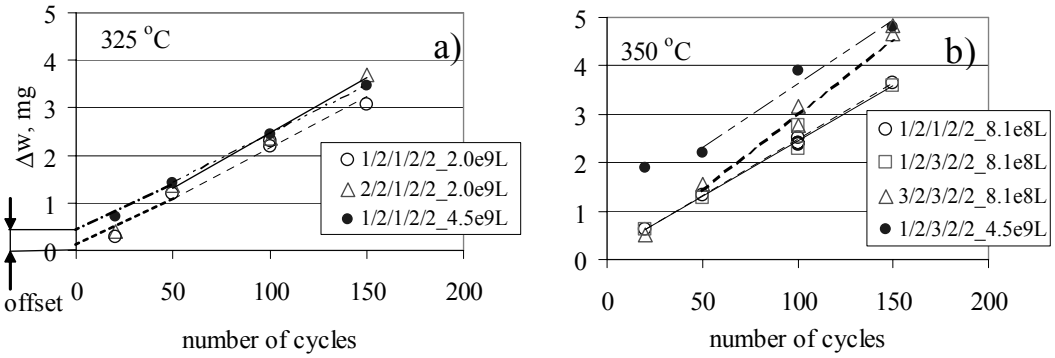

Figure 6-4. Weight dependence of the W_xN_{x-1} films versus number of cycles a) at 325 °C; b) 350 °C. In the legend there are pulse time lengths, s, in the pulse sequence of $WF_6/NH_3/C_2H_4/SiH_4/NH_3$. The last figure in the line indicates the exposure to Si_2H_6, L, in order to form the nucleation layer.

In Table 6-3 the amount of W for a series of samples is presented. The accuracy of the data is 5-10 % W. The data demonstrate the tendency of an increase of the amount of W with a two times longer WF_6 pulse. It shows an increase of the deposition rate of 7%, (see №1, 2 in Table 6-3). At 350 °C the growth rate is 15 % higher for the same pulse time as compared to 325 °C, (see №1, 3 in Table 6-3). The increase of the WF_6 exposure by 3 or 4 times leads to the slight increase of 5-9 % of the growth rate, (see №4, 5, 6). The calculated deposition rate is close to one monolayer of W_2N per cycle at 350 °C.

Table 6-3. The amount of W measured with RBS in films obtained after 100 cycles.

№	T, °C	sequence	W, x10^{15} at/cm^2
1	325	1 / 2/ 1/ 2/ 2	78
2		2 / 2/ 1/ 2/ 2	85
3	350	1 / 2/ 1/ 2/ 2	93
4		1 / 2/ 3/ 2/ 2	97
5		3 / 2/ 3/ 2/ 2	102
6		4/ 2/ 3/ 2/ 2	106

There is often a difference between the results of the weight measurements and RBS data. The reason is that the measured weight is the total amount of material deposited on a whole wafer. For calculation of the growth rate

from weight increase one should realize there is growth on the backside of the wafer and non-uniformity of the deposited film on the front side. Thus, weight data indicate the trend only. RBS analysis was performed on the same area and for identical positions for each measured wafer. In this case, the test results are not interfered by the deposition on the backside. The influence of the non-uniformity is minimized. The actual growth rate is to be calculated with RBS data.

In Figure 6-5 the amount of W and N is plotted versus number of cycles. These are used for an accurate calculation of the deposition rate at 350 ^{o}C. The slopes of the W lines are the same for the short and long WF_6 pulse, resulting in a deposition rate of $1{\cdot}10^{15}$ W at/cm^2 per cycle, (triangles and circles). The shift between the W lines is attributed to a difference in the W formed initially due to different initial Si nucleation layers. The N-content is shown as diamonds in Figure 6-5. This determines the film stoichiometry. It will be discussed in the following *Section: Composition of films*.

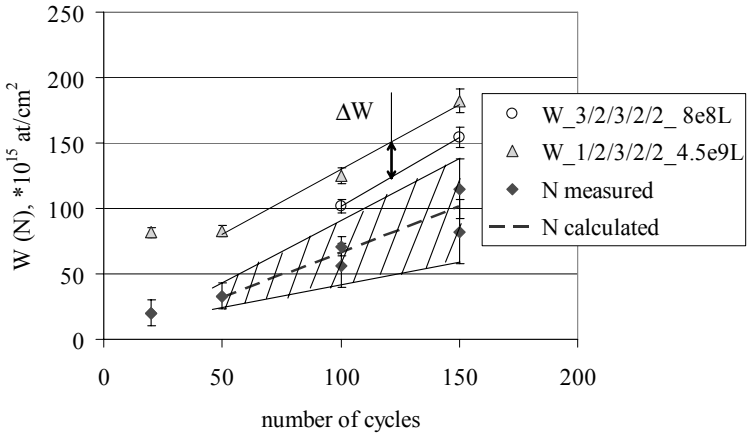

Figure 6-5. The W and N amount in the W_xN_{1-x} film versus number of cycles. The film was deposited at 350 ^{o}C with a sequence of $WF_6/NH_3/C_2H_4/SiH_4/NH_3$. The lengths of reactive pulses and initial exposure to Si_2H_6 are in the legend.

Composition of films

The composition of layers obtained after 100 cycles with a varying pulse length was determined using XPS and RBS. Both analytical techniques demonstrate that our films are tungsten nitrides.

The accuracy of the amount of nitrogen determined from RBS spectra is between 10 and 30 % of the measured value. Consequently, the range of the amount of N in the films becomes very broad. This is indicated in Figure 6-5 with the shaded area. The inaccuracy comes from the nature of the RBS spectrum. A part of such an RBS spectrum is shown in Figure 6-6. A schematic drawing of the measured stack is presented. The dashed arrows demonstrate how the RBS signals are assigned to elements and their location in the depth of the sample. It can be seen that the N signal has the same channel number as the O and/or Si signals from the underlying SiO_2. As a result, the peak from N in the film is on the top of Si and O signals. This coincidence of peaks makes an accurate determination of the amount of N very difficult. The error in the calculated amount of N can be as high as 30 %. On the other hand, an accuracy of simulated values deteriorates also with less N amount. In this case, a ratio of the N signal to a sum of the Si and O signal degrades and the accuracy becomes worse. The N content in the obtained films was about 38-44 at% with RBS. The *average ratio of W to N content is 1.46± 0.13.* Given the W growth rate of $1 \cdot 10^{15}$ at/cm^2, the N growth rate is $(0.7 \pm 0.13) \cdot 10^{15}$ at/cm^2 per cycle. The calculated N amount in films is indicated in Figure 6-5 with the dashed line.

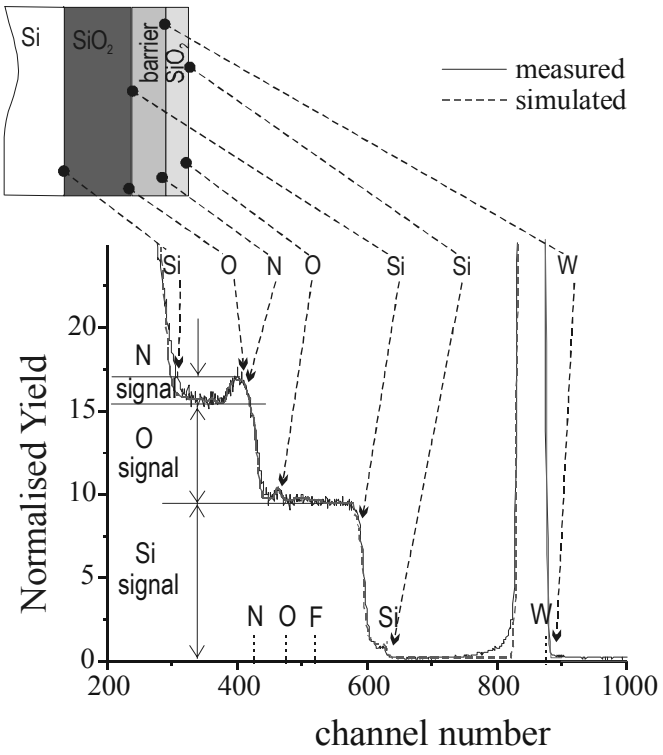

Figure 6-6. RBS spectrum for a tungsten nitride film grown on 700 nm SiO_2/Si substrate in 150 cycles. The black solid line is the measured signal. The dashed line is the simulation.

The hydrogen content in the films was lower than 1 % as measured with ERD.

An example of an XPS-depth profile is presented in Figure 6-7. The nitrogen content with XPS was taken from the plateau in the depth- profile, where the N and W content did not change anymore. The nitrogen concentration in this case is 15-21 at%. The depth profile of the samples showed a Si and an O peak at the surface. This corresponds to a very thin Si layer, which was on purposely grown on top of the ALD film and which oxidised later. *The average ratio of W to N with XPS is 4.4± 0.5.* This is substantially higher than the W to N ratio obtained from RBS data. The reason for that is preferential sputtering of nitrogen during depth profiling. This leads to a lower value of the N measured [12].

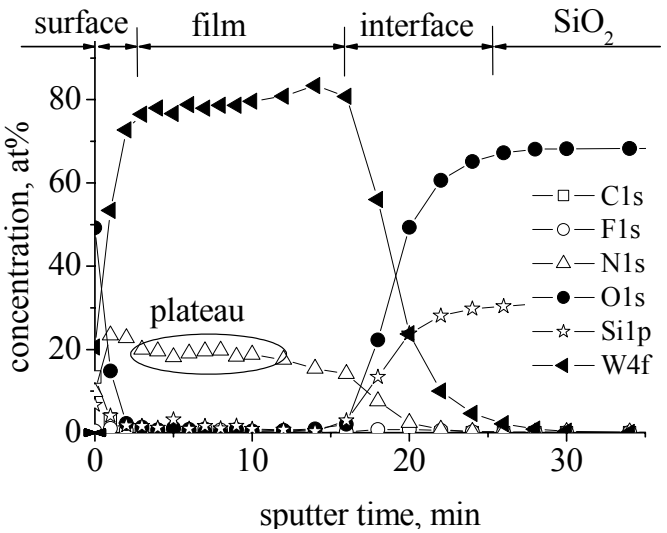

Figure 6-7. XPS depth profile for a film grown with a pulse sequence of 3/2/3/2/2 ($WF_6/NH_3/C_2H_4/SiH_4/NH_3$) at 350 °C for 100 cycles.

Results of XRD analysis

The results of XRD are presented in Figure 6-8 and Table 6-4. The films have been grown on a thick nucleation layer and covered with a 200 nm Cu film. Cu and Si (from the substrate) show several peaks, which could mask peaks in the region $2\theta > 43^{o}$. In the other part of the spectrum all samples show a peak at $2\theta \approx 40^{o}$. This one could belong to β-W or α-W phase formed at the cost of the Si nucleation layer. The peak at $2\theta \approx 36^{o}$ may be from the hexagonal δ-WN phase. The peak at $2\theta \approx 38^{o}$ may be from the cubic phases β-W_2N and β-$W_{40.9}N_{9.1}$.The top two curves belong to sequences with longer ethene exposure. They show broader peaks at $2\theta \approx 40^{o}$. Thus, larger exposure to C_2H_4 changes the apparent morphology of the deposited films.

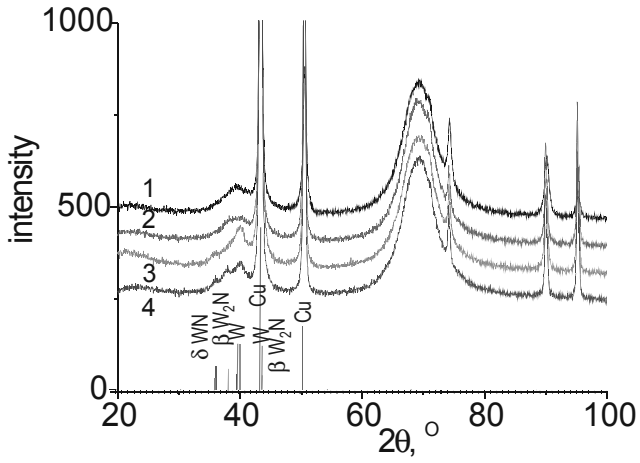

Figure 6-8. XRD θ-2θ spectrum for the stacks of Cu/$W_{1.5}N$ films.

Table 6-4. Summary of the XRD test of barriers.

№	WF_6/ NH_3/ C_2H_4/ SiH_4/NH_3	Peak by XRD
1	1/ 2/ 3/ 2/ 0	broad peaks for nitride and W phase
2	1/ 2/ 3/ 2/ 1	broad peaks for nitride and W phase
3	1/ 2/ 1/ 2/ 0	W phase, cubic W_xN_{1-x} very small and hexagonal WN
4	1/ 2/ 1/ 2/ 2	W phase, cubic W_xN_{1-x} and hexagonal WN

Films roughness

A film roughness as low as 0.43-0.76 nm was obtained for 16 nm $W_{1.5}N$ films using a low nucleation exposure to Si_2H_6.

6.3.2.2 Tungsten carbonitrides

For a deposition $W_xC_yN_{1-x-y}$ films a pulse sequence of WF_6/NH_3/TEB with N_2 purge was applied. Factors such as a surface cleaning, nucleation step and an exposure to TEB influence the growth process. Their effects on the film growth were studied.

Surface cleaning and TEB pulse

Tungsten carbide nitride films were grown on wafers, which received different etch-treatment before deposition: dipped in 0.3% HF solution or in 0.3% HF: isopropanol (65:1) solution. The standard deviation in % (STDV) of the sheet resistance and the sheet-resistance R of layers deposited with a different TEB flow is shown in Figure 6-9. The STDV, being an estimate of the film homogeneity, is lower for the films grown on wafers exposed to the solution with isopropanol. This is the reason why this solution was used for a growth of tungsten carbonitrides films.

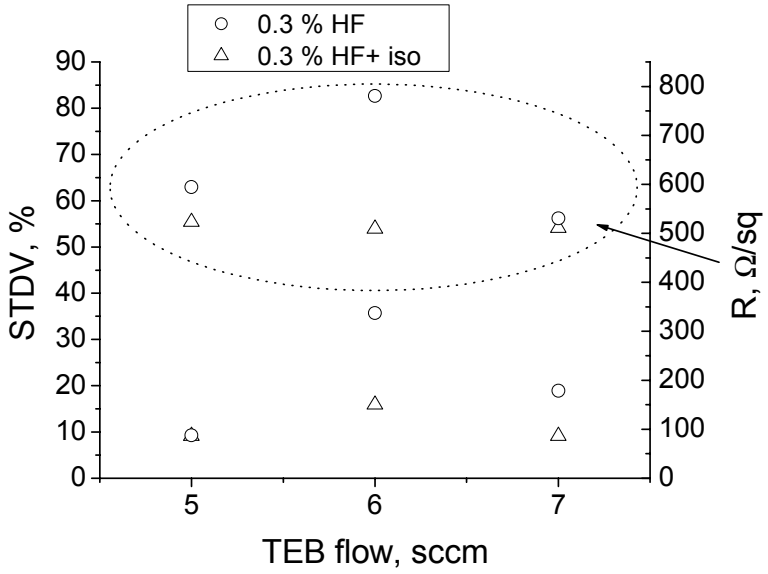

*Figure 6-9. STDV of sheet resistance (in %) and sheet resistance of the grown films with different flow of TEB. Thickness of deposited films is ~11 nm. (The thickness was calculated based on weight increase after the process and a density of 15.37 mg/cm^3 as reported by Kim [13].) Experiments are performed with an initial exposure to TEB of 9*10^6 L.*

The thickness of films grown with pulses of different TEB flows of 5, 6 and 7 sccm was about 10 nm for all flows, indicating that saturation conditions for ALD were reached. For the further study the TEB flow was set to 7 sccm.

Nucleation step

Figure 6-10 presents the weight of films versus number of cycles for different initial TEB exposure. When no nucleation step is applied, the

growth process is not reproducible (filled diamonds in Figure 6-10). The weight- growth dependence is approximated with a straight line for the films deposited after the nucleation step. For both nucleation exposures tried (of $9 \cdot 10^6$ and $2 \cdot 10^7$ L) these lines are parallel and the calculated growth rate corresponds to 1.3 Å/cycle. The shift of the line to the left for the larger TEB exposure indicates the decrease of the incubation time.

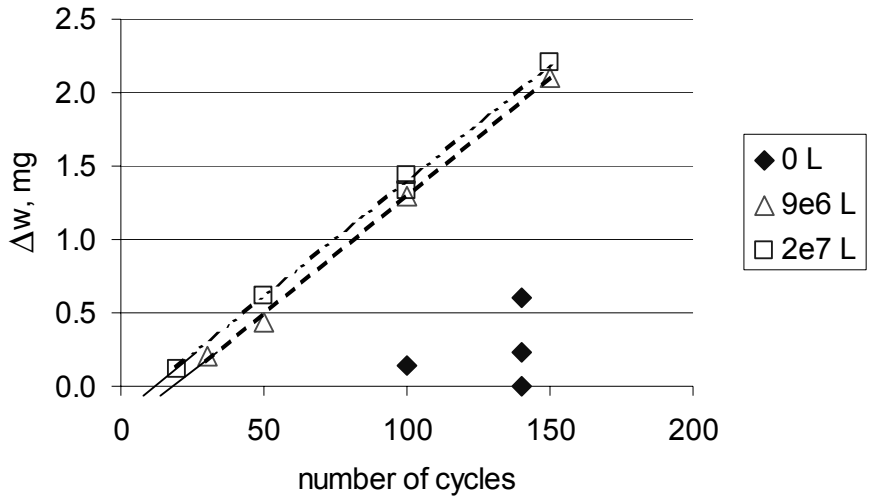

Figure 6-10. Weight change versus number of cycles for films grown at 325 ^oC with a pulse sequence of TEB/WF_6/NH_3. In the legend the nucleation exposure to TEB is shown.

Composition of films

The composition of the films was $W_{0.45}C_{0.29}N_{0.26}$ as determined with RBS. The composition with XPS was $W_{0.64}C_{0.25}N_{0.11}$. These values correspond well to the composition of similar films by Kim [13], who found $W_{0.48}C_{0.32}N_{0.20}$ with RBS, and by Li [8]: $W_{0.55}C_{0.30}N_{0.15}$ with XPS. The F-content in the films was at the detection limit.

Films roughness

The roughness of the 10 nm layers was 0.33 nm.

6.4 Film resistance

The sheet resistance (Ω/sq) was measured with the four-point probe method.

6.4.1 Tungsten nitrides

Figure 6-11 shows the resistance versus the amount of W in the films grown at 350 ^{o}C using different pulse times. The standard deviation of the resistance is marked with error bars. The resistance is decreasing proportional to the amount of W in the films. Using the amount of tungsten, related to the weight increase and multiplied by the measured sheet resistance, a measure for resistivity can be obtained. In Figure 6-12 the product, W·R, of the amount of W atoms and the resistance (R) is shown as a function of the number of cycles (the film thickness). The factor for resistivity approaches a constant value for films obtained in more than 50 cycles. Obviously, the observed decrease in resistance with the amount of W in Figure 6-11 is mainly determined by the thickness of the film itself.

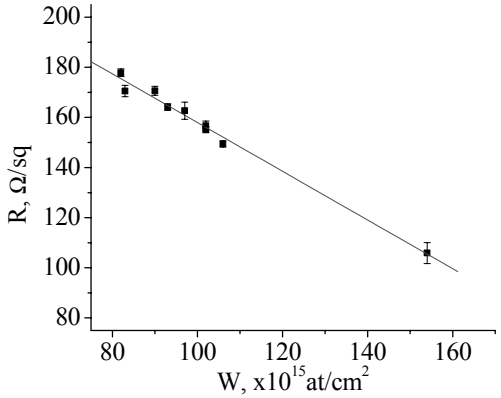

Figure 6-11. Resistance versus amount of W determined with RBS in films deposited at 350 ^{o}C using a low nucleation exposure to Si_2H_6.

In Figure 6-12 the average constant value is $15 \cdot 10^{18}$ (Ω/sq)·(at/cm^2). Given a measured sheet resistance of 164 Ω/sq, a fifty-fifty distribution of W_2N and WN in the film and their densities from the handbook one can calculate a resistivity of ~480 μΩ·cm for our $W_{1.5}N$ films.

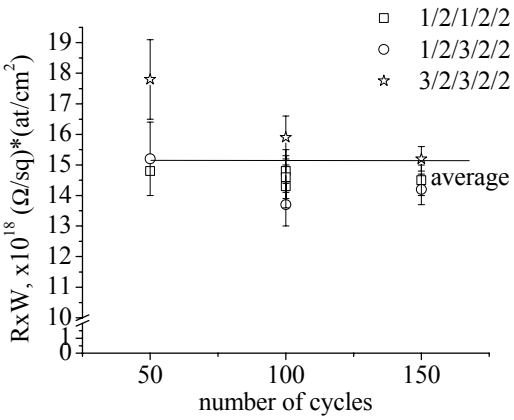

Figure 6-12. Resistance factor normalised with the amount of W versus number of cycles. The amount of W was calculated from (weight of the film-amount of W determined with RBS) dependence. The films are grown using a low nucleation exposure to Si_2H_6.

6.4.2 Tungsten carbonitrides

In Table 6-5 the measured sheet resistance and calculated resistivity of $W_xC_yN_{1-x-y}$ layers are presented. Sheet resistance decreases from 511 down to 421 Ω/sq with an increase of TEB exposure during the nucleation step from $9 \cdot 10^6$ up to $2 \cdot 10^7$ L. STDV of R in % reduces from 9.1% to 2.6%, which demonstrates the improvement of film homogeneity. The resistivity of 463 μΩ·cm was obtained for films with a thickness of 11 nm in close agreement to values reported in literature. For example, Smith reported 700-900 μΩ·cm for analogous layers of 7 nm [7] and Li 350-400 μΩ·cm for 25 nm films [8].

Table 6-5. Sheet resistance and resistivity of $W_xC_yN_{1-x-y}$ films.

№	initial TEB exposure, L	R, Ω/sq	STDV of R, %	thickness, nm	resistivity, μΩcm
1	$9 \cdot 10^6$	511	9.1	10.8	552
2	$2 \cdot 10^7$	421	2.6	11	463

Figure 6-13 shows sheet resistance versus films thickness for a varying nucleation exposure to TEB. STDV of R is presented with error bars.

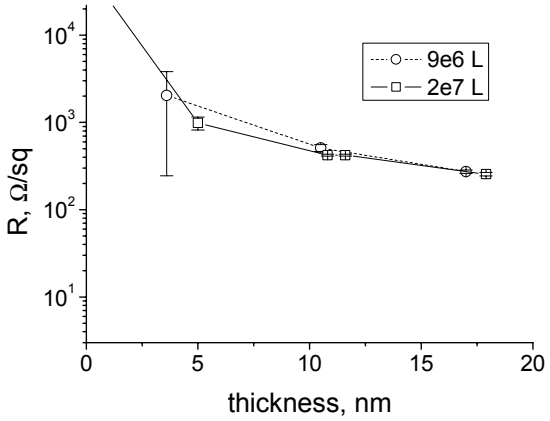

Figure 6-13. Sheet resistance versus film thickness. In the legend the nucleation exposure to TEB is shown.

Resistance and STDV are decreasing for thicker films. At the same time resistivity stays the same for 11 and 18 nm $W_xC_yN_{1-x-y}$ layers grown after the long nucleation step 465 μΩ·cm. Thus, the observed decrease of the sheet resistance is due to the film thickening mainly, as in the case of $W_{1.5}N$ films.

6.5 Evaluation of diffusion barrier properties

In general, electrical tests are much more sensitive then physical analyses and they reveal barrier failure with Cu diffusion after annealing at much lower levels than analytical techniques such as Rutherford Backscattering Spectroscopy, XPS etc. [3], as it was discussed in Chapter 1.2.3. Results of four-point probe *in situ* resistance measurements and measurements of van der Pauw structures, performed to evaluate reactivity of the barrier material with copper, will be discussed. We will also present I-V and C-V measurements of diodes and C-V and C-t tests of capacitors to characterise our diffusion barriers.

6.5.1 Experimental

For electrical characterisation of diffusion barrier properties of $W_{1.5}N$ and $W_{1.5}CN$ films different test structures were manufactured (for details see

Chapter 2.4.1 and 2.4.2). The films on SiO_2 have passed a conventional "scratch and tape" test, confirming sufficient adhesion. After the W-based barrier films were deposited, the wafers were exposed to air and transferred into the sputtering tool for Cu or Al deposition.

Cu (100 nm)/barrier/SiO_2 (700 nm) stacks on Si-substrates were fabricated for four-point probe *in situ* resistance measurements to study the interaction of Cu with the barrier at elevated temperatures in vacuum. Additionally, van der Pauw structures were made to perform sheet resistance measurements after a heat treatment in forming gas (N_2+5% H_2). These devices were made on the wafers with diodes. The thickness of Cu layer was 200 nm for all devices.

p^+/n diodes and capacitors with 200 nm of wet thermal oxide were made on separate 100 nm (100) n-type Si substrates (for details see 2.4 Process flow). This is done to avoid the capacitor to become contaminated during diode test, which could occur when both devices are on the same wafer. When a barrier on a diode fails, Cu diffuses very fast in Si; 440 μm in lowly doped Si ($<10^{15}$ cm^{-2}) and 13 μm in highly doped p-wafer in 2 hours at room temperature [14]. At failure of a barrier, which separates Cu and a Si area in a diode, Cu can be present at the Si/SiO_2 interface and measurements of neighboring capacitors can be distorted even without Cu diffused into SiO_2. Diodes with a varying area between 100x100 μm^2 and 1600x1600 μm^2 had a different geometry of the contacts openings and a varying perimeter to area ratio. A p^+/n junction was fabricated with BF_2^+ ion implantation at about 0.25 μm depth. Diodes were tested with a barrier thickness of 7 or 10 nm, capacitors with a barrier of 10 nm thick. Cu reference diodes were made with an ultra thin (~3 nm) adhesion layer. Cu reference capacitors were made with a direct Cu contact to SiO_2. Cu or Al was used as a metal for electrodes. Both as prepared and annealed devices were measured to monitor Cu-diffusion. Annealing was done at 200 and 400 ºC in N_2+5% H_2 ambient for 30 min.

C-V tests of diodes were done under reverse bias. I-V measurements were performed using a HP 4256A parameter analyser and the Material Development Corporations (MDC) CSMWin program. The leakage

current is measured at –5 V. Leakage of the set up was $5x10^{-15}$ A. C-V and C-t tests of capacitors were done at 10 kHz with a HP 4140B pA meter as a DC voltage source, a HP 4275 multi-frequency meter and the MDC CSMWin computer program.

6.5.2 Reactivity of Cu and barrier material

6.5.2.1 Four-point probe sheet resistance

The measurements were done with a ramp-up and cool-down step of 0.01degree/s in vacuum at a base pressure of $4 \cdot 10^{-6}$ mbar. After the temperature reached 500 ºC, it was kept constant for 15 minutes and then cooled down to room temperature.

Barrier layers with 100 nm Cu on top were tested during *in situ* four-point probe measurements upon heating. The results (resistance normalised to resistance after heat treatment) for pure Cu on SiO_2 and for Cu on two types of barrier are shown in Figure 6-14. Upon heating up to ~250 ^{o}C the slope of the curve deviates significantly from the expected linear Thermal Coefficient of Resistance (TCR) and the resulting net decrease in resistance is measured after the annealing cycle. At temperatures above 250 ^{o}C no unexpected change in resistance is observed. The resistivity of the 100 nm Cu layer on oxide (no barrier) was 2.53 and 2.06 μΩ·cm before and after anneal at 500 ^{o}C, respectively. Thus, at low temperatures the resistance of Cu decreases due to the annealing of defects. A 200 nm Cu film on oxide was 2.1 μΩ·cm before anneal, showing that the thinner Cu film had more defects. The 100 nm Cu layer deposited on barriers showed even higher sheet resistances, but after annealing the resistivity was close to the value of Cu on oxide. This indicates that there has been no reaction between the barrier and the Cu. The results of the test are summarized in Table 6-6.

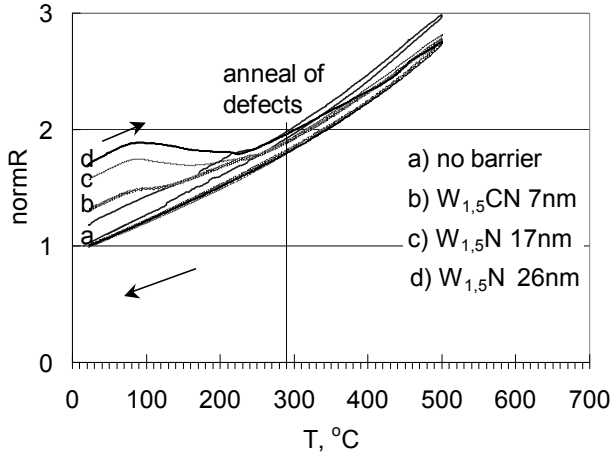

Figure 6-14. Normalised resistance versus temperature during the heat treatment. Arrows indicate heating up and cooling down.

Table 6-6. Results of the four-point probe resistance test with 100 nm Cu layer.

№	barrier thickness, nm	barrier composition	R_{before}, mΩ/sq	R_{after}, mΩ/sq
1	no	-	253	206
2	17	$W_{1.5}N$	365	235
3	20.5	$W_{1.5}N$	335	214
4	25.8	$W_{1.5}N$	450	225
5	26.3	$W_{1.5}N$	372	220
6	7	$W_{1.5}CN$	270	207

Some samples were annealed up to 700 °C. This high temperature resulted in agglomeration of Cu on the underlying $W_{1.5}N$ barrier layer. No intermixing of layers was observed and the resistance of the barrier could still be measured. In the case of a sample with Cu/$W_{1.5}CN$ combination the resistance increased by a factor of 1.4. This can be explained by the interaction of Cu and $W_{1.5}CN$. At least up to 500 °C no interaction was observed between the barriers and Cu film.

6.5.2.2 Van der Pauw structures

Van der Pauw structures were fabricated for sheet resistance measurements. Devices with Cu/$W_{1.5}N$ and Cu/$W_{1.5}CN$ stacks were measured before and after a heat treatment at 400 °C in forming gas

(N_2+5% H_2) for 30 minutes. The Cu layer has a thickness of 200 nm and the barrier thickness was 7 or 10 nm. A Cu-reference sample was prepared with an adhesion layer of $W_{1.5}CN$ with a thickness of 3 nm. Such a thin layer does not serve as a functional diffusion barrier. For the process details see 2.4. Process flow.

Two designs of van der Pauw structures were available to test our W-based barriers.

P3 was used to test the Cu/barrier stacks on SiO_2 to monitor changes caused by an interaction of Cu with the underlying barrier.

P2 was prepared to measure sheet resistance of the Cu/barrier stacks on Si. In these measurements the Cu, the barrier and the active Si are resistors in parallel. As the Cu layer has the lowest sheet resistance in this combination, a resistance change after the heat treatment will be ascribed to the resistance change of the Cu layer only. This can be a result of a reaction of the barrier with Cu- or Si-diffusion into Cu. Given 1 at% Si in Cu the Cu resistivity will increase from 1.7 μΩ·cm up to 3.7 μΩ·cm (see 5.3.4) [11].

The results of the sheet resistance measurements are presented in Table 6-7. The normalised resistance, R_{norm}, is given as the sheet resistance after the heat treatment divided by the resistance before.

Metallisation on SiO_2 (P3)

Cu reference sample showed no change of resistance after the heat treatment, 108 μΩ·cm before and 108 μΩ·cm after the heat treatment, respectively (see № 1 in Table 6-7). Thus no changes occurred in the Cu film. Samples with barriers showed the decrease of sheet resistance after the temperature treatment (see № 2-4 in Table 6-7). This decrease is attributed to the annealing of defects in the Cu layer on barriers (as it was discussed earlier in this Chapter). Thus, the $W_{1.5}N$ and $W_{1.5}CN$ compounds do not interact to a large extent with Cu at 400 ^{o}C.

Table 6-7. Normalised resistance of van der Pauw structures after the heat treatment.

№	metallisation stack	P3 on SiO_2	P2 on Si
		R_{norm}	R_{norm}
1	Cu/ adhesion layer	1.0	1.1
2	Cu/ 10nm $W_{1.5}N$	0.9	0.9
3	Cu/ 7nm $W_{1.5}N$	0.9	1.1
4	Cu/ 10nm $W_{1.5}CN$	0.9	1.2

Metallisation on Si (P2)

P2 devices on the Cu reference showed a 10 % increase of the sheet resistance after the temperature treatment (see № 1 in Table 6-7). The expected increase, however, should be by a factor of 30 related to a full transformation of 200 nm Cu film on Si into Cu_3Si under this heat treatment [14, 15]. Thus, the diffusion of Si was retarded by the adhesion film. Samples with barriers showed an increase of resistance up to 20 %, revealing changes in Cu (see № 3, 4 in Table 6-7). This could correspond to ~0.2 at% Si dissolved in Cu. These low concentrations cannot be measured with the used analytical techniques, i.e. AES and XPS. The source for Si could be a thin layer Si containing W grown due to the use of WF_6 and the reaction with Si in a few first cycles of the deposition process due to precursors and nucleation conditions used. Thus, the resistance change can be ascribed to Si diffusion from barrier/Si interface into Cu. No changes of sheet resistance after the heat treatment were measured for the sample with the film of $W_{1.5}N$ with a thickness of 10 nm (see № 2 in Table 6-7). Thus, this film was thick enough to prevent Si diffusion into Cu.

Sheet resistance measurements on structures (P3) showed that no reaction between Cu and $W_{1.5}N$ and $W_{1.5}CN$ compounds occurred at 400 ^oC for 30 minutes. Van der Pauw structures with 7 nm film of $W_{1.5}N$ and 10 nm film of $W_{1.5}CN$ grown on Si (P2) showed an increase of resistance, probably, due to Si-diffusion. The sample with the 10 nm film of $W_{1.5}N$ did not show measurable changes of resistance, demonstrating a stability of the

Cu/barrier/Si combination. No conclusions about Cu diffusion into Si can be done based on these measurements. To study Cu diffusion in Si C-V and I-V measurements on diodes were performed.

6.5.3 Diffusion properties of thin films

6.5.3.1 Diodes

Capacitance-Voltage (C-V) and Current-Voltage (I-V) characteristics of diodes with Cu/barrier, Al/barrier and Cu contacts were measured. Results of C-V test are used to calculate the effective carrier density and built-in voltage in the junction. Analysis of I-V characteristics gives a generation and a diffusion current component. These values serve as an input for the calculation of generation and minority lifetime, respectively.

A. C-V measurements

The results of the C-V measurements are presented as an $Area^2/C^2$-V dependence in Figure 6-15. The slope of the lines is inversely proportional to the effective doping level. The different slopes found in Figure 6-15 are due to wafer to wafer variation of doping level. The slope does not change significantly even after 400 ^oC annealing. The changes after the heat treatment of doping and built-in voltage are insignificant. Based on these data no conclusion about Cu diffusion can be drawn. Thus, the C-V test is not sensitive enough for a determination of the barrier failure.

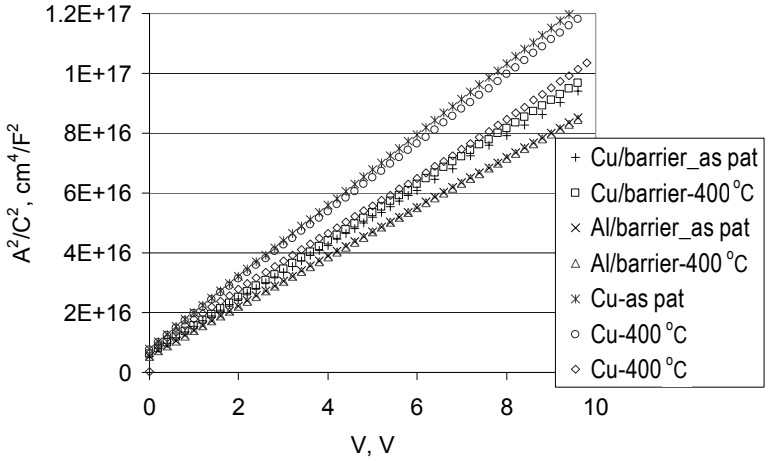

Figure 6-15. (A^2/C^2-V) plot for as patterned and annealed diodes.

B. I-V test

Cu reference

The Cu reference was measured to monitor the Cu diffusion. Figure 6-16 shows the leakage current before and after the heat treatment at 200 and 400 ^{o}C for diodes D1÷D5. The leakage current increases with the diode area and the perimeter for as patterned diodes and diodes received 200 ^{o}C heat treatment (circles and triangles respectively).

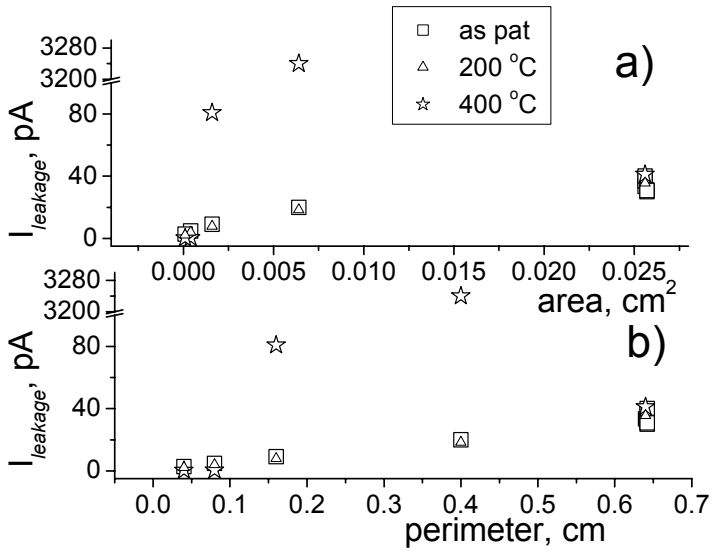

Figure 6-16. Leakage current versus area (a) and perimeter (b) for the Cu reference diodes (D1÷D5).

No increase of the leakage current is observed after the 200 ^{o}C treatment. Some devices annealed at 400 ^{o}C show an increase of the leakage current of 3 orders of magnitude. (Beware that there is a break in the y-axis at 100 pA.) This can be attributed to the diffusion of Cu.

Figure 6-17 presents the leakage current of diodes with a varying area of metal/Si contact (see DS1÷DL3 in Chapter 2, figure 2-8). Tests were performed for as patterned wafers and annealed at 400 ^{o}C (squares and stars). The current increase was random after the annealing. There is no direct relation between this rise and the area or perimeter of the metal contact to the Si. The increase of the reverse current is accompanied with a change of the forward current as well.

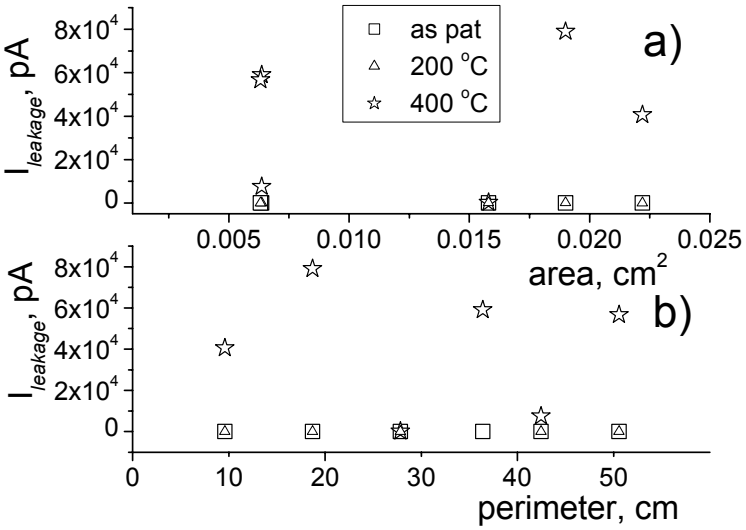

Figure 6-17. Leakage current versus metal/Si contact area for Cu reference diodes (a) and its perimeter (b). Active area of all devices is equal 1600x1600 μm^2.

Figure 6-18 shows the forward *I-V* characteristics. The current, I, has two components: a diffusion current in the neutral region, I_{dif}, and a recombination current in the space charge region of the diode, I_R:

$$I = I_{dif} + I_R \qquad \textit{Equation 6-1}$$

The diffusion and recombination current components, $I_{component}$, depend exponentially on applied voltage, V:

$$I_{component}(V) = I_{component}(0) \cdot \left[\exp\left(\frac{qV}{mk \cdot T} \right) - 1 \right] \qquad \textit{Equation 6-2}$$

where $I_{component}(0)$ is a current component at zero voltage;
m= 1 for the diffusion component;
m= 2 for the recombination component.
The diffusion and recombination current under zero bias, $I_{dif}(0)$ and $I_R(0)$, are obtained from lg*(I-V)* plots as an intercept of the line with a slope proportional to *[V/(kT)]* and *[V/ (2kT)]*, respectively, with the y-axis. For as patterned samples the recombination process in the space charge region is so much lower that the slope is proportional to *[V/(kT)]* over the complete voltage range. Thus the diffusion current in the neutral region dominates in the present voltage range. After the 400 °C annealing the

current increases. The slope of *I-V* curves alters at a bias < 0.6 V (dashed lines). This is due to the increase of the current in the space charge region, which can be ascribed to Cu diffusion into Si. The increase of the diffusion current in the neutral region is very small.

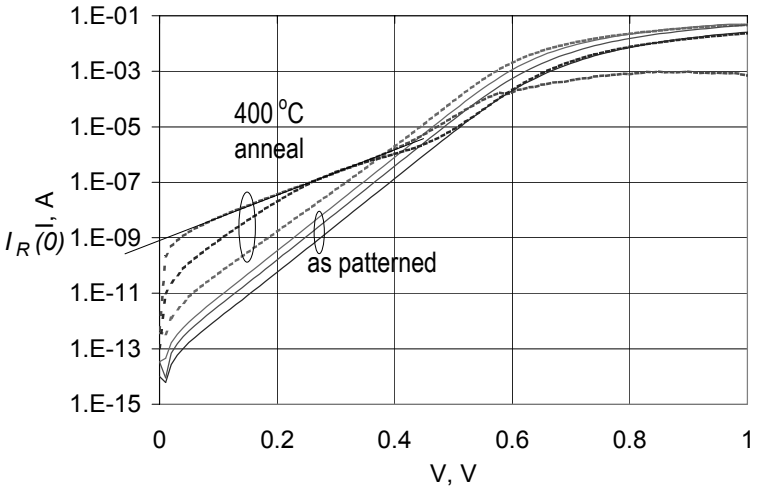

Figure 6-18. Forward I-V characteristics of the Cu reference diodes (D3÷D5 from figure 6-16) as patterned and annealed at 400 °C.

Diodes with barriers

Diodes with Cu metallisation and a $W_{1.5}N$ and a $W_{1.5}CN$ barrier layer of 7 or 10 nm are measured before and after the annealing treatment. Samples with Al metallisation on the 10 nm barrier serve as a reference.

TUNGSTEN NITRIDE

Figure 6-19 shows the leakage current density for diodes with the 10 nm barrier with different area before and after 400 °C annealing treatment. The leakage increases with a smaller area and a higher perimeter to area ratio, correspondingly. The same effect was observed for diodes with the 7 nm barrier. This means that the contribution of the perimeter current component becomes dominant in devices with a small area. After annealing, the smaller the area of diodes, the larger the decrease of leakage is. This reveals that a contribution of the perimeter current component to leakage becomes smaller.

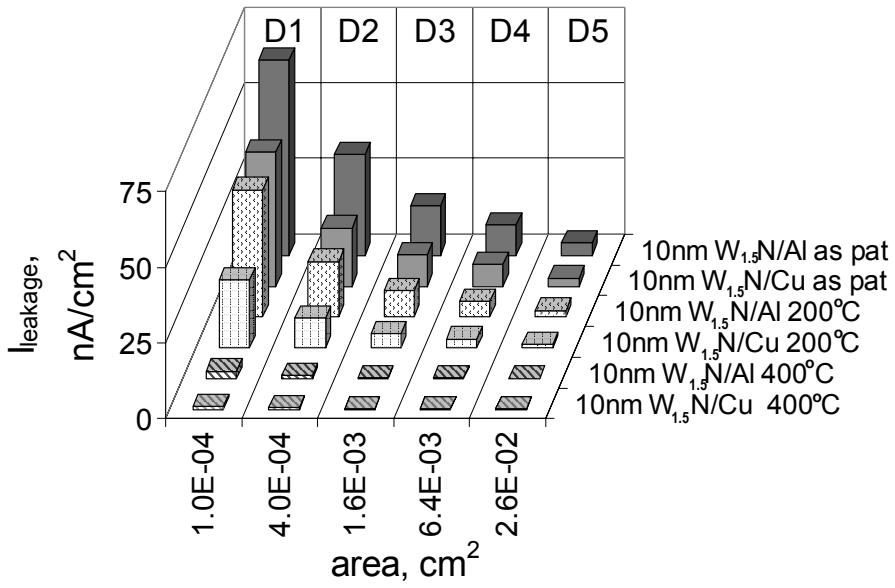

Figure 6-19. Leakage current density of diodes with different area.

This effect can be due to the annealing of plasma damage, introduced during the etching of barriers.

Figure 6-20 shows the leakage current density for Cu/7nm and Cu/10 nm barrier, Al/10 nm barrier and Cu contacts after 400 ^{o}C anneal. Cu reference diodes demonstrate a huge rise of the leakage current, while diodes with Al/barrier and Cu/barrier contacts show very low leakage current. For each type a number of diodes have been measured, they all show similar behavior. Obviously, the concentration of Cu in the diodes on Cu reference reached the level, at which Cu behaves as a trapping center. In opposite, no Cu trapping centers are present in samples with barriers.

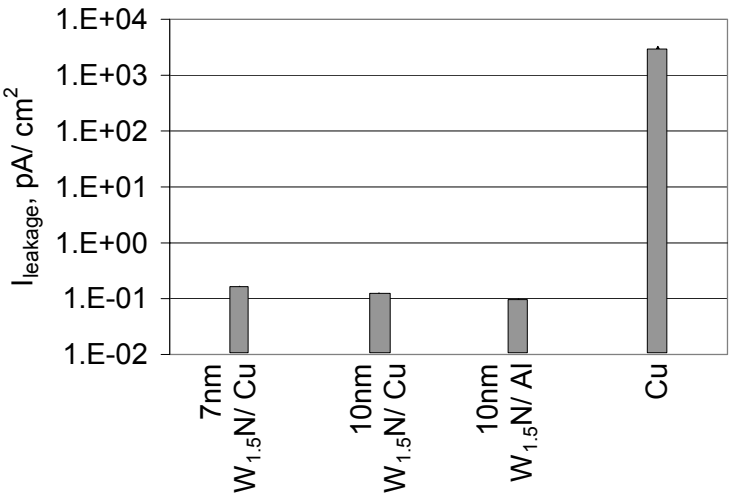

Figure 6-20. Leakage current density of diodes annealed at 400 ^oC in forming gas with area of 1600x1600 μm^2 (DL2).

In Figure 6-21 leakage currents are shown for large diodes with the area of (1600 μm)^2 and different contact area of barrier to Si (DL1÷3, DS1÷3 in Chapter 2, figure 2-8). This picture illustrates no dependence of leakage current on the area of the contact to the Si. No influence of the perimeter of this contact was observed. Essential in this picture is that a huge increase is only observed for diodes without a barrier. In all other cases the current decreases due to anneal of plasma damage.

The conclusion can be drawn that 7 and 10 nm of $W_{1.5}N$ withstand Cu and Al diffusion at least up to 400 ^oC anneal for 30 minutes.

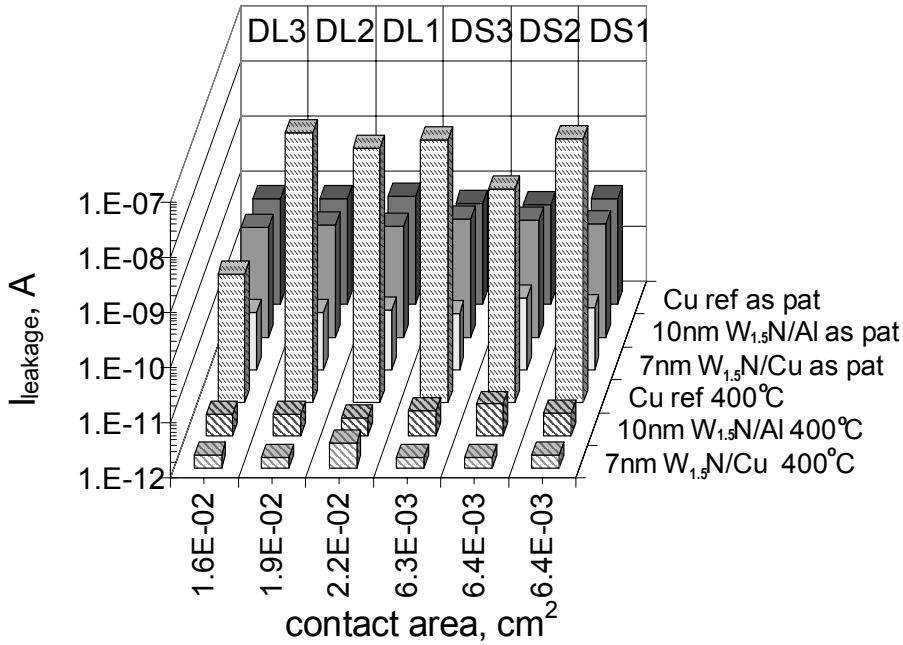

Figure 6-21. Leakage current of diodes with different area of contact of $W_{1.5}N$ film to the Si. All diodes have the same active area of 1600x1600 μm^2.

TUNGSTEN CARBONITRIDE

After 400 ^{o}C anneal all diodes with one contact opening with barrier layers and having an area ≤1600x1600 μm^2 (D1÷D5) showed a decrease of leakage current. This decrease occurred due to the annealing of plasma damage, like in diodes with $W_{1.5}N$ films. Figure 6-22 shows the leakage current of large diodes (1600x1600 μm^2) DL1÷3 and DS1÷3 with the different contact area of metallisation to Si. Before heat treatment no difference in leakage current was observed for devices with a Cu/barrier, an Al/barrier combination and Cu reference samples. After annealing one large diode among eleven failed with the increase of the leakage current by a few orders. This is not an inherent property of the barrier material, but most probably a defect on such extremely large area diode. This failure can indicate paths available for Cu, e.g. pinholes formed locally and random during the films growth. Devices with the Al/barrier combination showed no increase of leakage current.

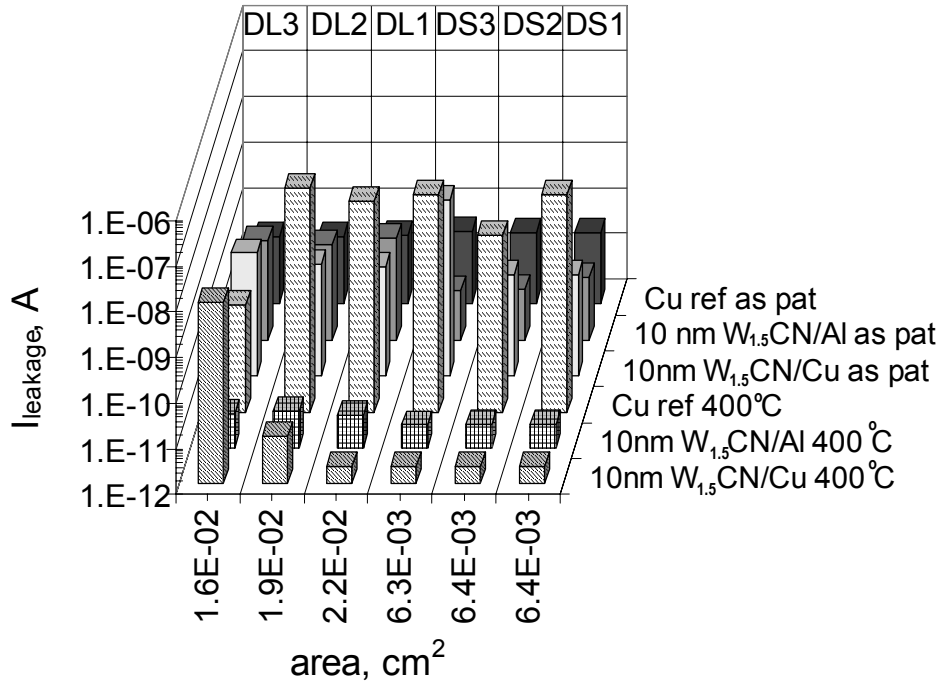

Figure 6-22. Leakage current of diodes with different area of contact of $W_{1.5}CN$ film to the Si. All diodes have the same active area of 1600x1600 μm^2.

Thus, the 10 nm $W_{1.5}CN$ film prevents Al diffusion after the 400 ^{o}C heat treatment. Blocking properties against Cu diffusion are good.

C. Generation lifetime and minority lifetime in the neutral region

Table 6-8 shows the calculated minority lifetime, which is related to the diffusion current in the neutral region at zero bias, $I_{dif}(0)$, as follows:

$$\tau_p(0) = \left[\frac{A \cdot q}{I_{dif}(0)} \cdot \frac{n_i^2}{N_D} \right] \cdot D_p \qquad \textit{Equation 6-3}$$

The minority lifetime does not change substantially after the heat treatment on diodes with barriers. Cu reference diodes show a decrease of the minority lifetime. This can indicate that Cu has diffused through the p/n junction.

Table 6-8. Minority lifetime.

№	annealing treatment	minority lifetime in neutral region, μs	
		Cu/ 10nm $W_{1.5}N$	Cu reference
1	no	600	1100
2	400 °C	640	280

Based on the reverse current, the generation lifetime in the space charge region, τ_g, was calculated for devices with an area of 1600x1600 μm^2 using the following expression:

$$\tau_g = \frac{A \cdot q \cdot n_i \cdot W_i}{2 \cdot I_g} \qquad \textit{Equation 6-4}$$

where W_i is the generation layer thickness related to an applied voltage and doping density, which is determined in C-V diodes test with an equation 2-15 (Chapter 2).
The generation current, I_g, was determined at –5 V as leakage current, $I_{leakage}$, minus diffusion current, I_{dif}, obtained with forward I-V characteristics:

$$I_g = I_{leakage} - I_{dif} \qquad \textit{Equation 6-5}$$

The measured currents, however, are not corrected for an area- and perimeter contribution.

The calculated generation lifetime is presented in Table 6-9. For the Cu reference there is a decrease of the lifetime from ~100 down to 0.2 μs upon annealing. This is explained by Cu diffusion and the formation of Cu trapping centers, which are very effective lifetime killers [16]. For the diodes with barriers the calculated generation lifetime increases after the anneal. The obtained increase of the generation lifetime is owed to the leakage value used in calculations, which was not corrected by the perimeter component of current. The area current component and a real generation lifetime, respectively, might remain unchanged. After annealing the contribution of perimeter current into leakage is reduced. As a result, the calculated generation lifetime after anneal becomes closer to the actual one. The generation lifetime for diodes with an Al/barrier contact and a

Cu/barrier contact is of the same magnitude and much higher than for diodes without a barrier, 1300, 1200 μs and 0.2 μs, respectively (see Table 6-9, № 2). Thus, no Cu or Al diffusion through the barriers occurred during the 400 °C anneal. In the case of $W_{1.5}CN$ film values of generation lifetime and minority lifetime are similar to values for $W_{1.5}N$ films. Therefore both the $W_{1.5}N$- and the $W_{1.5}CN$ layers show the good blocking properties against Cu and Al diffusion.

Table 6-9. Generation lifetime.

№	annealing treatment	generation lifetime, μs		
		Cu reference	Cu / 10nm $W_{1.5}$ N	Al / 10nm $W_{1.5}$ N
1	no	100	40	26
2	400 °C	0.2	1200	1300

Thus, Cu diffused into Si gives a huge reduction of generation lifetime in the space charge region (see Table 6-9). This is less pronounced for the minority lifetime in the neutral region (see Table 6-8), probably, because this neutral region is further away from the Cu source.

6.5.3.2 Capacitors

A. C-V and C-t measurements

C-V and C-t measurements were done on MOS-capacitors with Cu-, Al/barrier- and Cu/barrier-electrodes. Capacitors with a Cu electrode were used as a reference. Figure 6-23 shows the results of the measurements for the Cu reference before and after temperature treatment at 400 °C in N_2+5% H_2 ambient for 30 min. After the heat treatment the shift of flatband voltage towards negative voltage was insignificant (-0.05 V). Simultaneously, the change of the slope of the C-V curve in depletion shows the annealing of states at the SiO_2/Si interface. Figure 6-24 shows results of the C-V measurements for capacitors with Al/barrier and Cu/barrier contacts. The flatband voltage for both types of capacitors shifted towards positive voltage. The slope of the C-V curve in depletion has also changed, indicating the decrease of interface states.

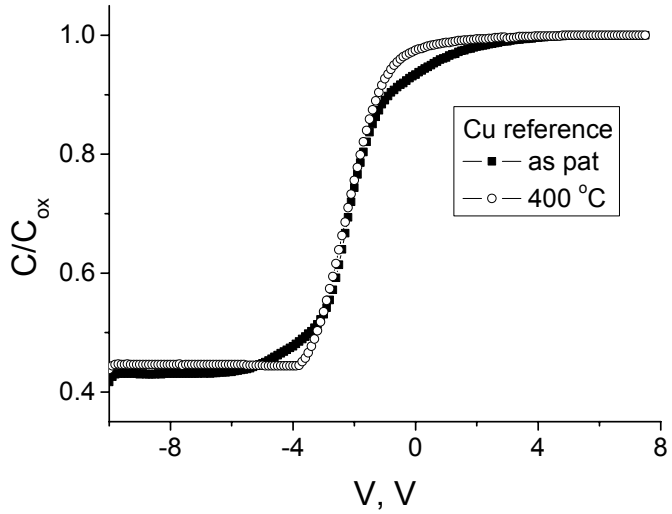

Figure 6-23. Normalized capacitance versus applied voltage for as patterned capacitors and capacitors after annealing at 400 °C in forming gas with Cu electrode to SiO_2.

The calculated oxide charge is shown in Table 6-10. The oxide charge, N_{ss}, for the Cu reference changes negligibly after anneal. For samples with Al/barrier and Cu/barrier contacts the oxide charge becomes lower after the heat treatment. Probably, the plasma during the etching of barriers or the deposition process of barriers creates charged traps in the oxide, which density can be decreased at 400 °C in forming gas, alike in capacitors with $W_xSi_yN_{1-x-y}$ barriers (see Chapter 5, 5.3.3). The interface state density, D_{it}, presented in this table, was calculated with the Terman method [17]. The density of interface states for capacitors with all types of electrode decreases after 400 °C anneal, e. g. from ~$4x10^{10}$ down to $1x10^{10}$ $cm^{-2}eV^{-1}$ for samples with barriers with Al or Cu metallisation (see № 2-5 in Table 6-10). Thus this heat treatment results in the annealing of both the interface states and oxide charges.

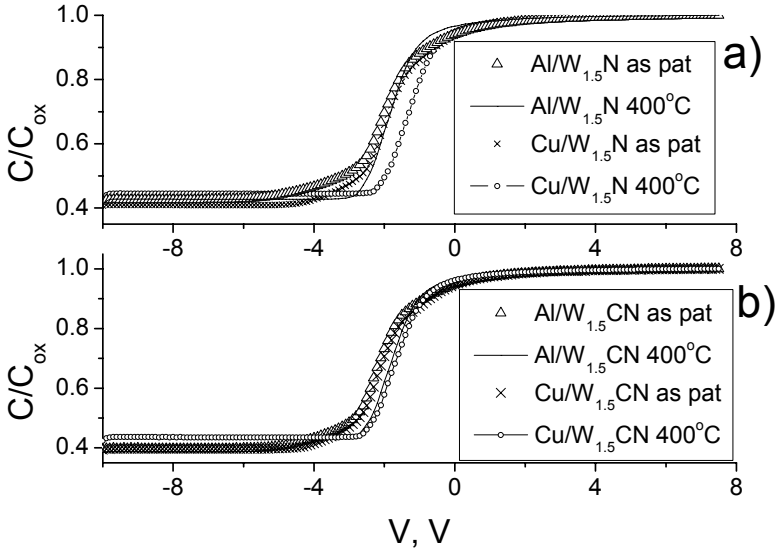

Figure 6-24. Normalized capacitance versus applied voltage for as patterned capacitors and capacitors annealed at 400 °C in forming gas: a) with $W_{1.5}N$ and b) $W_{1.5}CN$ barrier layers.

The results of C-t tests are presented in Figure 6-25 and Figure 6-26 as Zerbst plots for samples with the Cu-, Al/barrier- and Cu/barrier electrode to SiO_2, respectively. The slope of the Zerbst plot is inversely proportional to the generation lifetime. Annealed devices show a longer lifetime.

Table 6-10. Oxide charge N_{SS} and interface state density D_{it} before and after annealing in forming gas.

№	contact to SiO_2	N_{ss}, cm^{-2}		D_{it}, $cm^{-2}\,eV^{-1}$	
		as patterned	400 °C	as patterned	400 °C
1	Cu	1.79E+11	1.85E+11	4.0E+10	3.2E+10
2	Al/$W_{1.5}$N	1.97E+11	1.60E+11	3.0E+10	1.0E+10
3	Cu/$W_{1.5}$N	1.55E+11	1.04E+11	3.5E+10	1.0E+10
4	Cu/$W_{1.5}$CN	1.92E+11	1.56E+11	3.0E+10	1.0E+10
5	Al/$W_{1.5}$CN	1.78E+11	1.43E+11	3.0E+10	1.5E+10

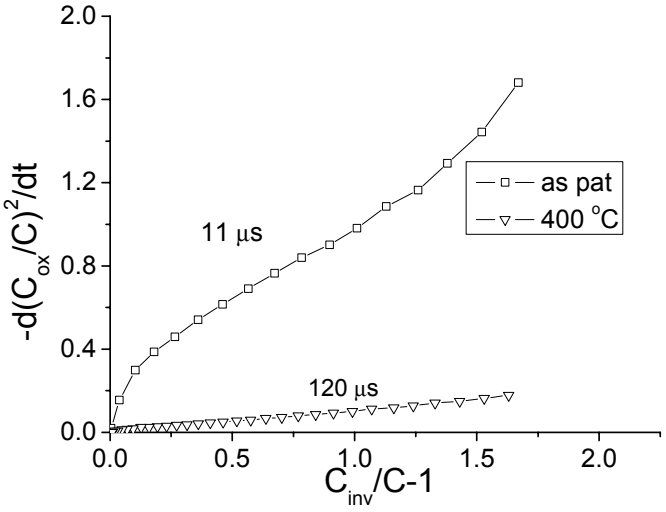

Figure 6-25. Zerbst plot for capacitors with Cu electrode to SiO_2 before and after anneal at 400 °C in forming gas.

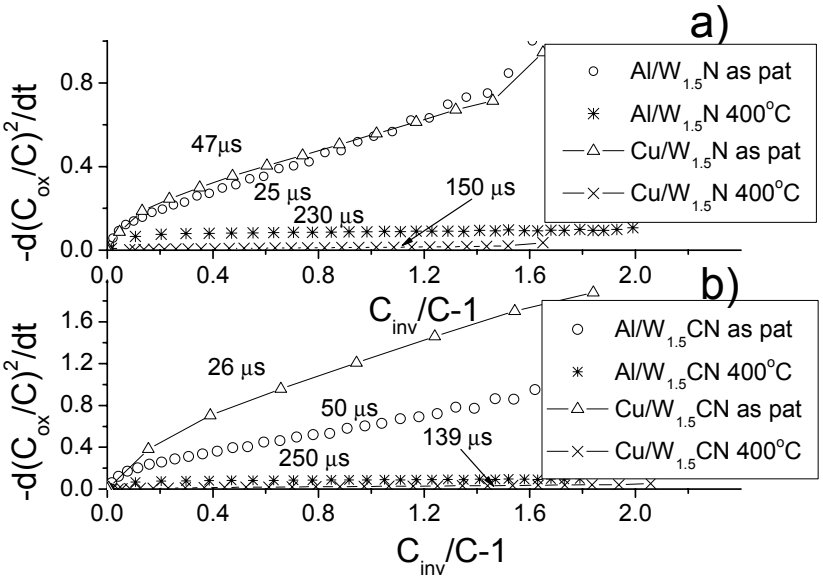

Figure 6-26. Zerbst plot for capacitors with a) $W_{1.5}N$- and b) $W_{1.5}CN$ barrier films before and after 400 °C annealing in forming gas.

No deterioration of oxide properties or interface state density, nor a deterioration of lifetime, which would accompany the diffusion of Cu, was observed with C-V and C-t tests. The lifetime even improved due to the annealing at 400 °C in forming gas. C-V and C-t measurements are not sensitive, however, to Cu ions with a low density when they are located underneath the metallisation in the SiO_2 within a small thickness. TVS and

BTS measurements are more sensitive for mobile ions determination. Results and their discussion are presented in the following sections.

B. TVS

TVS measurements are performed at 250 ^{o}C after a stress at +2 MV/cm with a sweep of -0.1 V/s. Capacitors with an Al electrode to SiO_2 are now used as a reference, because the Cu electrode loses adhesion to SiO_2 at 250 ^{o}C in air environment. The diffusion properties of barriers are tested in devices with Cu/$W_{1.5}$CN, Cu/$W_{1.5}$N and Al/$W_{1.5}$N electrodes. The test is carried out on devices annealed at 400 ^{o}C for 30 or 150 min.

Figure 6-27 shows results of the measurements on capacitors with Al and Cu/$W_{1.5}$CN contacts to SiO_2 after the heat treatment. Both samples show a peak around zero voltage. This peak corresponds to Na^+ ions with a density of $1.8 \cdot 10^{10}$ and $3.8 \cdot 10^{11}$ cm^{-2} for Al and Cu/$W_{1.5}$CN electrodes, respectively. Thus no Cu or other mobile ions are present in the oxide. The films with a 10 nm thick $W_{1.5}$CN barrier withstand a diffusion of Cu during TVS stress at 250 ^{o}C after bias at +2 MV/cm.

Figure 6-28 shows TVS plots for the capacitors after anneal for 30 min. in forming gas with Cu/$W_{1.5}$N and Al/$W_{1.5}$N electrodes. Both curves have two peaks. One peak around 0 V is attributed to Na^+ ions. The Na^+ charge has a density of $2.0 \cdot 10^{11}$ and $4.6 \cdot 10^{11}$ cm^{-2}, for Al and Cu metallisation, respectively (see circles and squares in Figure 6-28). As in samples with the $W_{1.5}$CN film the concentration of sodium is higher for Cu metallisation, which indicates a difference in purity between the sputtering tools for Al and Cu. The second peak is located between -10 V and -15 V with broad shoulders for both Al and Cu metallisation. Because it is observed in the case of both Al and Cu electrodes, this peak cannot be attributed to Cu^+ mobile ions. The density of this charge is very high and equal to $2.2 \cdot 10^{13}$ cm^{-2} and $6.5 \cdot 10^{12}$ for Al/$W_{1.5}$N and Cu/$W_{1.5}$N contacts, respectively.

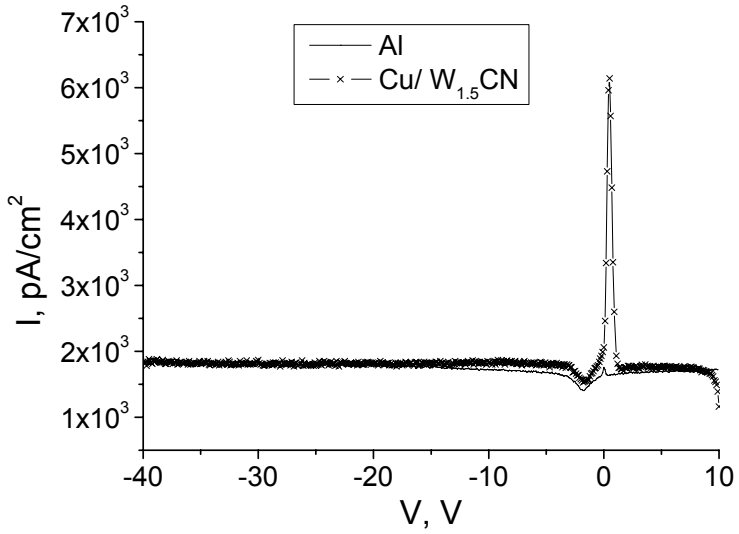

Figure 6-27. TVS plot at 250 °C after 5 min stress at +2 MV/cm. Current is normalized to the device area. Capacitors were annealed for 30 min at 400 °C in forming gas.

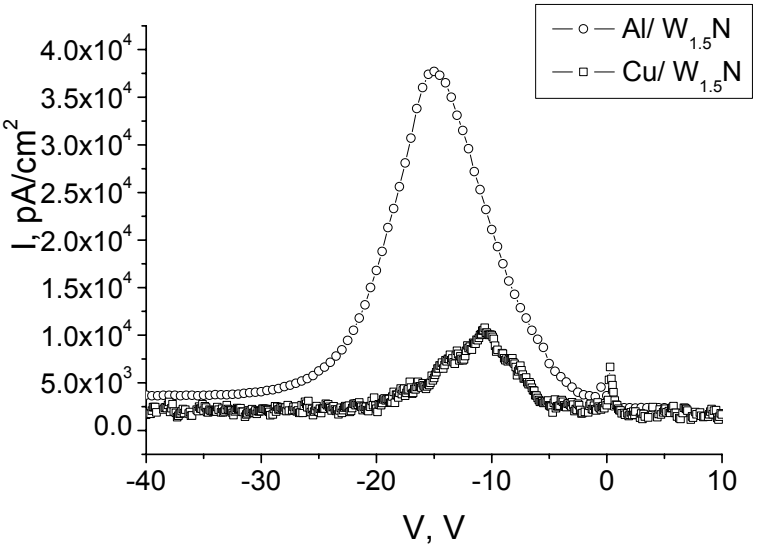

Figure 6-28. TVS curve at 250 °C after 5 min stress at +2 MV/cm. Current is normalized to the device area. Capacitors were annealed for 30 min at 400 °C in forming gas.

In order to find out how this charge is affected by anneal, additional measurements were performed on Al/$W_{1.5}$N electrode capacitors after longer anneal (for 150 min) in forming gas at 400 °C.

Figure 6-29 shows the results of the measurements after 30 min. and 150 min. anneal at 400 °C. The Na^+ peak increased from $2.0 \cdot 10^{11}$ cm^{-2} to $3.5 \cdot 10^{11}$ cm^{-2} with a longer anneal (Figure 6-29 a), b)). This increase can be ascribed to a contamination coming from the oven during the heat treatment or from diffusion out of the bulk of the metal into the oxide. The maximum of the broad peak of interest corresponds to the charge density, which is reduced with a longer anneal, i. e. from $2.2 \cdot 10^{13}$ to $6.2 \cdot 10^{12}$ cm^{-2} for 30 min and 150 min, respectively (Figure 6-29 a), b)). Thus, at 400 °C this charge cannot be annealed fully. A similar effect was observed on samples with $W_xSi_yN_{1-x-y}$ barrier layer (see Chapter 5). This charge was not observed in oxides with a $W_{1.5}CN$ barrier film after heat treatment.

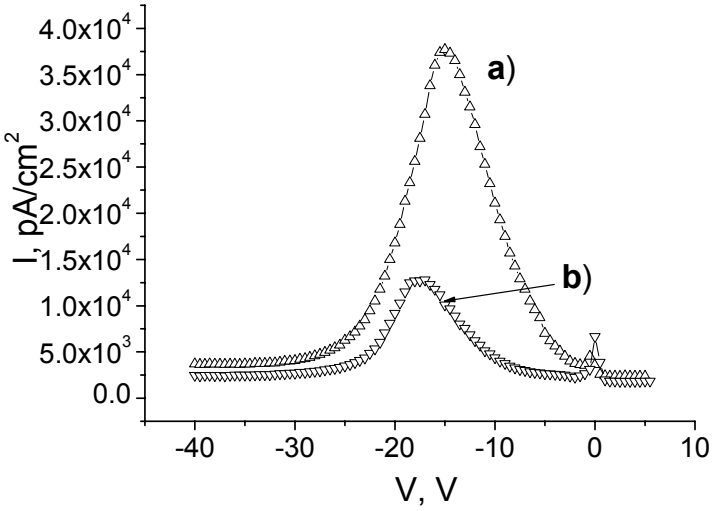

Figure 6-29. TVS curve at 250 °C after 5 min stress at +2 MV/cm for capacitors with Al/$W_{1.5}$N contacts: a) after 30 min anneal at 400 °C in forming gas; b) after 150 min anneal. Current is normalized to the device area.

Due to the large number of unannealed states near the barrier/SiO_2 interface there is the large peak in TVS curve, obscuring any Cu peak [18, 19]. Therefore the TVS method cannot be applied to study diffusion of Cu^+ in the capacitors in the case of $W_{1.5}N$ layers.

TVS method does not provide information on the sign of the charges flowing to the traps, which were present in the oxide underneath tungsten

nitride barrier films. In order to determine the sign of these charges and their nature, BTS tests were applied.

C. BTS

Capacitors with Al/$W_{1.5}N$ contact to SiO_2 were tested before and after the 400 ^oC heat treatment. The conditions of BTS were equivalent to the stress used in the TVS test. Capacitors were stressed at 250 ^oC in air for 5 minutes with an electrical field of +2 and –2 MV/cm. After samples have cooled down under the electrical field, C-V test was performed.

Figure 6-30 shows the C-V plot before and after BTS of the capacitors annealed in a forming gas for 30 min or 150 min. No changes of C-V plot were observed after positive BTS (see circles and plusses in Figure 6-30). After negative BTS capacitors annealed for 30 min. show a negative shift of flatband voltage of -1.7 V (see minuses in Figure 6-30). The negative shift indicates that the traps become positively charged. This must be due to the release of electrons under the stress conditions (negative bias give negative shifts). The shape of the C-V curve in inversion is changed. This can be due to an increase of interface states density at the SiO_2/Si interface under negative bias [19] or due to a nonuniform distribution of the created positive charges. Capacitors annealed for 150 min. also do not show changes of C-V plot after positive bias stress (not shown). After negative bias capacitors show flatband voltage shift of -1 V, which is smaller than the shift for the samples after 30 min anneal (see crosses and minuses in). Thus the defects close to the oxide/barrier interface, serving as traps, could not be annealed completely under these conditions.

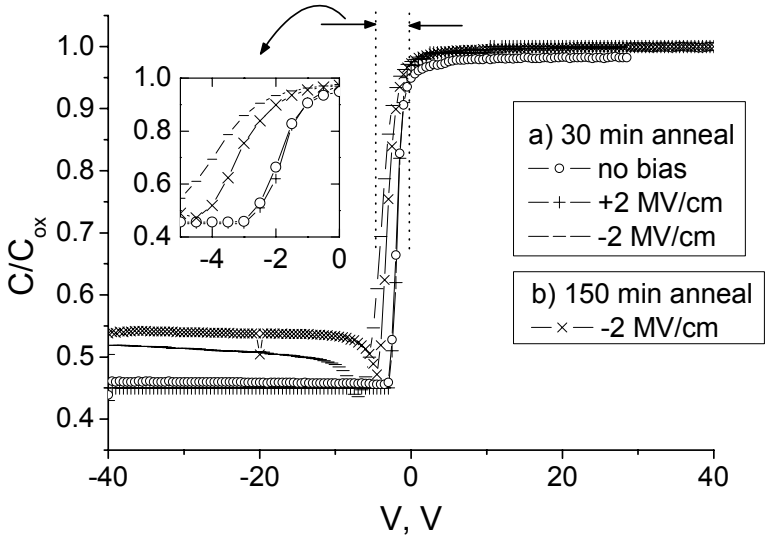

Figure 6-30. C-V plot for a capacitor with Al/ $W_{1.5}N$ contact after annealing at 400 ^{o}C in forming gas before and after BTS at 250 ^{o}C. Time of the annealing is a) 30 min; b) 150 min.

The obtained shifts of flatband voltage after BTS correspond to a lower traps density than the density determined with TVS. This is because changes of flatband voltage are not very sensitive to charges and traps near the gate electrode/oxide interface. Whereas TVS technique measures defects or traps overall in the oxide, For example, charges, located in a 200 nm oxide at a depth of 5 nm beneath the gate, influence forty times less the flatband voltage than charges at the Si/SiO_2 interface. The anneal of these traps (decrease of the related peak with TVS) also explains why the shift of C-V curve after BTS test is less for devices annealed longer in forming gas. These traps or states are probably always there after oxidation but are annealed under Al electrode and also under $W_{1.5}CN$ film, due the reducing action of Al and, may be, TEB. In the case of $W_{1.5}N$ barrier deposition they are not annealed completely. Further study of the anneal of these states has not been performed.

Thus, the charge measured with TVS and BTS is correlated to traps in the oxide underneath the $W_{1.5}N$. These traps, unlike the interface trap charge and plasma damage, cannot be fully annealed at 400 ^{o}C in forming gas.

6.6 Summary and conclusions

Tungsten nitride films have been grown in ALD mode with a repeating pulse sequence of $WF_6/NH_3/C_2H_4/SiH_4/NH_3$. The process has been studied at 325 and 350 ^oC. The growth rate is about 1 monolayer per cycle. The deposited layers are tungsten nitrides with a composition of $W_{1.46}N$ as determined with RBS. No carbon and Si are incorporated. The F- content in the films is at the detection limit of RBS and XPS (0.5 at %). The low F content is due to a combination of SiH_4 and C_2H_4 gases. Moreover, the use of ethene changes the morphology of the obtained layers.

Tungsten carbide nitride films are grown with a cycling of $TEB/WF_6/NH_3$ at 325 ^oC. The composition of layers with RBS is $W_{1.5}CN$. The growth rate of the films is 1.3 Å/cycle. Also here the amount of F is at the detection limit of RBS and XPS.

The layers of $W_{1.5}N$ are characterized with an RMS- roughness of 0.43 nm at a thickness of 16 nm. A 10 nm film of $W_{1.5}CN$ has a roughness as low as 0.33 nm.

Resistivity of $W_{1.5}N$ layers is ~480 $\mu\Omega\cdot$cm, which is 10 times lower than reported earlier by Klaus [5] and Elers [6]. This value is at the same level as the resistivity of our $W_{1.5}CN$ layers being 465 $\mu\Omega\cdot$cm [7, 8].

The combination of the low RMS roughness and low resistivity make these films promising diffusion barriers.

Functional $W_{1.5}N$ and $W_{1.5}CN$ barrier layers have been demonstrated for interconnect. The $W_{1.5}N$ layers with a thickness of 7 and 10 nm and the 10 nm $W_{1.5}CN$ layer did not show failure of barrier properties with I-V test of p^+/n diodes after the 400 ^oC anneal for 30 min in forming gas.

TVS measurements even after 5 min stress at 250 ^oC and +2 MV/cm do not show a failure of a $W_{1.5}CN$ barrier film with a thickness of 10 nm. TVS test cannot be applied, however, to determine Cu diffusion in capacitors with $W_{1.5}N$ layer, because of the masking effect of traps near the barrier/oxide interface.

Both $W_{1.5}N$ and $W_{1.5}CN$ layers serve as good barriers for both Cu and Al metallisation.

p^+/n diodes with Cu contacts without barrier showed an increase of the leakage current by 3 orders and a degradation of minority carrier lifetime after the anneal.

The sensitivity of the C-V test of diodes was insufficient to detect Cu diffusion.

Four-point probe sheet resistance test at elevated temperature showed no Cu- barriers interaction up to 500 ^oC. Test of van der Pauw structures confirmed temperature stability of $Cu/W_{1.5}N$ and $Cu/W_{1.5}CN$ combinations up to 400 ^oC.

C-V and C-t measurements of capacitors do not reveal Cu diffusion in the SiO_2 protected with a 10 nm barrier film after the anneal treatment.

References

1. T. Suntola, Atomic layer epitaxy, *Mat. Sci. Rep*., 4 (7), p. 261-312 (1989).
2. T. Nakajiama,K. Watanabe and N. Watanabe, Preparation of Tungsten Nitride Film by CVD Method Using WF_6, *J. Electrochem. Soc*., 134(12), p. 3175-3178 (1987).
3. C. Ahrens et al., Electrical characterization of $TiN/TiSi_2$ and $WN/TiSi_2$ Cu-diffusion barriers using Schottky diodes, *Microelectronic Engineering*, 33, p. 301-307 (1997).
4. K. M. Chang, T.H. Yeh, I.C. Deng, and C.W. Shih, Amorphouslike chemical vapor deposited tungsten diffusion barrier for copper metallization and effects of nitrogen addition, *J. Appl. Phys*., 82 (3), p. 1469-1475 (1997).
5. J. W. Klaus, S. J. Ferro, S. M. George, Atomic layer deposition of tungsten nitride films using sequential surface reactions, *J. Electrochem. Soc*., Vol. 147, N 3, p. 1175-1181 (2000).
6. K.-E. Elers, V. Saanila, P.J. Soininen, W.-M. Li, J.T. Kostamo, S. Haukka, J. Juhanoja, W.F.A. Besling, *Chem. Vap. Deposition*, 8, No. 4, p. 149-153 (2002).
7. S. Smith, W.-M. Li, K.-E. Elers, K. Pfeifer, Physical and electrical characterization of ALCVD^{TM} TiN and WN_xC_y used as a copper diffusion

barrier in dual damascene backend structures, *Microelectronic Engineering*, 64, p. 247-253 (2002).

8. W.- M. Li, K. Elers, J. Kostamo, S. Kaipio, H. Huotari, M. Soininen, P. J. Soininen, M. Tuominen, S. Haukka, S. Smith, W. Besling, Deposition of WN_xC_y thin films by ALCVD™ method for diffusion barriers in metallization, *Proceedings of the IEEE 2002 International Interconnect Technology Conference (Cat. No.02EX519)*, p. 191-193 (2002).
9. K. Nakagawa, M. Fukuda, S. Miyazaki, M. Hirose, Self-assembling formation of silicon quantum dots by low pressure chemical vapor deposition, *Mat. Res. Soc. Symp. Proc*. Vol. 452, p. 243-248 (1997).
10. G. Robertshaw and P. J. Estrup, Kinetics of thermal desorption and thermal conversion of adsorbates: AES studies, *J. Vac. Sci. Technol*. 15(2), p. 554-558 (1978).
11. S. Bystrova, J. Holleman, P.H. Woerlee, R.A.M. Wolters, Electrical characterisation and properties of LPCVD W-Si-N barrier layers for Cu-metallization, *SAFE Proceedings*, (2000).
12. J. J. L. Alay, H. Bender, G. Brijs, A. Demesmaeker and W. Vandervorst, Qualitative Analysis of W(N), TiW and TiW(N) Matrices using XPS, AES, RBS, EPMA and XRD, *Surface and Interface Analysis*, Vol. 17, p. 373-382 (1991).
13. S.H. Kim, S.S. Oh, K.B. Kim, D.H. Kang, W.M. Li, S. Haukka, and M. Tuominen, Atomic-layer-deposited WN_xC_y thin films as diffusion barrier for copper metallization, *Appl. Phys. Lett.*, 82 (25), p. 4486-4488 (2003).
14. A. A. Istratov and E. R. Weber, Physics of copper in silicon, *J. Electrochem. Soc*., 149, G21-G30 (2002).
15. M. O. Aboelfotoh, L. Krusin-Elbaum, Electrical transport in thin films of copper silicide, *J. Appl. Phys.*, v 70, n 6, p 3382-3384 (1991).
16. R. Sachdeva, A.A. Istratov, E.R. Weber, Recombination activity of copper in silicon, *Appl. Phys. Lett*., 79 (18), p. 2937-2939 (2001).
17. E. H. Nicollian, J.R. Brews, MOS (metal oxide semiconductor)physics and technology, Wiley, 1982, ISBN 0-471-08500-6.
18. J. Cluzel, F. Mondon, D. Blachier, Y. Morand, L. Martel and G. Reimbold, Electrical Characterization of Copper Penetration Effects, *Annual Proceedings - Reliability Physics (Symposium)*, p. 431-432 (2002).
19. G. W. Book, K. Pfeifer, S. Smith, Barrier integrity testing of Ta using triangular voltage sweep and a novel CV-BTS test structure, *Microelectronic Engineering*, 64, p. 255-260 (2002).

20. D.K. Schroder and J.A. Babcock, Negative bias temperature instability: Road to cross in deep submicron silicon semiconductor manufacturing, *J. Appl. Phys*., Vol. 94, N 1, p. 1-18 (2003).

Chapter 7

Summary, conclusions, recommendations

7.1 Summary

In modern integrated circuits with Cu interconnects a diffusion barrier is used between the dielectric and Cu in order to prevent diffusion of Cu through the dielectrics. The choice of such a barrier requires a material exploration and a study of the material reactivity with both Cu and the dielectric used in the back-end processing. This thesis presents results of a study focused on the growth processes of tungsten nitride silicide films by CVD; tungsten nitride and tungsten carbidonitride films by ALD. The suitability of these materials as a diffusion barrier has also been evaluated by testing film properties such as resistivity, RMS-roughness, the reactivity with Cu, blocking properties to Cu diffusion and adhesion. A combination of Cu and the tungsten silicide nitride with a Si to W ratio $\geq$0.8 has shown Si diffusion out of the barriers into Cu resulting in a large increase of Cu-resistivity. Thus, these materials failed the criterion of low reactivity with Cu, which has been tested with four-point probe *in situ* sheet resistance measurements at elevated temperatures. Tungsten nitride and tungsten carbonitride films are shown to have low reactivity with Cu. Moreover, good blocking properties of these films against Cu and Al diffusion have been demonstrated on capacitors and p^+/n diodes.

At the same time a continuous scaling of components in IC's demands the integration of low-k dielectrics, e.g. SiLK^{TM} (an aromatic hydrocarbon based polymer with a static dielectric constant ~2.65), in the back-end process of IC's. This requires a study of processes at the interface of the dielectric film with Ta-based materials, which are now commonly used as barriers. Therefore a study of the interaction of SiLK with the Ta-based materials has been performed. Sheet resistance measurements show that tantalum with 8-10 at% N has better thermal stability on SiLK than the pure Ta film. The four-point bend test shows suitable adhesion.

7.2 Conclusions

Conclusions to *Chapter 3*.

For the deposition of the ternary compounds of $W_xSi_yN_{1-x-y}$ in the WF_6-SiH_4-NF_3-Ar system the thermodynamic calculations show that the stoichiometry of the predicted compounds (Si content) is strongly influenced by the ratio of SiH_4/WF_6 in the temperature range of 250-385 ^oC. In order to deposit W-compounds containing a small amount of Si a flow ratio of SiH_4 to WF_6 should be kept in the narrow range between 3 and 3.6.

Thermodynamic calculations for the ALD process of the $W_xC_yN_{1-x-y}$ showed disagreement between thermodynamics and growth kinetics. In the end the calculations based on the available data are not suitable for qualitative analysis of the process.

Conclusions to *Chapter 4*.

It was shown that during a heat treatment the resistance and the TCR of the Ta-based barrier film increases. This is mainly caused by the incorporation of oxygen. The SiLK layer serves as the source of oxygen. The maximum amount of oxygen from SiLK in Ta after heat treatment at 400 ^oC is estimated to be 10 at%. No further reaction with hydrocarbons from the SiLK has been observed.

Nitrogen in the barrier is shown to limit the incorporation of oxygen. However, the better the barrier against oxygen diffusion, the worse the adhesion at the barrier/SiLK interface.

Ta films containing 8-10 at% N show better performance than pure Ta films being based on the resistance measurements and on the suitable adhesion from the four-point bend tests.

Conclusions to *Chapter 5*.

It was shown that the CVD process of the growth of $W_xSi_yN_{1-x-y}$ films using WF_6, SiH_4 and NF_3 is characterized with a deposition rate of 35-70 nm/min. This is substantially higher than required for barrier

application. Moreover, it was presented that tuning the composition of the films is very difficult regarding the N-content.

The resistivity of the N-rich compounds is 1500-3000 μΩ·cm, which is unacceptably high. Si-rich compound with a suitable resistivity of 550-890 μΩ·cm have shown a Si diffusion out of the barriers into Cu metallisation and a large increase of Cu-resistivity. Thus, these materials failed the criterion of low reactivity with Cu. C-V test of capacitors with Cu/barrier electrode did not show the evidence of diffusion barrier failure.

Conclusions to *Chapter 6*.

For the first time the ALD process for the deposition of $W_{1.5}N$ film with a repeating pulse sequence of $WF_6/NH_3/C_2H_4/SiH_4/NH_3$ is presented.

It is shown that tungsten nitride films grow in ALD mode at 325 and 350 ^oC. The growth rate is about 1 monolayer per cycle. No carbon and Si are incorporated. The low F-content in the films (at the detection limit of RBS and XPS) is due to a combination of SiH_4 and C_2H_4 gases.

Tungsten carbidonitride, $W_{1.5}CN$, films are grown with a cycling of $TEB/WF_6/NH_3$ at 325 ^oC. The growth rate of the films is 1.3 Å/cycle. Also here the amount of F is at the detection limit of RBS and XPS.

Resistivity of $W_{1.5}N$ layers is ~480 μΩ·cm, which is at the same level as the resistivity of our $W_{1.5}CN$ layers being 465 μΩ·cm.

Functional $W_{1.5}N$ and $W_{1.5}CN$ barrier layers have been demonstrated for interconnect. The $W_{1.5}N$ layers with a thickness of 7 and 10 nm and the 10 nm $W_{1.5}CN$ layer did not show failure of barrier properties with I-V test of p^+/n diodes after the 400 ^oC anneal for 30 min in forming gas. $W_{1.5}N$ and $W_{1.5}CN$ layers serve as good barriers for both Cu and Al metallisation.

Four-point probe sheet resistance tests at elevated temperature showed no Cu-barriers interaction up to 500 ^oC. C-V and C-t measurements of capacitors do not reveal Cu diffusion in the SiO_2 protected with a 10 nm barrier film after the anneal treatment.

The combination of low RMS roughness (~0.33-0.43 nm for films of 10-16 nm thick), low resistivity, low reactivity with Cu and good blocking properties against Cu diffusion makes these films promising diffusion barriers.

7.3 Recommendations

Some recommendations for further research are:

- In order to confirm a growth mechanism during the ALD of the $W_{1.5}N$ film, i.e. role of the C_2H_4 (*Chapter 6*), a study of the species available on the surface of the growing film and in the reactor volume should be performed. This comprises surface analysis by in situ XPS/TOFSIMS (Time-of-Flight Secondary Ions Mass Spectroscopy) and mass spectrometry.

- A focus on integration issues should be done for a successful integration of the $W_{1.5}N$ in Cu interconnects. Among others, a study and optimization of Cu growth on $W_{1.5}N$ and $W_{1.5}CN$ films should be performed. Moreover, a study of compatibility of $W_{1.5}N$ with low-k dielectrics should be done.

SAMENVATTING

In moderne geïntegreerde circuits met Cu interconnecties wordt van een diffusiebarrière gebruikt gemaakt tussen het diëlektricum en het Cu om Cu diffusie door het diëlektricum tegen te gaan. Voor de keuze van een dergelijke barrière is het nodig een geschikt materiaal te vinden en onderzoek te doen naar de chemische reactiviteit met zowel het Cu als het diëlektricum zoals dat gebruikt wordt in de IC fabricage.

Dit proefschrift presenteert de resultaten van een studie gericht op de groeiprocessen van wolfraamsilicide-nitride films door CVD en wolfraamnitride en wolfraamcarbonitride films door ALD. Ook de geschiktheid van deze materialen als een diffusie barrière is geëvalueerd door het testen van diverse film eigenschappen zoals: weerstand, RMS-ruwheid, reactiviteit met koper, het blokkeren van koper diffusie en de hechting. Een combinatie van Cu met wolfraamsilicide-nitrides met een Si/W verhouding $\geq$0.8 lieten een Si diffusie zien vanuit de barrière in het Cu, wat resulteerde in een grote toename van de elektrische weerstand van het Cu. Hierdoor haalden deze materialen het criterium van een lage reactiviteit met Cu niet. Dit is getest met *in situ* vier-puntsweerstandsmetingen bij verhoogde temperatuur. Wolfraamnitride en wolfraamcarbonitride toonden een lage reactiviteit met Cu. Bovendien blokkeren deze films Cu en Al diffusie. Dit is aangetoond op condensatoren en p^+/n diodes.

Een continue schaalverkleining van de componenten op IC's vereist de toepassing van materialen met een lage diëlektrische constant zoals SiLK™ (een aromatische koolwaterstof gebaseerde polymeer met een statische diëlektrische constante ~2.65) in de IC fabricage. Hiervoor is onderzoek nodig naar de processen op het grensvlak van de diëlektrische film en Ta gebaseerde materialen welke nu algemeen gebruikt worden als barrière. Om deze reden is de wisselwerking van SiLK met Ta gebaseerde materialen onderzocht. Weerstandsmetingen laten zien dat tantaal met 8-10 at% N, een betere thermische stabiliteit vertonen met SiLK dan de pure Ta film. Deze lagen hebben een voldoende hechting, zoals aangetoond met vier-puntsbuigtesten.

LIST OF PUBLICATIONS

S. Bystrova, A.A.I. Aarnink, J. Holleman, R.A.M. Wolters, ALD of tungsten nitride films: Process study, submitted to the *Journal of the Electrochemical Society.*

S. Bystrova, A.A.I. Aarnink, J. Holleman, R.A.M. Wolters, Barrier Properties of ALD $W_{1.5}N$ Thin Films, Advanced Metallization Conference, San Diego, October 19-21, 2004, to be published in *MRS Proceedings*.

S. Bystrova, J. Holleman, R.A.M. Wolters, Characterization of Ta-based barrier films on SILK for Cu- metallization, Proceedings of Semiconductor Advances for Future Electronics, 2002 (SAFE 2002).

S. Bystrova, J. Holleman, P. H. Woerlee, Growth and properties of LPCVD W-Si-N barrier layers, *Microelectronic Engineering*, 55, p. 189-195, (2001).

ACKNOWLEDGMENTS

A lot of people contributed to this research. This thesis would not be complete without the contribution of a number of people. I would like to thank them all.

First of all, I am sincerely grateful to my promoter Rob Wolters. His great knowledge in material science and fruitful discussions helped me a lot in this research. His guidance through a period of this research was excellent.

Jisk Holleman is thanked for his supervision and critical comments on this thesis, which helped to improve the content of the book.

Pierre Woerlee together with Jisk are truly thanked for the creation of this project. Bob van Donselaar, Hans Wallinga and Jurriaan Schmitz are acknowledged for obtaining the finance for this research.

I am fully indebted to Eddy Ruiter. He is cordially thanked for the full help in the Cleanroom and particular in all kind of “out of order” Wodan situations, including extinguishing a fire in the equipment. Also I would like to thank the Cleanroom staff for the technical support.

I owe much gratitude to Tom Aarnink for his guidance with the Cluster tool for Atomic Layer Deposition, “all-around” professional advice in the Cleanroom, relaxing atmosphere and helping me out by making diodes.

Marcel Weusthof and Henk de Vries are truly thanked for their assistance in the Test room.

Peter Scheeren, Gert Niers, Lars van Tongeren and others from the mechanical workshop for their technical support and construction of the Cluster system. Wilfried Raanhuis and Rindert Nauta for computer support of the system. George oude Elferink from the mechanical workshop for technical support of the pumps for Wodan.

Yde Tamminga, Thuy Dao, Hans Snijders, Peer Zalm, Emile Naburgh, Albert van den Berg, Mark Smithers and Rico Keim for characterisation of my films. Martin Siekman for the introduction and help with AFM measurements. Meint de Boer for his help with the preparation of high

aspect ratio features.

Greja Verheijden is thanked for the preparation samples with SiLK for Chapter 4. Arjen Boogaard for his help with the four-point probe in situ sheet resistance measurements. Jaap den Toonder for his help with the four-point bend measurements. Kees Mutsaers, Martin Maas and Walter de Laat are gratefully thanked for the enjoyable time of my internship in Philips and exercises in Dutch.

Cor Bakker and Frederik Reenders for the support of the PC-network. Annemiek Janssen, Gerdien Lammers, Marie-Christine Predery, Miranda van Wijk, Sofie Kreulen and Joke Vollenbroek for their administrative assistance.

My sincere gratitude is to Margie Rhemrev for helping with my home arrangements, her help and care. Violeta Petrescu is thanked for the introduction to Holland, friendship and so many bursting laughs together!

My office-mates: Sheela Sowariraj, Tu Huang, Radko Bankras, Phuong Le Ming, Nataša Golo are thanked for being supportive and friendly. Radko is also thanked for letting me use some results from his Master study, which he performed within this project (in Chapter 5.3.3). Also I would like to thank all my colleagues (ex and present) from the Semiconductor Components group, Reliability group, Test group and IC Design group for the pleasant atmosphere in our third floor.

I am grateful to my paranimfen Sheela Sowariraj and Radko Bankras for being with me through my defence.

My dad and Tamara Aleksandrovna, my mother-in-law Susan: without their unconditional support this book would have been finished much later. I am fully indebted to my husband Jan and my daughter Mascha who were patient and let me spend our precious time for the writing.

BIOGRAPHY

Svetlana Bystrova was born in 1967 in Leningrad (nowadays Saint-Petersburg, Russia). After finishing high school in 1984 she had one year of work experience as an accountant in Optical Fine-Mechanical Corporation. Then she started her study in Leningrad Polytechnical Institute (later Saint-Petersburg Technical University), which she finished in 1991 with an M.S. degree with a specialisation in “Chemical technology of semiconductor materials and the components of microelectronics”. The following year she was working at the University as an engineer with educational tasks. In 1993 she started working as a scientific worker in Joint-Stock Company “Centre of Perspective Technology and Development” in the group of Semiconductor Devices. The main area of interest was development and fabrication of laser diodes. From 1996 she worked as an English teacher at a primary school. In 1998 she started a Ph. D. research project at the University of Twente, which is completed by writing the thesis entitled “DIFFUSION BARRIERS FOR Cu METALLISATION IN Si INTEGRATED CIRSCUITS. Deposition and related thin film properties”.